IPP-Report

Max-Planck-Institut für Plasmaphysik

Elizaveta Sytova

Modeling of ITER and ASDEX Upgrade detached plasmas using the SOLPS-ITER code with drifts and currents

IPP 2020-05
Juni 2020

With the support of the
Erasmus+ Programme
of the European Union

Modeling of ITER and ASDEX Upgrade detached plasmas using the SOLPS-ITER code with drifts and currents

Sytova Elizaveta

International Doctoral College in Fusion Science and Engineering (FUSION-DC)
Joint Doctoral Training Programme

Doctor in de ingenieurswetenschappen: toegepaste natuurkunde

Le Doctorat en Physique et Sciences de la Matière spécialité Energie, rayonnement et plasma

Date de soutenance: 28 avril 2020

Jury:

M. Yannick Marandet, Président du jury, Charge De Recherche, Universite D'aix-Marseille
Mme Martine Baelmans, Rapporteur du jury, Professeur Des Universites, Katholieke Universiteit Leuven
M. Roger Jaspers, Rapporteur du jury, Professeur Des Universites, Eindhoven University Of Technology
M. Alberto Loarte, Membre du jury, Charge De Recherche, ITER Organization
M. Eric Serre, Membre du jury, Directeur De Recherche, Universite D'aix-Marseille
M. Hendrik Van Landeghem, Membre du jury, Professeur Emerite, Universite De Gent
Mme Kristel Crombe, Directeur, Professeur Des Universites, Universite De Gent
M. Philippe Ghendrih, Directeur, Directeur De Recherche, Commissariat A L'energie Atomique

Max-Planck-Institut für Plasmaphysik
Ghent University
Aix-Marseille Université

Abstract

The ITER project is one of the main focuses of the nuclear fusion research field and aims to build and operate a very large tokamak to test the viability of the tokamak concept for energy production. Modeling studies of the ITER tokamak operation indicate that to allow for steady state operation, the heat fluxes in the ITER divertor would have to be mitigated, otherwise these heat fluxes would exceed material limits.

Currently heat fluxes in tokamak divertors are mostly mitigated by operating with detached divertors in which layers of cold and dense plasma are created near the divertor targets. This regime in tokamaks with metal targets and walls is achieved by introducing radiating impurities. For the ITER reactor, two possible impurity radiators are planned: nitrogen and neon.

In present tokamak experiments nitrogen and neon behave differently with respect to detachment formation. Recent experiments on the ASDEX Upgrade tokamak (AUG) has shown that detachment can be routinely achieved with nitrogen. With neon, on the other hand, a stable detachment regime for AUG has not been achieved despite multiple attempts.

The main mechanisms of detachment formation with impurity seeding is the power loss in the divertor volume due to impurity line radiation. This condition is fulfilled when impurity ions stay in the divertor (so called retention) and is hindered when impurity ions escape the divertor (leakage). In the case of impurity leakage, impurity ions can penetrate the area of the main confined plasma, decreasing the machine performance and even lead to plasma disruptions. Retention and leakage of impurity ions depend nonlinearly on the plasma parameters and numerical modeling is used to understand the mechanisms in the current experimental results and to predict impurity behavior for ITER plasma parameters.

The main goals of the present thesis are to:

- investigate the differences between retention and leakage mechanisms of nitrogen and neon impurities in the context of the detachment formation;

- compare the retention and leakage mechanisms of the nitrogen and neon impurities for ASDEX Upgrade and ITER.

To do this, the SOLPS-ITER code modeling package was further developed and then used. This package, used for the ITER tokamak design, provides information about the plasma particles density, temperature and velocity as well as the plasma potential distribution in the tokamak edge region (scrape-off layer and edge of the confined plasma region). As a first step, the accuracy of the impurity modeling in SOLPS-ITER was increased by modifying the parallel momentum balance equation in the code. As a part of this modification more precise analytical formulations of the friction and the thermal force terms of this equation were derived and implemented in the code. This work was presented at the "Plasma Edge Theory" (PET) Workshop in 2017 and published in a peer-reviewed journal paper.

In the next step, modeling of ITER and ASDEX Upgrade scenarios with Ne and N impurity seeding was performed. The same ratio of radiated to input power ratio was maintained for all four modeling cases to make further comparisons possible. Modeling of the ASDEX Upgrade runs and ITER run with Ne seeding were done in collaboration with the Peter the Great Saint-Petersburg Polytechnic University team, while the ITER N run was performed separately. The input parameters and modeling results are discussed in the present thesis.

On the basis of the modeling, the following conclusions are made:

- impurity transport from the divertor region upstream is found to be different for neon and nitrogen impurities in both ITER and ASDEX Upgrade. Nitrogen is found to be better retained in the divertor volume than neon for both devices. The main factor which causes better retention of the nitrogen in the tokamak divertor is that it ionizes closer to the divertor targets than the main ions. This causes the pressure gradient from the main ions ionization to keep the nitrogen ions in the divertor. This situation is opposite for neon ions: they are ionized further away from the target than the main ions and the main ions pressure gradient leads to the increased leakage of neon;
- even though the retention and leakage of nitrogen and neon has the same mechanism in ITER and ASDEX Upgrade (nitrogen is better retained), in terms of the radiation distribution point of view the two machines behave differently. This difference suggests that neon impurity seeding seem to be an appropriate radiator for ITER, even though for ASDEX Upgrade it results in an unacceptable radiation pattern;
- for the ASDEX Upgrade-like case, a larger percentage of the impurity radiation is present outside the divertor for the neon seeded case in comparison to the

nitrogen case. For the neon case a significant amount of impurity radiation is also present in the core plasma, which in the real experiment leads to a confinement loss;

- for the ITER case, the impurity radiation mostly stayed within the divertor volume for both nitrogen and neon seeded cases, even though more Ne ions escaped the divertor volume. Core impurity radiation was negligible for both seeded impurities. This suggests that neon might be used as a radiative impurity for the ITER power exhaust.

These differences between the nitrogen and neon behavior in ASDEX Upgrade and ITER modeling results are caused by very different plasma backgrounds. The electron temperature distribution was found to be the most influential parameter, and even for the same radiated fractions of the input power, very different profiles of the temperature and the radiative power were obtained for ITER and ASDEX Upgrade. These differences come from the geometrical effects and should be a subject for future investigations. All the findings about the differences in the nitrogen and neon behavior in the ASDEX Upgrade and the ITER modeling as well as the discussion of the possible causes of the plasma background differences and the detailed analysis of the radiated power distributions were presented on the “Plasma Surface Interaction”conference in 2018. It was also published in a peer-reviewed journal paper in 2019.

Beknopte samenvatting

Het ITER project is één van de belangrijkste doelen van net huidig fusie-onderzoek. Het heeft als doel om een tokamak te bouwen, te laten werken op grote schaal en zo de mogelijkheden van een tokamak voor energie-productie te bestuderen. Modelleringsstudies van de operatie van de ITER tokamak tonen aan dat, om langdurige stabiele operatie mogelijk te maken, de warmtestroom in de divertor van ITER moet dalen. Anders overschrijden deze warmtestromen de limieten van het wandmateriaal.

Momenteel worden warmtestromen in tokamak divertors meestal veranderd door gebruik te maken van zogenoemde detachment divertors. Hierin zijn lagen van koud en dicht plasma gecreëerd vlak voor de divertorplaten of targets. In tokamaks met metalen targets wordt dit regime bereikt door onzuiverheden te injecteren die vermogen afstralen. Voor de ITER reactor zijn er twee onzuiverheden voorzien: stikstof en neon.

In huidige tokamak-experimenten gedragen stikstof en neon zich verschillend als het aankomt op de vorming van detachment. Recente experimenten op de ASDEX Upgrade tokamak tonen aan dat detachment gemakkelijk bereikt kan worden met stikstof. Met neon daarentegen, is dit na verschillende pogingen niet gelukt.

Het belangrijkste mechanisme dat de vorming van detachment door de injectie van onzuiverheden drijft, is het verlies van vermogen in het divertor volume door lijnstraling van deze onzuiverheden. Dit gebeurt wanneer de onzuivere ionen in de divertor blijven (zogenoemde behoud van ionen) en wordt verhinderd wanneer de onzuiverheden ontsnappen (lek van ionen). In het geval van lek, kunnen de gelekte onzuivere ionen in de kern van het opgesloten plasma binnendringen en zo de machine prestatie verminderen en zelfs tot een disruptie leiden. Lek en behoud van onzuivere ionen hangt niet lineair af van de plasma parameters. Numerieke modellering wordt gebruikt om de mechanismes die hier een rol in spelen in huidige tokamaks te begrijpen en om het gedrag van onzuiverheden te voorspellen voor de plasma parameters van ITER.

Van deze thesis zijn de belangrijkste doelen de volgende:

- het onderzoeken van de verschillen tussen de mechanismes die zorgen voor lek en behoud van onzuiverheden bij het gebruik van stikstof en neon onzuiverheden voor de vorming van detachment;
- het vergelijken van de mechanismes voor lek en behoud van stikstof en neon onzuiverheden tussen ASDEX Upgrade en ITER.

Om dit te doen, werd de SOLPS-ITER code verder ontwikkeld en daarna gebruikt. Deze geüpgrade versie van de code is gebruikt voor het ontwerp van de ITER tokamak. Het geeft informatie over de dichtheid, de temperatuur en de snelheid van de plasmadeeltjes en ook over de potentiaalverdeling in de plasmarand (bestaande uit een klein gebied buiten de separatrix en de rand van het opgesloten plasma). In een eerste stap is de nauwkeurigheid van de modellering van onzuiverheden in SOLPS-ITER verhoogd door de parallele impulsvergelijking aan te passen in de code. Als deel van deze verandering werd een meer precieze, analytische formulering afgeleid van de wrijvingstermen en van de thermische krachttermen in deze vergelijking. Vervolgens zijn deze geïmplementeerd in de code. Dit werk is gepresenteerd op de "Plasma Edge Theory"(PET) Workshop in 2017 en gepubliceerd in een peer-reviewed vaktijdschrift.

In een volgende stap, werd modellering van ITER en ASDEX Upgrade scenario's met neon en stikstof onzuiverheden gedaan. Dezelfde verhouding van uitgestraald vermogen ten opzichte van input vermogen werd gebruikt voor alle vier gemodelleerde scenario's. Dit maakt een onderlinge vergelijking mogelijk. De ASDEX-Upgradesimulaties en de ITERsimulatie met neon zijn uitgevoerd in samenwerking met het team van de Peter de Grote Sint-Petersburg Polytechnische Universiteit, terwijl de ITERsimulatie met stikstof apart gedaan werd. De input parameters en de resultaten van de modellering worden bediscussieerd in deze thesis.

Op basis van de modellering, zijn de volgende conclusies gemaakt:

- het transport van onzuiverheden in het stroomopwaarts deel van de divertorregio is verschillend voor neon en stikstof, zowel bij ITER als bij ASDEX Upgrade. Stikstof blijft beter in de divertor dan neon in beide machines. De belangrijkste factor die het behoud van stikstof in de tokamak divertor bepaalt, is dat stikstof dichter bij de divertorplaat ioniseert dan de waterstofionen. Dit zorgt voor een drukgradiënt op de waterstof waardoor de stikstof in de divertor blijft. Een tegengestelde situatie werd geobserveerd voor neonionen: zij worden verder weg van de divertor geïoniseerd dan de waterstof ionen. Hierdoor leidt de drukgradiënt van de waterstof ionen tot een verhoogde lek van neon;

- hoewel behoud en lek van stikstof en neondeeltjes op dezelfde manier werken in ITER als in ASDEX Upgrade (stikstof blijft beter behouden), treedt er in beide gevallen een verschillende stralingsverdeling op. Dit verschil suggereert dat neon gebruikt kan worden als straler voor ITER, ondanks dat het voor ASDEX Upgrade resulteert in een onacceptabel stralingspatroon;
- voor cases die gelijkaardig zijn aan ASDEX Upgrade, zal een groter percentage van de straling door onzuiverheden plaatsvinden buiten de divertor in het geval van neon onzuiverheden dan in het geval van stikstof onzuiverheden. Voor de neon case zal een significant deel van de straling door onzuiverheden plaatsvinden in de kern van het plasma. Dit leidt vervolgens in een echt experiment tot een verlies van opsluiting van het plasma;
- voor een ITER case zal de straling door onzuiverheden voor het grootste deel in de divertor zelf blijven, zowel voor stikstof als voor neon, hoewel er meer neonionen ontsnappen uit het divertor volume. Dit suggereert dat neon gebruikt kan worden als onzuiverheidsstraler voor het uitgaand vermogen in ITER.

Deze verschillen tussen het gedrag van stikstof en neon in ASDEX Upgrade en ITER in de resultaten van de modellering worden veroorzaakt door erg verschillende plasma achtergronden. De electronentemperatuurverdeling bleek de meest bepalende factor te zijn, en zelfs voor dezelfde afgestraalde fractie van het inputvermogen, werden zeer verschillende profielen van de temperature en van het afgestraalde vermogen gevonden voor ITER en ASDEX Upgrade. Deze verschillen komen van de geometrische effecten en zouden verder moeten onderzocht worden in de toekomst. Al de resultaten over de verschillen in het stikstof en neongedrag in de ASDEX Upgrade and de ITER modellering, alsook de discussie over de mogelijke oorzaken van de verschillen in de plasma achtergrond en de gedetailleerde analyse van de verdeling van het afgestraalde vermogen, zijn gepresenteerd op de “Plasma Surface Interaction”conferentie in 2018. Het is ook gepubliceerd in een peer-reviewed internationaal tijdschrift in 2019.

Résumé

Le projet international ITER est un point focal du programme de recherche sur la fusion par confinement magnétique. L'objectif est la construction puis l'opération d'un dispositif magnétique appelé tokamak. La taille de ce dernier permettra d'évaluer la performance des tokamaks dans des régimes pertinents pour la production d'énergie. Les études et les expériences en préparation d'ITER ont montré que les flux d'énergie à la périphérie du dispositif seraient nettement supérieurs aux limites imposées par la technologie de refroidissement des matériaux. La solution mise en œuvre dans ITER est de dédier un volume spécifique à l'interaction plasma-paroi appelé divertor, volet technologique, associé à la maitrise d'un point de fonctionnement optimum du divertor, volet physique.

Le régime qui doit être atteint dans le divertor est celui dit de plasma détaché obtenu après une transition vers un état du plasma froid et dense dans la région du divertor en contact avec la paroi. Dans le cas de parois métalliques, et donc pour ITER, une possibilité pour atteindre le régime de détachement est l'injecter d'impuretés extrinsèques, permettant de rayonner une fraction de l'énergie du plasma par l'excitation de lignes spectrales des atomes partiellement ionisés. En vue d'ITER, deux types d'impuretés extrinsèques gazeuses, l'Azote et le Néon, font l'objet d'études tant expérimentales que par la modélisation. Dans les expériences sur les tokamaks en opération, l'injection d'azote ou de néon conduit à des régimes différents. Par exemple, les expériences récentes sur le tokamak ASDEX-Upgrade sont caractérisées par l'obtention d'un régime de détachement stable pour une injection d'Azote alors que les expériences conduites avec une injection de Néon n'ont pas permis jusqu'à lors d'obtenir un régime de détachement stable.

Le principal mécanisme physique associé à l'injection d'impureté est la dissipation de l'énergie du plasma par le rayonnement de raies des impuretés. Ce mécanisme est favorisé lorsqu'une forme de piégeage retient les impuretés dans le volume du divertor. En revanche, quand les impuretés s'échappent du divertor pour atteindre le volume de plasma confiné, on observe à la fois une baisse du rayonnement dans le divertor et une perturbation du plasma confiné qui peut aller jusqu'à une disruption, c'est-à-dire à la terminaison du plasma suite à une instabilité magnéto-

hydro-dynamique du plasma. L'équilibre pour les impuretés entre piégeage dans le divertor et fuite vers le plasma confiné résulte de phénomènes non-linéaires qui dépendent des paramètres du plasma et de l'impact des impuretés sur ce dernier. La modélisation est utilisée pour comprendre les mécanismes dominants dans les expériences actuelles et par cette compréhension réaliser des projections pour ITER. Les principaux objectifs de cette thèse sont :

- analyser les mécanismes déterminant l'équilibre rétention \ fuite pour l'Azote et le Néon dans le régime de plasma détaché du divertor;
- comparer l'efficacité du piégeage relatif aux fuites pour l'Azote et le Néon ainsi que pour les divertors des tokamaks ASDEX-Upgrade et ITER.

A cette fin, le code de modélisation appelé SOLPS-ITER a été modifié et utilisé comme outil d'étude. Dans une version antérieure, le code SOLPS-ITER a été utilisé pour étudier et optimiser le point de fonctionnement du divertor lors du design d'ITER. Il décrit le plasma, densité, vitesse moyenne, énergie thermique, champ électrostatique dans la région périphérique du plasma qui comprend la partie externe du plasma confiné, une région de couche limite appelée SOL (Scrape-Off Layer) et la région du divertor. La première étape de modification du code a été d'améliorer les équations de bilan de quantité de mouvement dans la direction parallèle au champ magnétique, notamment pour les impuretés. Le rôle des collisions dans équilibre des forces est un point important pour évaluer le transport des impuretés. Dans cet esprit, des expressions analytiques plus précises des forces de friction inter-espèces et des forces thermiques ont été établies puis utilisées dans le code. Ce travail a été présenté à la conférence "Plasma Edge Theory"en 2017 et a donné lieu à une publication dans une revue avec comité de lecture. La modélisation des scénarios d'opération d'ASDEX-Upgrade et d'ITER avec injection d'Azote ou de Néon a ensuite été abordée. La comparaison des régimes obtenus dans les quatre cas a été faite pour une fraction puissance rayonnée sur puissance injectée donnée. La modélisation avec Néon, aussi bien pour ASDEX-Upgrade que pour ITER a été réalisée en collaboration avec l'équipe de l'Université Polytechnique de Pierre le Grand à Saint Pétersbourg. Le choix des paramètres de simulation et les résultats obtenus sont présentés et discutés dans cette thèse.

Les principales conclusions de ce travail de modélisation sont :

- Le transport des impuretés le long des lignes de champ, de la région du divertor vers la région amont, à proximité du volume de confinement, est différent pour l'Azote et le Néon aussi bien dans ASDEX-U que dans ITER. On observe que la rétention de l'Azote dans le volume divertor est supérieure à celle du Néon dans les simulations pour les deux tokamaks. Le principal mécanisme conduisant à cet effet est la différence de potentiel d'ionisation entre ces deux espèces conduisant à une première ionisation de l'Azote à une distance moindre de la paroi que celle de l'ion majoritaire. La force de pression des ions majoritaires tend alors à favoriser le piégeage de l'Azote. Inversement, la première ionisation du Néon se produit au-delà de celle de l'espèce d'ions majoritaires conduisant à un effet opposé des forces de gradient, et en conséquence favorise la migration des impuretés vers l'extérieur du divertor.

- Si les mécanismes de rétention et de migration des impuretés dans le divertor donnent des résultats comparables pour ASDEX-Upgrade et pour ITER, la situation est assez différente du point de vue de la distribution spatiale du rayonnement. Cette différence permet de penser que le Néon sera efficace dans les scénarios pour ITER.

- Les résultats de simulation pour ASDEX-Upgrade indiquent une localisation du rayonnement du Néon en dehors du divertor ce qui expliquerait les difficultés rapportées dans les expériences.

- Dans le cas de la modélisation pour ITER, la distribution spatiale du rayonnement est pour l'essentiel localisée dans le volume du divertor. Le rayonnement consécutif à la migration du néon vers le plasma confiné reste négligeable. Ce résultat suggère que le Néon, gaz noble chimiquement neutre, pourrait être avantageusement utilisé dans ITER, permettant d'éviter l'utilisation de l'Azote et les problèmes à long terme posé par la réactivité chimique avec l'hydrogène.

La différence des résultats de modélisation rapportée dans la thèse entre ASDEX-Upgrade et ITER est due à la différence de régime du plasma. En particulier, une différence notable dans la distribution spatiale de l'énergie thermique des électrons joue un rôle important. L'origine de cette différence semble consécutive pour l'essentiel à une différence de géométrie entre les deux dispositifs. Un sujet d'analyse important à mener pour confirmer et expliquer cette propriété anticipée par ce travail de modélisation. L'ensemble des résultats de simulation et leurs interprétations a été présenté à la conférence internationale "Plasma Surface Interaction"en 2018. Il a également été présenté et publié dans un journal avec comité de lecture en 2019.

Résumé long

Le projet international ITER est un point focal du programme de recherche sur la fusion par confinement magnétique. L'objectif est la construction puis l'opération d'un dispositif magnétique appelé tokamak. La taille de ce dernier permettra d'évaluer la performance des tokamaks dans des régimes pertinents pour la production d'énergie. Les études et les expériences en préparation d'ITER ont montré que les flux d'énergie à la périphérie du dispositif seraient nettement supérieurs aux limites imposées par la technologie de refroidissement des matériaux. Pour surmonter ce problème dans ITER un volume spécifique appelé divertor est dédié au contrôle de l'interaction plasma-paroi.

Le régime qui doit être atteint dans le divertor est celui dit de plasma détaché obtenu après une transition vers un état du plasma froid et dense dans la région du divertor en contact avec la paroi. Pour atteindre le régime de détachement, une des voies retenues est de bénéficier du rayonnement par des impuretés de faible nombre atomique. Avec des parois métalliques, et donc pour ITER, une possibilité est d'injecter des impuretés extrinsèques. Dans le cas d'ITER, on envisage une injection d'azote (N) ou de néon (Ne).

Dans les expériences sur les tokamaks en opération, l'injection d'azote et celle de néon conduisent à des régimes différents. Par exemple, les expériences récentes sur le tokamak ASDEX-Upgrade ont permis d'obtenir un régime de détachement stable pour une injection d'azote alors que les expériences conduites avec une injection de néon n'ont pas permis jusqu'à présent d'obtenir un régime de détachement stable.

Le principal mécanisme physique associé à l'injection d'impuretés est la dissipation de l'énergie du plasma par rayonnement de raie des impuretés. Ce mécanisme est favorisé lorsqu'une forme de piégeage retient les impuretés dans le volume du divertor. En effet, le rayonnement de raie est très efficace mais n'a lieu que dans un domaine restreint d'énergie des électrons. En dessous d'un seuil, l'état d'ionisation requis pour maximiser le rayonnement n'est pas obtenu, alors qu'au-dessus d'un autre seuil, l'impuretés est trop ionisée, voire complètement ionisée, et l'optimum de rayonnement est perdu. Cette description montre qu'il faut maximiser la concentration d'impuretés dans la région où la température électronique correspond aux énergies de cet optimum, et, pour ne pas modifier les performances de fusion du plasma de cœur, dans la région périphérique du plasma, typiquement le divertor. Pour les impuretés, l'équilibre entre piégeage dans le divertor et fuite vers le plasma confiné résulte de phénomènes non-linéaires qui dépendent des paramètres du plasma et de l'impact des impuretés sur ce dernier. La modélisation est utilisée pour comprendre les mécanismes dominants dans les expériences actuelles et par cette compréhension réaliser des projections pour ITER. L'enjeu est l'équilibre rétention-fuite des impuretés : par rétention, on entend le piégeage des impuretés dans le divertor, et par fuite le transport des impuretés, azote ou néon, en dehors du plasma de divertor vers le plasma central.

Les principaux objectifs de cette thèse sont :

- D'analyser les mécanismes déterminant l'équilibre rétention-fuite dans le régime de plasma détaché du divertor.
- De comparer l'efficacité du piégeage pour l'azote et le néon ainsi que pour les géométries des divertors des tokamaks ASDEX-Upgrade

et ITER.

Le travail de modélisation a été effectué avec ensemble de codes appelé SOLPS-ITER. Il a été réalisé en deux étapes, une étape de développement pour améliorer le modèle physique du code et une étape d'exploitation. Dans un premier temps, la précision de la modélisation des impuretés dans SOLPS-ITER a été améliorée en introduisant des formulations analytiques plus précises des frictions collisionnelles et des termes de force thermique. Ces travaux ont été présentés lors de la conférence "Plasma Edge Theory"(PET) en 2017 et publiés.

La modélisation des scénarios des expériences réalisées dans ASDEX-Upgrade et projetées dans ITER avec injection d'azote ou de néon a ensuite été abordée. La comparaison des régimes obtenus est basée sur quatre cas caractéristiques correspondant aux deux espèces injectées et aux deux dispositifs expérimentaux. Pour réaliser cette comparaison, le paramètre de contrôle, fraction puissance rayonnée sur puissance injectée, est fixé.

Les principales conclusions de ce travail de modélisation sont les suivantes:

- Le transport des impuretés le long des lignes de champ, de la région du divertor vers la région amont, à proximité du volume de confinement, est différent pour l'azote et le néon aussi bien dans ASDEX-U que dans ITER. On observe que la rétention de l'azote dans le volume divertor est supérieure à celle du néon dans les simulations pour les deux tokamaks.
- Bien que les mécanismes de rétention et de migration des impuretés dans le divertor donnent des résultats comparables pour ASDEX-Upgrade et pour ITER, la situation est assez différente quant à la distribution spatiale du rayonnement. Cette différence

permet de penser que le néon sera efficace dans les scénarios pour ITER bien qu'il semble moins adapté au cas d'ASDEX-Upgrade.

L'ensemble des résultats de simulation et leurs interprétations a été présenté à la conférence internationale "Plasma Surface Interaction" en 2018 et publié en 2019.

Une description détaillée de la thèse est présentée ci-dessous. La thèse comporte huit chapitres, y compris les chapitres d'introduction et de conclusion.

Chapitre d'introduction.

Dans ce chapitre, le problème du dépôt de chaleur sur la paroi est présenté. Tout d'abord, le concept de divertor ainsi que le développement d'une structure comparable à une couche limite, le plasma dit de Scrape-Off Layer, sont décrits, voir Fig. 1. Dans un deuxième temps, les problèmes de rétention des impuretés dans le volume du divertor sont discutés, en se concentrant sur les régimes présentant localement un flux de puissance élevés car concentré sur des zones de faible surface. La solution au problème des fortes valeurs du flux d'énergie et de concentration du dépôt de puissance que nous considérons est celle d'un régime dit de plasma détaché induit par le rayonnement des impuretés. La pertinence de cette solution est discutée en détail pour le cas ITER.

Les mécanismes déterminant le transport des deux impuretés prévues pour ITER - azote et néon – sont discutés dans la perspective des résultats expérimentaux récemment obtenus et dans celle de la modélisation ITER initialement réalisée avec le code SOLPS 4.3. L'objectif principale de la thèse est la comparaison de ces mécanismes pour l'azote aussi bien que le néon dans la modélisation des tokamaks ITER et

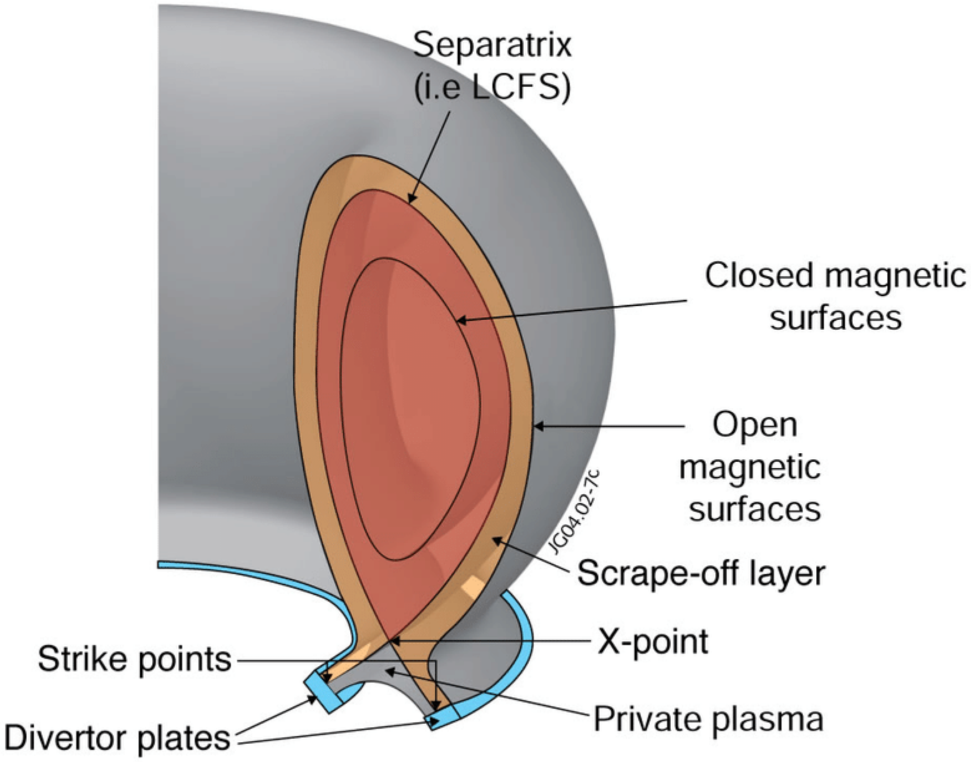

Figure 1: Schéma de la configuration “divertor axisymétrique ”dans un tokamak. Figure originale dans la référence [1]

ASDEX à partir des versions les plus récentes et les plus complètes des codes SOLPS-ITER.

Un bref historique du développement du code SOLPS de la version SOLPS 4.3 vers la version SOLPS-ITER est présenté. L'impact possible de ces développements sur la modélisation ITER est discuté avec un accent particulier sur les effets induits par la prise en compte des vitesses de dérive. Le résumé des principaux résultats et la description des chapitres de la thèse concluent le chapitre Introduction.

Plasma de bord et interaction plasma-paroi.

Ce chapitre présente les principaux concepts de physique et d'ingénierie de l'interaction plasma-paroi utilisés dans la thèse. Le point de départ est la description des configurations limiteur et divertor du tokamak. La discussion est illustrée par l'exemple du tokamak ASDEX-upgrade dont les configurations limiteur et de divertor sont présentées Figure 2. La formation de la couche limite appelée gaine à l'interface du plasma et de l'état solide constituant les composants face au plasma est rappelée. La physique qui caractérise cette région fixe les conditions limites pour la modélisation et notamment le flux d'énergie à la paroi. Une autre physique détermine l'extension radiale de la Scrape-Off Layer, la région du plasma en contact avec la paroi dans la direction parallèle au champ magnétique. Les mécanismes qui diminuent la qualité du confinement par le champ magnétique, essentiellement le transport turbulent transverse, jouent ici un rôle essentiel.

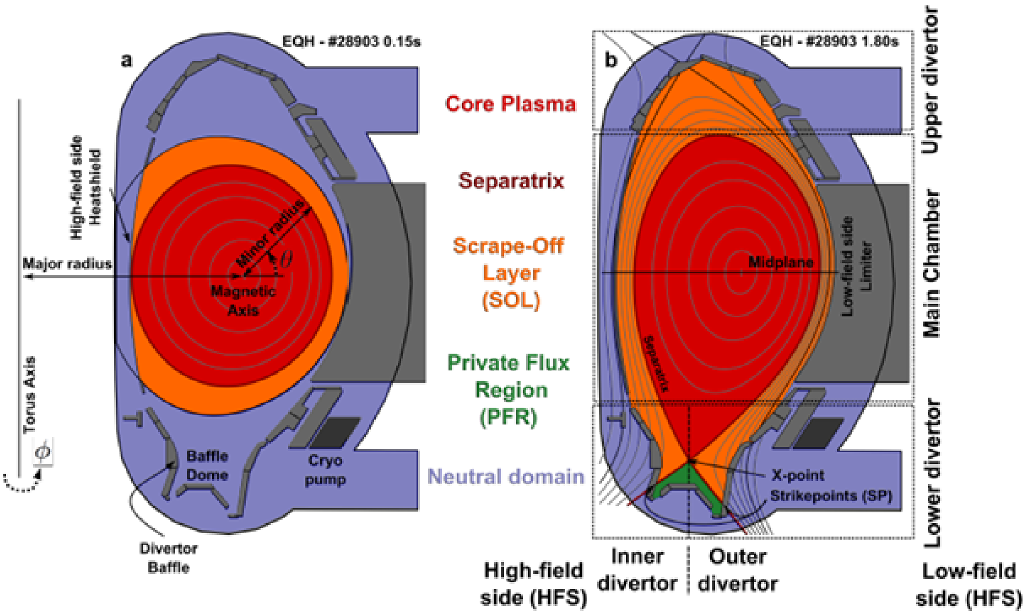

Figure 2: Configurations limiteur (à gauche) et divertor bas du tokamak ASDEX-upgrade. Figure tirée de la référence [2]

Étant donné que l'une des caractéristiques importantes de la modélisation SOLPS-ITER utilisée dans cette thèse est le transport induit par les vitesses de dérive transverse au champ magnétique, une discussion détaillée de ces écoulements dans le plasma est présentée dans ce chapitre. La physique déterminant ces flux est présentée. Des croquis, montrant l'organisation et les directions des écoulements de dérive se trouve à la fin de ce chapitre, ainsi que Fig. 3 - schémas des écoulements poloïdaux et radiaux; et Fig 4 - schéma de principe de l'organisation des écoulements résultant de la modélisation SOLPS-ITER.

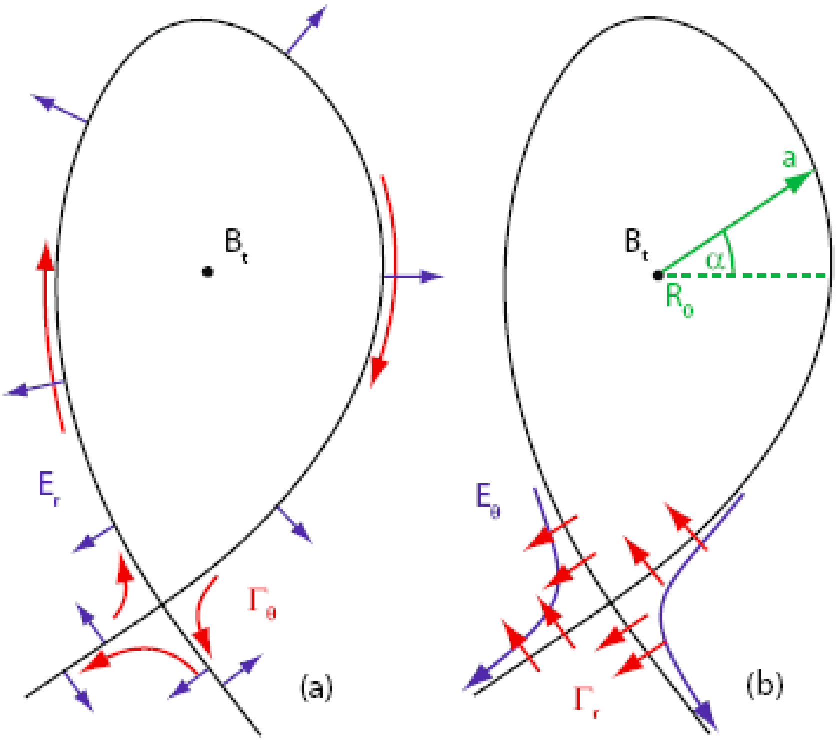

Figure 3: Un exemple des flux de particules poloïdaux (a) et radiaux (b) induits par les dérives ExB indiqués par les flèches de couleur rouge. Le champ électrique associé est indiqué par les flèches en bleu. Reproduit de [3]

Équations de transport.

Le principal outil méthodologique de la thèse est la modélisation du plasma périphérique basée sur des équations de transport. La terminologie de cette approche et la dérivation des équations de transport sont décrites dans ce chapitre 3.

Le point de départ est la description cinétique du transport, les espèces présentes dans le plasma étant décrite par une fonction de distribution. L'équation de Boltzmann, décrivant l'évolution de cette fonction, est introduite. L'approximation fluide est utilisée pour déterminer les équations de conservation de la densité, de la quantité de mouve-

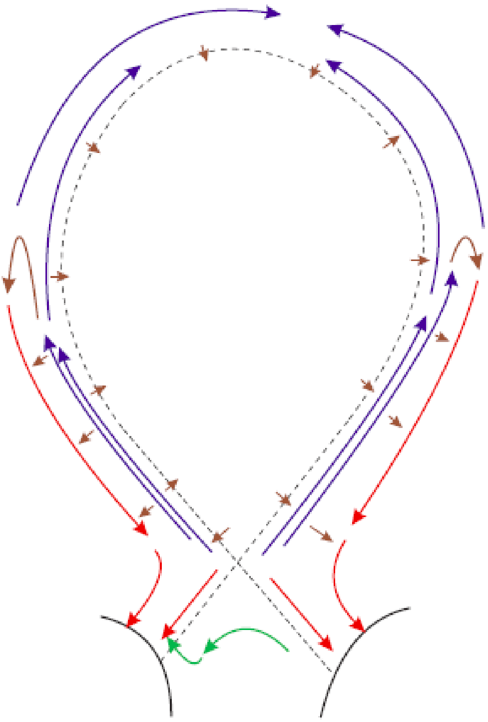

Figure 4: Un exemple du schéma compliqué du flux ionique dans la région SOL. La vitesse de dérive ExB responsable du transport les particules de la région externe du divertor vers la région interne est indiquée en vert. Reproduit de [4]

ment et de l'énergie du plasma. La fermeture du système d'équations dans la limite d'un plasma fortement collisionnel permet d'obtenir le système d'équations utilisé pour décrire le transport dans le plasma dans cette modélisation.

Code SOLPS-ITER.

Dans ce chapitre, le système complet des équations utilisées dans le code SOLPS-ITER est présenté ainsi que la géométrie imposée par le champ magnétique.

Les équations SOLPS-ITER sont données en géométrie toroïdale mais supposent une symétrie axiale, les quantités sont donc invariantes par rotation toroïdale indiquée par la direction z. Les coordonnées dans le plan transverse, le plan poloïdal, sont désignées comme suit: x - pour la direction selon l'angle poloïdal, y - pour la direction radiale. Le système de coordonnées du code SOLPS-ITER, pour un exemple de maillage utilisé pour le tokamak ASDEX-upgrade, est présenté Figure 5 [5]. Le système d'équations SOLPS-ITER comprend

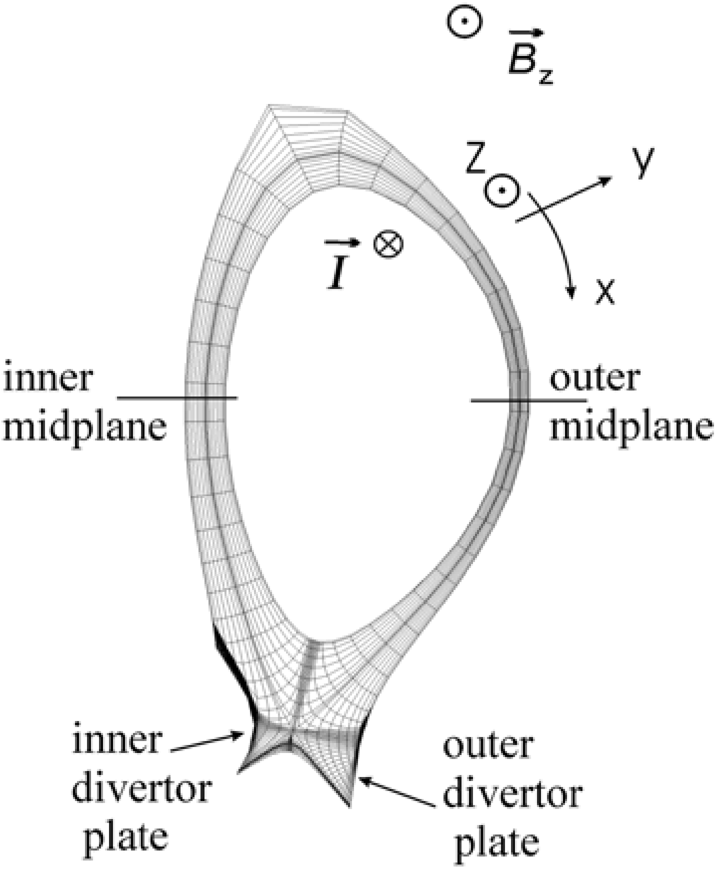

Figure 5: Le système de coordonnées du code SOLPS-ITER pour un maillage utilisé pour le tokamak ASDEX Upgrade, figure tirée de la référence [5].

les équations de conservation des particules du plasma, de la quantité de mouvement dans la direction parallèle, l'équation de transport de chaleur et l'équation de conservation de charge. L'ensemble complet des équations est présenté ainsi que la discussion des conditions aux limites.

Transport d'impuretés et modification de l'équation d'équilibre de la quantité de mouvement parallèle.

Ce chapitre présente les résultats d'une des parties importantes de la thèse, à savoir la modification de l'équation de bilan de la quantité de mouvement parallèle. Cette modification permet de retrouver une forme analytiquement plus claire de l'équation: dans la version antérieure du code SOLPS, le bilan de quantité de mouvement parallèle a été modélisé dans la limite asymptotique où les impuretés sont à l'état de trace, c'est-à-dire qu'elles suivent les écoulements déterminés par l'espèce ionique principale, sans participer à sa définition. La nouvelle version permet une modélisation plus précise du plasma de tokamak en régime détaché ainsi que du rayonnement par les impuretés quand les effets d'accumulation des impuretés deviennent sensibles et ne permettent plus d'utiliser l'hypothèse d'impuretés à l'état de trace. La comparaison entre les deux formes de de cette équation ainsi que la dérivation de la nouvelle forme du code sont décrites dans ce chapitre.

Discussion des résultats de la modélisation pour ITER et ASDEX-upgrade.

Ce chapitre aborde les résultats de modélisation obtenus avec le code SOLPS-ITER avec la nouvelle forme de l'équation d'équilibre de quantité de mouvement parallèle, discutée dans le chapitre précédent.

Les paramètres d'entrée pour chaque cas de modélisation sont présentés et comparés. Le choix du taux d'injection des impuretés est discuté: il est fixé de telle sorte que les distributions de la température et de la densité soient similaires dans les cas avec injection d'azote et de néon (AUG N similaire à AUG Ne et ITER N similaire à ITER Ne). Pour le tokamak ITER comparé au tokamak ASDEX-upgrade tokamaks (ITER versus AUG), le choix des taux d'injection des impuretés a été fait de manière à obtenir des rapports similaires de puissance rayonnée sur puissance injectée. Pour les cas avec injection d'azote, les valeurs suivantes ont été atteintes: 60% de la puissance totale rayonnée pour ITER et 48% pour le cas AUG. Les cas avec injection de néon avaient les valeurs suivantes: 67% de puissance rayonnée pour

ITER et 52% pour AUG.

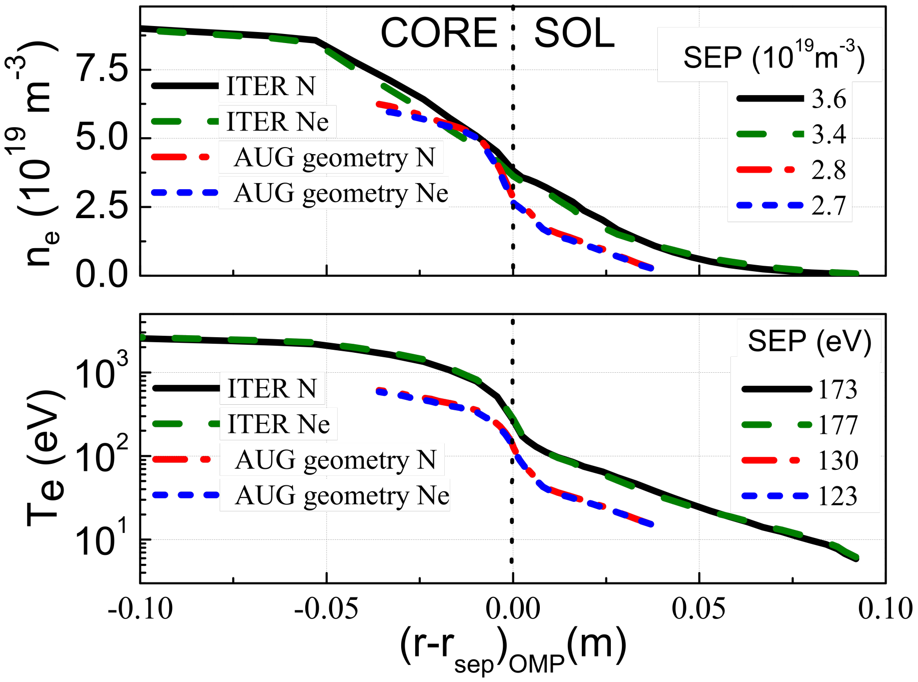

Figure 6: Profils dans le plan équatorial externe et valeurs à la séparatrice de la densité et de la température électroniques pour tous les cas considérés.

Les profils dans le plan équatorial externe de la densité électronique et de la température pour les 4 cas de modélisation considérés dans cette thèse sont présentés sur la figure 6. Cette figure montre que les profils sont comparables pour les deux cas d'injection et dépendent bien sûr du dispositif considéré.

La densité à la séparatrice pour les cas de modélisation avec la géométrie AUG est plus faible que celle pour les cas ITER. Une telle différence peut être expliquée par l'injection de deutérium plus élevée qui a été utilisée dans la modélisation pour ITER. La température à la séparatrice est également plus basse dans les cas de modélisation AUG. Cette différence est également attendue en raison des différences de paramètres d'entrée : notamment la puissance venant du plasma central est 20 fois plus grande dans le cas de la modélisation d'ITER que dans celle pour AUG.

Les distributions de densités et de températures électroniques dans le divertor pour les 4 cas de simulations sont présentées sur les Fig. 7 et 8 respectivement. Sur la Fig. 9, les flux d'énergie sur la paroi du divertor sont présentées pour chacun de ces cas.

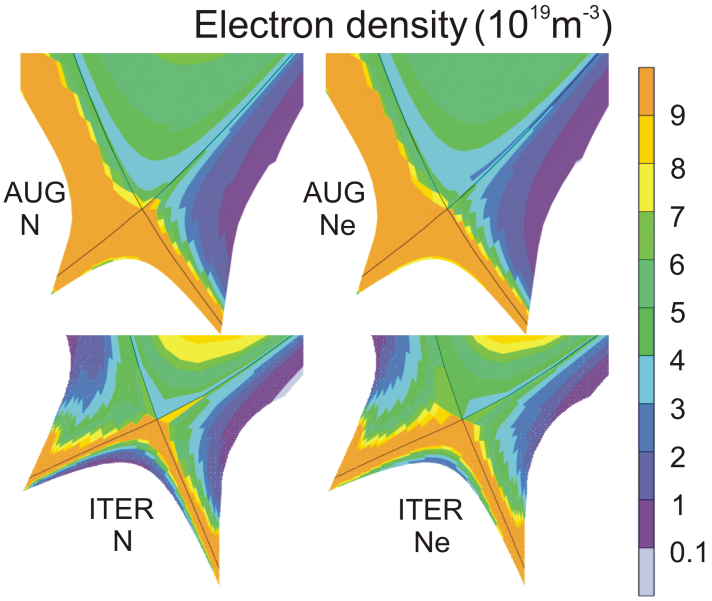

Figure 7: Densité électronique dans le divertor. En haut à gauche- injection d'azote dans AUG, en haut à droite – injection de néon dans AUG, en bas à gauche injection d'azote dans ITER, en bas à droite injection de néon dans ITER.

Ces résultats montrent les différences qui apparaissent aussi bien en volume que localement pour des cas d'injections comparables d'impuretés. Dans le cas d'injection d'impuretés N et Ne, une zone de forte densité et de basse température est présente près de la paroi du divertor côté interne, comparable aux observations expérimentales [40]. Le flux d'énergie au niveau de la paroi interne est faible, en accord avec un état complètement détaché. En revanche, le côté externe dans les cas AUG correspond à un état partiellement détaché, avec une température électronique basse uniquement dans le voisinage de la séparatrice, et une région beaucoup moins étendue de haute densité électronique. Par ailleurs, les profils de flux de chaleur à la paroi sont beaucoup plus élevés.

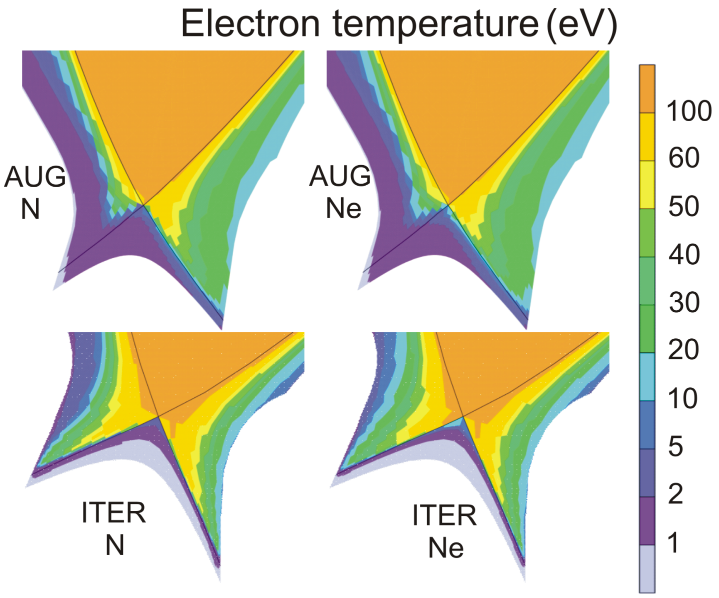

Figure 8: Température électronique dans le divertor. En haut à gauche – injection d'azote dans AUG, en haut à droite – injection de néon dans AUG, en bas à gauche – injection d'azote dans ITER, en bas à droite injection de néon dans ITER.

Dans les résultats de la modélisation ITER, les distributions de la densité et de la température dans le divertor sont beaucoup plus symétriques. Le pic de densité électronique est large du côté interne, mais cet effet est beaucoup moins prononcé que dans le cas de AUG. La distribution de la température électronique et des flux de chaleur est également plus symétrique dans les résultats de la modélisation ITER. L'une des raisons possible est la baisse des vitesses de dérive électrique à travers la région dite de flux privé reliant les deux côtés du divertor. Cet effet est discuté dans la référence [16].

Rétention et fuite d'impuretés: comparaison des cas d'injection d'azote et de néon pour ITER et ASDEX-upgrade.

Dans ce chapitre sont discutés les mécanismes de transport des impuretés dans ITER et ASDEX Upgrade. A la frontière de la région divertor et SOL, côté extérieur, la modélisation pour AUG et ITER présente une inversion de la direction d'écoulement du flux ionique. Dans le volume du divertor le flux de particules est orienté vers la

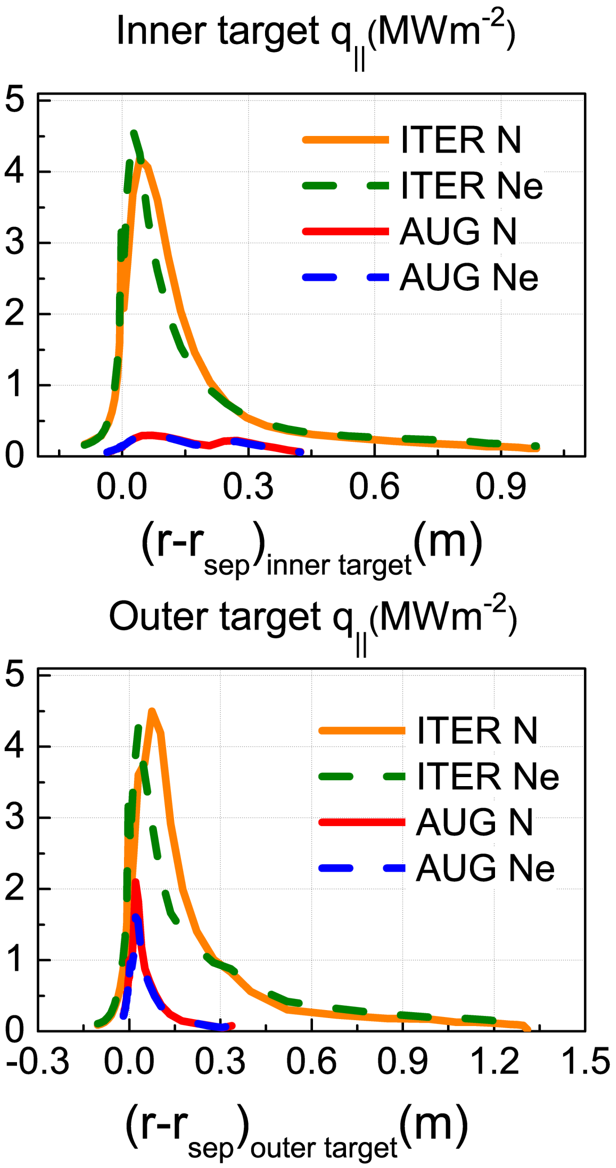

Figure 9: Profils de dépôt du flux d'énergie sur la paroi du divertor, côté intérieur (figure du haut) et extérieur (figure du bas) pour les 4 cas de modèlisation.

paroi du divertor, alors que plus en amont, vers la SOL, le flux de particules est inversé, comme indiqué sur la Figure 10. La position du point de stagnation du flux ionique se situe approximativement au niveau du front d'ionisation. Cette organisation particulière peut s'expliquer par le gradient de pression qui se développe au voisinage de la source de densité ionique. La position du point de stagnation peut encore être décalée par les effets induits par les vitesses de dérive électrique ainsi que par les dérives liées au gradient d'intensité du champ magnétique. L'effet des dérives sur la rétention d'impuretés et les fuites pour les simulations d'azote et de néon avec SOLPS-ITER est discuté dans [6] et dans [4]. L'effet des dérives sur la rétention et la fuite d'argon est étudié dans [7].

Il a été constaté dans les simulations que les fronts d'ionisation de l'azote, N, et du néon, Ne, sont localisés différemment par rapport au front d'ionisation du deutérium dans tous les cas considérés. Les conditions d'opération retenues dans cette modélisation sont telles que les principales propriétés du plasma, que ce soit pour les électrons ou l'espèce ionique majoritaire, le deutérium, sont comparables aussi bien dans les cas d'injection d'azote que de néon, et ce, dans chacun des dispositifs ITER et AUG. Cela signifie que la température des électrons et la distribution de densité dans le divertor et la SOL en amont sont similaires. Pour AUG et ITER dans les cas d'injection d'azote, la première ionisation des impuretés se produit plus près de la paroi du divertor que celle du deutérium. Dans les cas avec le néon, les impuretés sont ionisées plus en amont. Ce fait semble être le facteur déterminant de la différence entre l'azote et de néon quant à l'équilibre fuite / rétention de ces impuretés.

Dans tous les cas de modélisation considérés, la première ionisation de l'azote se produit au voisinage de la paroi du divertor, le deutérium et le néon présentant des pics d'ionisation plus éloignés dans la direc-

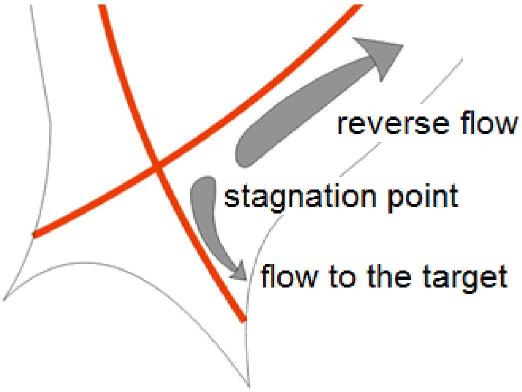

Figure 10: Inversion du flux ionique dans le divertor.

tion du plan équatorial. Cette observation est valable dans les deux géométries, celle d'ITER et celle ASDEX-upgrade. Du point de vue de la modélisation SOLPS-ITER, le néon se répandra alors plus facilement vers la SOL aussi bien dans ITER, que dans ASDEX-upgrade. Néanmoins, la comparaison des résultats de modélisation avec injection de néon et d'azote dans AUG par rapport à ITER indique que le néon serait approprié pour ITER. Cette différence de propriété est illustrée par la distribution spatiale de la puissance rayonnée.

Pour les injections de néon et d'azote, le pic de puissance rayonnée dans le cas d'ASDEX-upgrade est localisé autour du point X. Dans les cas ITER, le pic de la puissance rayonnée pour les deux types d'impuretés est localisé proche du point d'intersection de la séparatrice sur la paroi du divertor, là où se trouve le pic de puissance déposé à la paroi. Les distributions spatiales de la puissance rayonnée sont représentées sur la Fig. 11.

La principale raison conduisant à ces différences entre les distributions de puissance rayonnée est la suivante : pour une raison de taille du divertor d'ITER, le front de détachement reste à l'intérieur du volume divertor, loin du point X. De plus les niveaux de puissance plus élevées dans le cas d'ITER permettent de maintenir une température plus élevée plus loin du point X en direction de la paroi du diver-

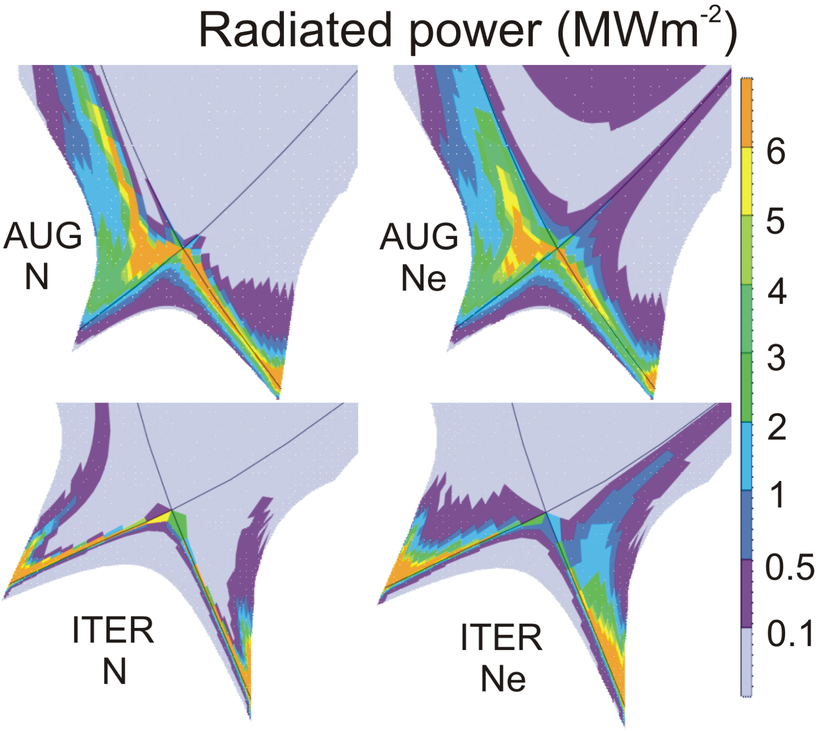

Figure 11: Distribution de puissance rayonnée dans ASDEX-upgrade, rangée supérieure, et ITER, rangée inférieure avec injection d'azote N,colonne de gauche, et de néon Ne, colonne de droite.

tor. Ces deux faits déterminent une distribution différente des états d'ionisation et donc des états déterminant la localisation du maximum de rayonnement. L'effet de taille favorise ainsi la localisation dans le volume du divertor et la condition d'opération d'un divertor fermé.

Chapitre Conclusions

Ce chapitre résume la thèse. Les points discutées dans la conclusion sont ceux qui sont abordés ce résumé.

Contents

Chapter 1

Introduction

The ITER project consists of designing, building and operating the largest tokamak in the world. Since this tokamak is expensive, it is important to model plasma behavior in it to predict possible problems.

For tokamaks in general the exhaust power handling issue is an important one [8]. In most modern tokamaks, power exhaust is handled through a special chamber geometry called the divertor configuration. An example of the divertor configuration is shown in Fig. 1.1, a more detailed description is given in Chapter 2.

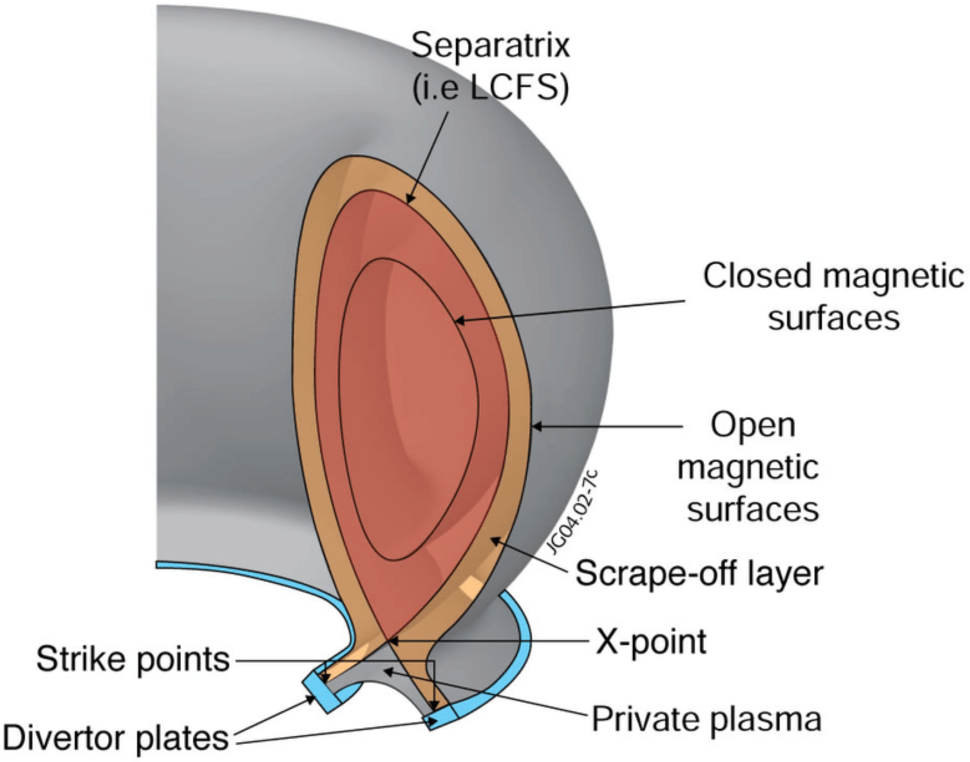

Figure 1.1: Sketch of the tokamak divertor configuration. Adapted from [1]

A divertor configuration was initially suggested to limit the plasma surface interaction area [9] and to limit impurity transport into the main plasma. Impurities are in general avoided in tokamak operations, because if they are present in the plasma, they cause power losses by line radiation and reduce the energy confinement time.

In the divertor configuration the confining magnetic field is designed in such a way that plasma power and particle fluxes are directed to the special areas of the tokamak wall, called the divertor targets. In this way, plasma surface interaction (PSI) becomes mostly located on the divertor targets and the sputtering area becomes smaller. Additionally, divertor targets are usually made from refractory, low sputtering materials. For ITER, divertor targets are planned to be made from W (Tungsten) [8].

Although the divertor configuration is beneficial to the tokamak operation due to its ability to limit the impurity transport to the main plasma, it also has drawbacks. Since in this configuration most of the power is deposited on a limited area, the density of the heat fluxes becomes high. In ITER the highest heat load on the targets is going to occur when the real fusion operation is going to start, in the so called "DT phase"[8]. It is important to design the ITER components and plan the reactor operations in such a way that the divertor targets will survive the heat fluxes deposited on them during operation.

If the heat fluxes in the DT phase are not mitigated, it was estimated that they are going to be too high (more than the material limit of 10 MW/m^2) [8]. This is why it is planned to mitigate heat fluxes by using the so called "detachment regime" [10] .

The divertor detachment regime allows a significant reduction of heat fluxes to the targets without power losses in the confined plasma. To achieve divertor detachment the main condition is to have a significant amount of power radiated. This radiation usually comes from the impurities in the plasma.

Initially, detachment was first studied with carbon (C) impurity radiation [11]. Carbon was actively used as the divertor target material because it has low charge number and does not melt.

Due to the chemical issues with carbon [12] it was decided to avoid its usage in ITER. The ITER chamber will be made from Beryllium (Be) and the divertor will be made from Tungsten (W). In these conditions divertor detachment is only achievable with impurity seeding [8]. Two seeding impurities are planned: Nitrogen (N) and Neon (Ne).

The detachment regime with a seeded impurity is widely studied in all the modern tokamaks. The most relevant studies to the ITER conditions are done in the full-metal chamber environments: on the ASDEX Upgrade and JET tokamaks. Results of these studies state that on both ASDEX Upgrade and JET it is easier to achieve divertor detachment with N seeding than with Ne seeding. It is not possible in the second case to obtain a stable exhaust scenario. In the Ne seeded discharges dithering between H- and L- modes occurs, which is connected to core plasma radiation losses by Ne [13].

For ITER it will be beneficial to use Ne as the seeded impurity for the power exhaust. Usage of N will lead to the formation of tritiated ammonia and reduce the duty cycle of the cryopump [8]. Initial numerical studies of the ITER divertor performance suggested that in contrast to existing tokamaks, ITER divertor conditions will allow stable exhaust with Ne seeding [8].

To estimate the steady state power fluxes to the divertor targets in ITER, numerical modeling of the plasma boundary is used. Although the plasma discharge is a highly time dependent process and it includes large variation of the parameters, proper time-dependent modeling of the plasma boundary at the moment is extremely numerically expensive due to the complexity of the model. Modeling of ITER divertor is performed using SOLPS codes under steady state conditions (SOLPS 4.3 for initial divertor design [12] and SOLPS-ITER for further investigations).

Recently modeling results of N and Ne exhaust scenarios for ITER were analyzed on the basis of SOLPS4.3 modeling [8]. This analysis found that the distribution of the radiated power is similar for N and Ne seeded scenarios: for the same amount of the total radiated power the same amount was radiated in the divertor region in N and Ne seeded cases with similar impurity concentration at the separatrix [8]. This fact suggests that Ne can be used as a divertor radiator in ITER as efficiently as N in contrast with the experimental observation on the smaller machines.

In ASDEX Upgrade experiments, as it is mentioned above, it was not possible to achieve stable power exhaust with the Ne seeding [13]. At the same time N seeding in ASDEX Upgrade provides stable and reproducible power exhaust [13].

The idea of the present PhD project was to test the suitability of Ne for ITER with the improved (in comparison with the initially used SOLPS 4.3) version of the SOLPS code - the SOLPS-ITER code.

Another important point of the study is to at least qualitatively reproduce the difference of the power exhaust of Ne and N observed on ASDEX Upgrade. This point is necessary to show the ability of the SOLPS-ITER code to reproduce possible differences between N and Ne in the ITER modeling.

SOLPS-ITER code is one of many codes for the tokamak plasma boundary area. This code is based on Braginsky-like equations solver to model plasma transport processes coupled to the Eirene Monte-Carlo code for the modeling of the neutral particles behavior.

SOLPS code was proposed in 1987 and back then it was called B2. The code consisted only of the Braginsky solver. Since then significant changes were introduced, leading to a much more complex physics model. One of the significant changes was the coupling with the Eirene code[14]. The version used for the initial ITER divertor design in 2001-2009 was SOLPS4.3 [15]. In the present thesis version SOLPS-ITER 3.0.6 is used. This version was released in 2016 [16].

One of the most important differences between 4.3 and SOLPS-ITER code versions is that SOLPS-ITER version allows including cross field and diamagnetic drift terms in the equation model.

Cross field (or ExB) drifts are an important part of the tokamak boundary description. Especially relevant for the present thesis is the fact that ExB drifts significantly impact the plasma in the detachment regime for the boundary modeling in the ASDEX Upgrade geometry [17] [18]. In this regime the plasma becomes cold and this leads to a drop of the plasma conductivity. In order to maintain the plasma current the parallel electric field in this region significantly increases and drift fluxes become an important contributor to the particle transport and lead to the particle redistribution in the divertor. For instance, particle transport from the outer to the inner divertor target in ASDEX Upgrade geometry modeling is largely caused by drifts [19].

These drifts terms introduced significant numerical complications which made it impossible to include them in SOLPS 4.3 modeling. In 2001 [20] modifications to the SOLPS model equations were made, which made it possible to include drift terms in the modeling in a self-consistent manner. In 2009 further modifications were made which allowed modeling of the H-mode regimes with drifts [5].

The initial ITER divertor design database was created using the SOLPS 4.3 code version and did not include any drift effects. Part of the present thesis analysis is directed towards studying the impact of the drifts on the ITER simulations. The results obtained in the thesis, indicate a lower importance of the fluid drifts for

ITER parameters than for a smaller device (ASDEX Upgrade parameters) for high divertor neutral pressures.

A possible explanation can be given on the basis of the different magnetic field, which is at least two times larger in ITER and weakens the ExB drift fluxes. Another possible effect, which can explain the smaller impact of the drifts on ITER is the finite length of the cold plasma layer formed in the detachment regime. Numerical modeling of ITER and ASDEX Upgrade geometry gives initial indication that this length does not increase with the machine size. Thus while in the ASDEX Upgrade geometry the whole divertor area cools down during the detachment operations, in ITER cold plasma layers might only occur in the strike point vicinity. In this case the private flux region in ITER will stay relatively hot and a large electric field, which causes significant drift flux in this area, will not be formed. This explanation is still rather preliminary and needs to be supported or dismissed by further research.

Further important findings made in the present thesis relate to impurity transport. Differences between nitrogen and neon transport in ASDEX Upgrade and ITER geometries were investigated and a few important conclusions have been made:

- In the modeling results the parallel momentum balance for impurity in the scrape off layer (SOL) is to a large extent determined by the balance of the friction and thermal gradient forces, acting on the impurities. These forces balance each other in almost the whole SOL, apart from a narrow layer near the divertor targets. Other forces such as the pressure gradient force, electric force, impurity partial pressure gradient force, etc. are at least one order of magnitude lower.
- The balance of the friction and thermal forces acting on the impurity ions allows the evaluation of the parallel velocity of the impurities with respect to that of the main ions. The expression, obtained for the impurity velocity consists mainly of the main plasma parameters and does not contain a strong dependence on the impurity parameters.
- Impurity retention or leakage in the considered modeling results is found to be determined by the interplay of the position of the impurity ionization front and the position of the impurity flow stagnation point in the near SOL.
- The position of the impurity near SOL stagnation point is to a large extent determined by the main ions stagnation point position, which, in turn, is coupled to the main ion ionization front.

- In the comparison of nitrogen and neon retention, it is important to note that due to the ionization efficiency of N, Ne and D, the latter is always ionized geometrically between N and Ne (further away from the target than N, closer to the target than Ne, distance measured in the direction parallel to the magnetic field). Ne is ionized further away from the target and N is ionized closer to the target. Therefore N will always be better retained in the divertor volume than Ne - for both ASDEX Upgrade and ITER geometries.

- Despite the previous statement, the analyzed modeling results show that it is possible to use both N and Ne as ITER divertor radiating impurity, in contrast to AUG where only N can be used. The radiated power distribution differs significantly between the two devices. In ITER the radiated power stays closer to the divertor targets while in ASDEX Upgrade geometry a significant amount of power is found to be radiated in the upper SOL and for the ASDEX Upgrade Neon seeded case more than 10% of the radiated power comes from the core region.

- The different radiative patterns for N and Ne in ASDEX Upgrade partially reproduce experimentally observed phenomena. Due to the absence of the self-consistent transport coefficients and time dependence in the model used it is impossible to get a complete picture for the N and Ne exhaust difference. Nevertheless in the modeling for the same main plasma backgrounds and the similar total radiated power a different distribution of the radiated power between the regions is obtained. More power coming from the core for Ne seeded case suggests worse machine performance and possible impurity accumulation driven by Ne seeding. These effects can be explained by the lower divertor retention of Ne and stronger recycling fluxes.

- For ITER similar radiated power distributions are obtained in the Ne and N seeded cases. Results with drifts do not differ significantly from the old SOLPS 4.3 database conclusions, which suggest the possibility to use Ne for the ITER power exhaust.

Most of the present findings are explained in the Chapter 7 of this thesis.

Chapter 2 of the thesis introduces the basic phenomena of the tokamak boundary physics, which are important for the discussion of the results. These phenomena include detailed explanations of the divertor concept; plasma properties in the divertor region, different regimes of the power exhaust in the divertor configuration; fluid drifts in the tokamak plasma and their effect on the plasma parameter distributions.

After all the important background physics is discussed, Chapter 3 covers the basic transport modeling methodology. The Braginskii equations are presented and discussed there.

The SOLPS-ITER equations are presented in Chapter 4 together with the boundary condition for these equations and the geometry of the SOL used in the modeling.

Chapter 5 is the first chapter, based on the actual work performed in the PhD project framework, and discusses the code modification. This modification concerns the parallel momentum balance equation in the code, and was crucial for obtaining many of the physics results presented in this thesis. The modification consists of a generalized parallel momentum balance description in the SOLPS-ITER code [21].

Chapter 6 focuses on the modeling results, obtained with the modified version of the SOLPS-ITER code. Modeling input parameters and modeling results are presented there.

In Chapter 7, the analysis of this results is presented. The physics findings obtained in the process of this analysis, are presented and discussed there.

Conclusion and outlook finalize the thesis.

Chapter 2

Boundary plasma concepts

Magnetic confinement in a tokamak does not prevent 100% of the plasma particles from escaping. Particles escape both in the direction parallel and perpendicular to the magnetic field. While the radial escape of the plasma is rather slow, the parallel one is very efficient - particles escape with their thermal velocity, which in the case of the fusion plasma often creates heat flow sufficient for damaging the plasma facing components. Another effect of plasma surface interaction (PSI) is the contamination of plasma by impurity particles, sputtered from the material surface.

In order to limit both effects: components damaging and plasma contamination in fusion devices, limiter and divertor configurations were introduced.

2.1 Limiter and divertor configurations

In the limiter and divertor configurations the area inside the chamber becomes split in the confined area (core) and boundary layer (SOL, scrape-off-layer). The magnetic surface between these two is called Last Closed Flux Surface (LCFS) or separatrix.

SOL consists of the so-called open magnetic field lines. In reality these magnetic field lines are still closed, but they intersect the material element, so the particles trajectories on these lines are not closed.

2.1.1 Limiter Configuration

The limiter configuration is a tokamak chamber configuration with a material element, physically limiting the plasma. Example of the limiter configuration on the ASDEX Upgrade tokamak is shown in Fig 2.1, where the plasma is limited by the HFS (High Field Side) heatshield [2].

In the case of limiter configuration there is no strong separation between open and closed magnetic surfaces. This leads to two major drawbacks: direct contact of

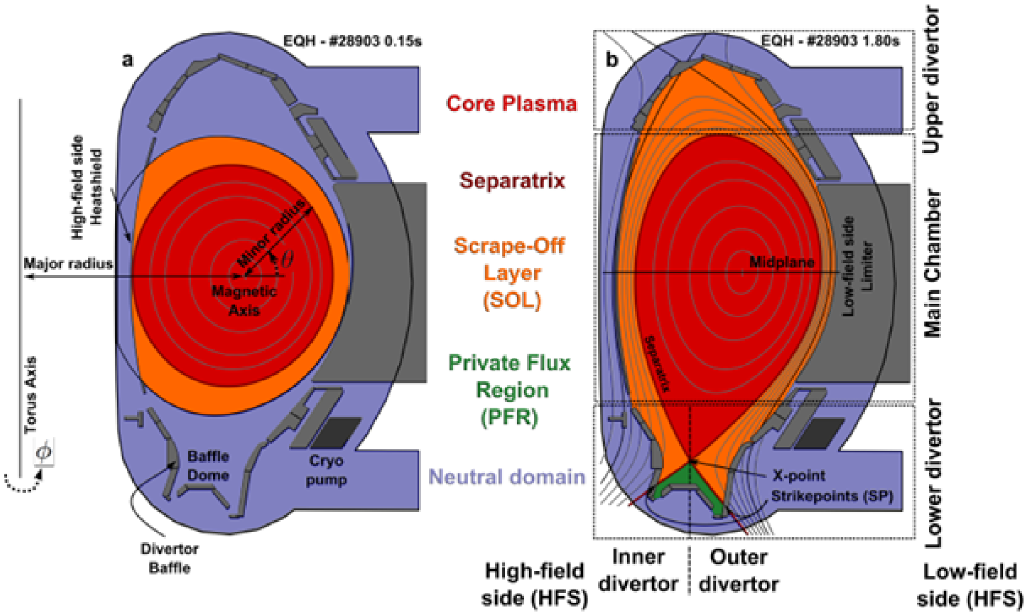

Figure 2.1: ASDEX Upgrade limiter (on the left) and LSN divertor configurations. Adapted from [2]

the hot and dense core plasma with the limiter element and strong transport of the limiter material into the core plasma.

Plasma density outside of the LCFS in the limiter configuration decreases monotonically. Most of the particles reach the limiting structure by fast transport parallel to the magnetic field before they can reach the wall by the slower radial transport. The width of the SOL is determined by the balance of the parallel and radial transport [22].

2.1.2 Divertor configuration

A more advanced plasma limiting configuration is called a divertor. In this configuration, separation of the closed and the open field lines is done through specific shaping of the confining magnetic field.

In order to separate the confined region additional currents are introduced creating a point (or a number of points) in which the poloidal magnetic field is equal to zero (X-point). In this configuration the core plasma is confined without direct proximity to the material surfaces.

The separatrix contacts the special areas of the magnetic chamber, called divertor targets; the points of this contact are called strike points. They become the most intense Plasma Surface Interaction (PSI) area.

The most studied type of the divertor configuration has one X-point in the bottom of the device. This configuration is called Lower Single Null (LSN) and is intensively studied on many tokamaks including ASDEX Upgrade.

An example of the ASDEX Upgrade LSN magnetic configuration is shown on the right of Fig 2.1.

In Fig 2.1 detailed designations of all the elements of the magnetic geometry and chamber structure of ASDEX Upgrade are given. To discuss the tokamak SOL it is important to define the equatorial midplane (midplane in the Fig 2.1) - a horizontal plane in the poloidal cross section at the height of the magnetic axis. The outer midplane (point of $\Theta = 0$ in Fig 2.1) is often taken as a reference "upstream point" in the discussion of power and particle transport.

The region of open field lines is called the SOL (orange region in the Fig 2.1), apart from the region of the open field lines between the two legs of the separatrix. This region (marked green in the Fig 2.1) is called the private flux region (PFR).

It is common to call the region of the SOL, located poloidally above the X-point the upstream region (main SOL), and the region below the X-point is usually called the divertor region.

For ITER a LSN divertor configuration is planned due to the simplicity of this configuration. More complicated magnetic configurations (double null configuration, snowflake divertor, etc.) are less studied. Another reason to keep the ITER divertor configuration simple is the need to protect all additional magnetic structure from neutron fluxes, which is simpler in the LSN configuration.

2.2 Sheath in the tokamak SOL

At the plasma-surface interface in front of the divertor target specific arrangement of the electric potential occurs. The closest to the target region of this formation is called the sheath. The structure of this layer is shown in Fig. 2.2 . It is important to discuss this layer since it sets the ion parallel velocity in the SOL to the ion sound speed, $c_s = \sqrt{\frac{T_e + T_i}{m_i}}$. This condition should be satisfied in the vicinity of the divertor targets.

Due to the much lower mass of the electron in comparison with ions they travel to the surface faster. This causes a negative charge of the surface and a potential builds up, which slows down the electrons and speeds up the ions. The plasma

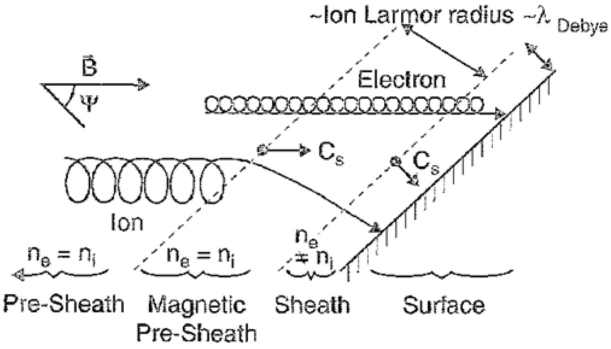

Figure 2.2: Ion and electron trajectories in the various sheath regions near the target surface. Reproduced from [22]

quasineutrality condition in this layer is violated and the width of this layer is equal to the Debye radius. The thickness of the sheath layer is defined by the scale on which it is possible to violate plasma quasineutrality condition. For the sheath layer the Bohm criterion exist; velocity of plasma ions on the sheath entrance should be larger than the local sound speed.

Due to the presence of the large toroidal magnetic field in the tokamak plasma the incidence angle of the plasma particles to the target can be very far from the normal direction. In this case a so called magnetic pre-sheath layer is formed. This layer is quasineutral but it has the same condition at the entrance: ion velocity should be larger or equal than the sound speed.

Since the bulk velocity in general cannot be higher than the sound velocity, in the simple approximation the plasma velocity in the SOL is assumed to be equal to the sound speed. This boundary condition for ion velocity is applied on both divertor targets.

2.3 Divertor asymmetries

Inner and outer divertor targets (located correspondingly on the HFS and the LFS of the divertor), Fig 2.1, can feature significantly different plasma properties on them. Usually the plasma density is higher at the inner (HFS) target, and the temperature at that target and the heat flux, received by it, is lower.

Reasons for the divertor power asymmetries:

- Magnetic flux surfaces are more compressed on the LFS compared to the HFS. This is caused by the Shafranov shift - displacement of the center of the magnetic equilibrium outwards from the center of the tokamak. This introduces stronger gradients of the plasma parameters at the LFS [22]. If the cross field transport is assumed to be proportional to the gradients strength, this results in even more power being deposited on the outer target.

- Ballooning type radial transport [23] is present only on the LFS of the tokamak due to the unfavorable curvature there. This amplifies the amount of the power deposited on the outer target;
- ExB drifts through the private flux region can significantly redistribute the particles from the outer to the inner divertor target.

In order to explain the asymmetry in the particle distribution, cross field drifts have to be introduced.

2.4 Drifts in the tokamak

2.4.1 Larmor motion

In order to discuss the motion of the particles in the tokamak it is important to understand the motion of the charged particles in a homogeneous magnetic field. The equation of motion of one charged particle in a magnetic field is as follows:

$$m_a \frac{d\mathbf{V}}{dt} = z_a e \left[\mathbf{V} \times \mathbf{B}\right] \tag{2.1}$$

Here $\mathbf{V}$ is the particle velocity, m_a is the particle mass, $z_a e$ is the particle charge, $\mathbf{B}$ is the magnetic field.

The velocity component parallel to the magnetic field in these conditions is constant:

$$m_a \frac{d\mathbf{V}_{||}}{dt} = 0; \mathbf{V}_{||} = const \tag{2.2}$$

Total energy of the motion in the direction parallel to the magnetic field is also constant, since the only force, acting on the particle, is perpendicular to this direction.

$$m_a \frac{d\mathbf{V}_{||}^{\mathbf{2}}}{dt} = 0; \mathbf{V}_{||}^{\mathbf{2}} = const \tag{2.3}$$

The equation of the particle motion in the plane, perpendicular to the magnetic field describes a circular motion.

$$m_a \frac{d\mathbf{V}_{\perp}}{dt} = z_a e \left[\mathbf{V}_{\perp} \times \mathbf{B}\right]; \tag{2.4}$$

$$\mathbf{V}_{\perp} = |\mathbf{V}_{\perp}| \left(\boldsymbol{e}_x \cos(\omega_c \mathrm{t}) + \boldsymbol{e}_y \sin(\omega_c \mathrm{t})\right) \tag{2.5}$$

Here $\omega_c = \frac{z_a e|\mathbf{B}|}{m}$ - Larmor frequency.

In order to connect the absolute value of the perpendicular velocity with the radius of the circle in the circular motion, one takes into account that the centrifugal force of the circular motion has to be balanced by the Lorentz force:

$$\frac{m_a \mathbf{V_\perp^2}}{\rho_c} = z_a e |\mathbf{V}_\perp||\mathbf{B}|; \rho_c = \frac{|\mathbf{V}_\perp|}{\omega_c} \tag{2.6}$$

Summing up the information about the $\mathbf{V}_{||}$ and $\mathbf{V}_\perp$, the particle motion in a constant magnetic field can be described as the spiral motion - motion with the constant velocity along the magnetic field and circular motion in the plane perpendicular to the magnetic field.

2.4.2 Drifts of the particles in the magnetic field

For any force $\mathbf{F}$, acting on the particle in the homogeneous magnetic field the drift velocity corresponding to this force can be derived. In order to do so one has to consider the equation of motion for this particle:

$$m_a \frac{d\mathbf{V}}{dt} = \mathbf{F} + z_a e \left[\mathbf{V} \times \mathbf{B}\right] \tag{2.7}$$

The component of the velocity, parallel to the field, will give the uniformly accelerated motion:

$$m_a \frac{d\mathbf{V}_{||}}{dt} = \mathbf{F}_{||} \tag{2.8}$$

The component of the velocity, perpendicular to the magnetic field can be split in the constant drift velocity and the Larmor motion velocity:

$$\mathbf{V}_\perp = \mathbf{V_d} + \mathbf{V}_{\boldsymbol{\omega}} \tag{2.9}$$

Here Larmor motion contribution cancels the cross product part in the right hand side of the equation of motion (2.7) and the time derivative in the left hand side. For the drift contribution the following equation is obtained:

$$\mathbf{F}_\perp + z_a e \left[\mathbf{V_d} \times \mathbf{B}\right] = 0 \tag{2.10}$$

Making the cross product of this equation with the magnetic field and taking into account expression $[[\mathbf{A} \times \mathbf{B}] \times \mathbf{B}] = -\mathbf{B}^2\mathbf{A}$ one obtains the following expression for the drift velocity:

$$\mathbf{V_d} = \frac{[\mathbf{F} \times \mathbf{B}]}{z_a e |\mathbf{B}|^2} \tag{2.11}$$

2.4.3 ExB drifts

Due to the presence of an electric field in the tokamak plasma particles experience drifts, which are called ExB drifts. Velocity of these drifts can be calculated by eq. 2.11 and since the electric force, acting on the charged particle is $\mathbf{F} = z_a e\mathbf{E}$ the ExB drift velocity defined as:

$$\mathbf{V_{ExB}} = \frac{[\mathbf{E} \times \mathbf{B}]}{|\mathbf{B}|^2} \tag{2.12}$$

Since the drift velocity $\mathbf{V_{ExB}}$ is independent of the particle charge or mass, the ExB drift does not cause charge separation (because electrons and ions drift in the same direction) and does not cause any plasma current.

The ExB drifts can be split in the two categories: drifts due to the radial electric field and drifts due to the poloidal electric field. Resulting drift fluxes would be directed poloidally for the radial electric field and radially for the poloidal electric field.

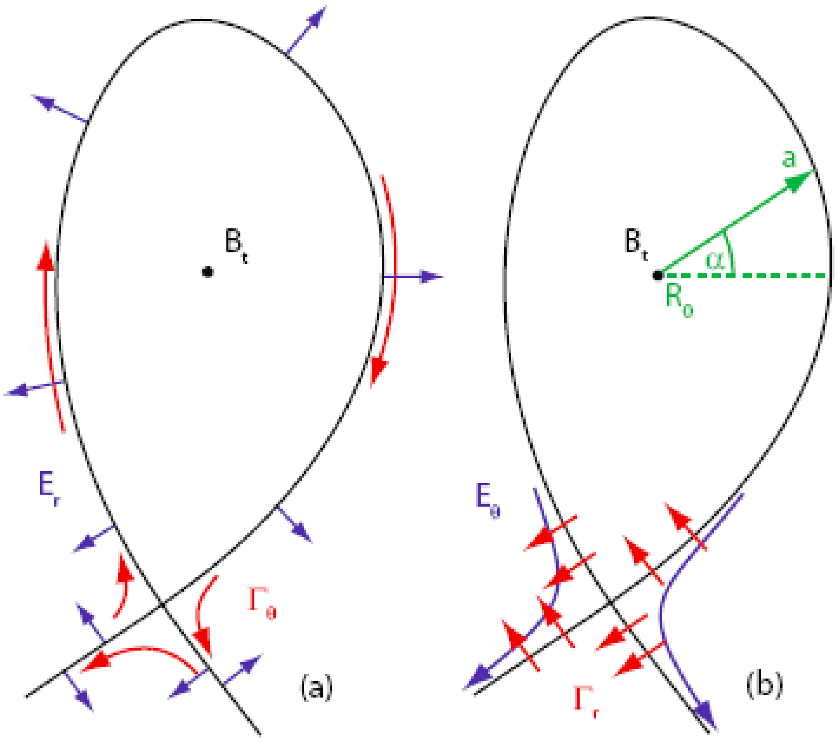

Figure 2.3: An example of the poloidal (a) and radial (b) particle fluxes caused by the ExB drifts shown in red. Corresponding electric field is shown in blue. Reproduced from [3]

According to the recent SOLPS-ITER modeling studies, supported by the theoretical explanations [4] poloidal drift flux though the private flux region is one of the main contributor in the divertor densities asymmetry, discussed above.

Radial electric fields in the boundary plasmas are usually formed due to the presence of the temperature and density gradients.

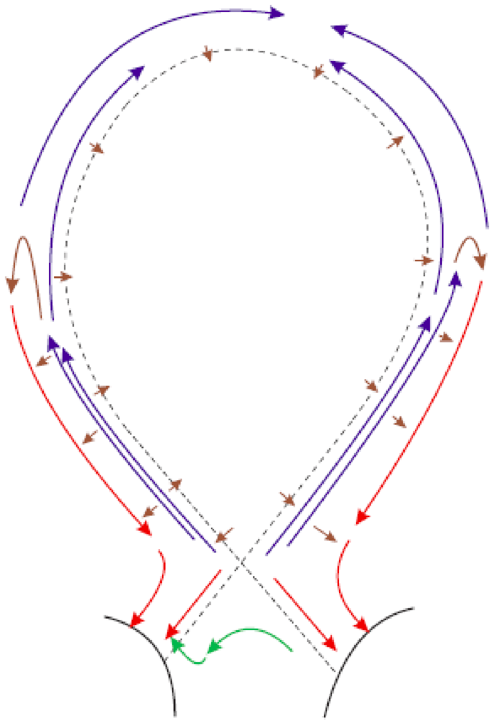

Figure 2.4: An example of the complicated pattern of the ion flow in the SOL. ExB drift which moves particles from the outer to the inner target is shown in green. Reproduced from [4]

2.4.4 ∇B drifts

The magnetic field in the tokamak has an intrinsic gradient. The force, acting on one particle, moving on the Larmor orbit, can be evaluated in the following way:

$$\mathbf{F} = \mu \nabla \mathbf{B} = \frac{m|\mathbf{V}_\perp|^2}{2|\mathbf{B}|} \nabla \mathbf{B}, \tag{2.13}$$

where $\mu = \dfrac{m|\mathbf{V}_\perp|^2}{2|\mathbf{B}|}$ is the magnetic moment of the charged particle experiencing the Larmor motion.

The resulting drift velocity, calculated using 2.11, is

$$\mathbf{V}_{\boldsymbol{\nabla}\mathbf{B}} = m|\mathbf{V}_\perp|^2 \frac{[\mathbf{B} \times \boldsymbol{\nabla}\mathbf{B}]}{2ez_a|\mathbf{B}|^3} \tag{2.14}$$

This velocity is dependent on the particle mass and charge. Thus, the absolute value and the direction of the **∇B** drift differ for electrons and ions and this creates a charge separation.

The toroidal geometry of the tokamak leads to the magnetic field gradient proportional to 1/R and directed horizontally towards the center of the torus. According to the eq. 2.14 the corresponding drift velocity is directed vertically and in ASDEX

Upgrade geometry the standard direction of the $\nabla\mathbf{B}$ drift is down for the ions and up for the electrons. The charge separation, which is created by this drift is compensated by the return flows along the magnetic field lines, called Pfirsch-Schlueter flow.

Chapter 3

Transport equations

The main methodological strategy of this PhD project was transport modeling of the edge plasma with the SOLPS-ITER transport code. This code is one of the transport codes for the SOL plasma which exist in the field, including EMC3-EIRENE[24], SOLEDGE2D-EIRENE [25], EDGE2D-EIRENE [26] and UEDGE [27] codes.

The model equations, which serve as the basis of all transport codes for plasma boundary, are the transport equations. These equations were derived for a hydrogen plasma without impurities in [28].

The derivation of the transport equations is discussed in the present chapter.

3.1 Kinetic approach to the plasma description

The derivation of the transport equations in [28] starts from the general kinetic description of the plasma with a distribution function characterizing each particle component.

By definition, the distribution function f_a (for particles of sort a) is specified in such a way that the expression $f_a(\mathbf{r}, \mathbf{v}, t)drdv$ represents the number of particles in an infinitesimal six dimensional volume $drdv$.

Once the distribution function is introduced, the behavior of plasma can described by the system of kinetic equations (Boltzmann equations):

$$\frac{\partial f_a}{\partial t} + \frac{\partial}{\partial x_b}(v_b f_a) + \frac{\partial}{\partial v_b}\left(\frac{F_{ab}}{m_a} f_a\right) = C_a \tag{3.1}$$

Here v is the microscopic velocity of particles of sort a, F_a is the force, acting on these particles, m_a is their mass and C_a is the collisional operator, b is a summing index in the divergences.

For plasma particles in the electrical ($\mathbf{E}$) and magnetic ($\mathbf{B}$) fields $\mathbf{F}_a$ would be as follows:

$$\mathbf{F}_a = \mathrm{z}_a \mathrm{e} \mathrm{n}_a \left(\mathbf{E} + [\mathrm{v}_a \times \mathbf{B}]\right) \tag{3.2}$$

Here z_a is the charge of species a.

The kinetic description is one of the most mathematically complex approaches in plasma physics. For many applications this description can be simplified if certain assumptions are made. For instance, moments of the distribution function can be used to describe the plasma evolution in a fluid approach. Limitations of this approach come from the assumption of a high plasma collisionality and will be discussed below.

3.2 Fluid approach to the plasma description. Moments of the distribution function

The fluid approach is based on transport equations as suggested in [1]. They describe the behavior of the distribution function moments - macroscopic parameters of plasma particle species "a": density (n_a), velocity (v_a) and temperature (T_a). These parameters are defined as follows:

Density of plasma particles of sort "a":

$$n_a(\mathbf{r}, t) = \int f_a(\mathbf{r}, \mathbf{v}, t) d\mathbf{v} \tag{3.3}$$

Macroscopic velocity of the plasma particles of sort "a":

$$\mathbf{v}_a(\mathbf{r}, t) = \frac{1}{n_a} \int \mathbf{v} f_a(\mathbf{r}, \mathbf{v}, t) d\mathbf{v} \tag{3.4}$$

Thermal energy of the plasma particles of sort "a", referred in this text as the temperature:

$$\mathrm{T}_a(\mathbf{r}, t) = \frac{m_a}{3n_a} \int (\mathbf{v} - \mathbf{v}_a)^2 f_a(\mathbf{r}, \mathbf{v}, t) d\mathbf{v} \tag{3.5}$$

3.3 Momentum equations

To obtain equations describing dynamics of distribution function moments Eq. (3.3) - Eq. (3.5), the integration of the Boltzmann equation 3.1 in velocity space with the weights (defined below) is required. In the Braginskii equation system, which serves as the basis of the fluid approach, only the equations for the first three moments are used. Therefore only the integration of the kinetic equation with the weights "1", "$m_a v$" and "$m_a v^2$" is performed. After this integration is done, transport equations are obtained. They are briefly discussed below. The continuity equation (particle balance equation):

$$\frac{\partial n_a}{\partial t} + \mathrm{div}(\Gamma_a) = S_a \tag{3.6}$$

Here Γ_a - flow of the plasma particles of the sort "a", S_a - the source (or the sink) of these particles, which represents the change of the particle content in the system due to the interaction with the particles of other sorts. The source is defined by the collisional operator: $S_a = \int C_a dv$

The momentum balance equation:

$$m_a n_a \frac{d_a \mathrm{v}_{aj}}{dt} = -\frac{\partial p_a}{\partial x_j} - \frac{\partial \pi_{ajk}}{\partial x_k} + z_a e n_a \left(E_j + [\boldsymbol{v}_a \times \mathbf{B}]_j\right) - R_{aj} \tag{3.7}$$

Here p_a- partial pressure of particles of the sort "a", π_{ajk}- stress (viscosity) tensor,R_{aj}- general friction force of the plasma particles of the sort "a" with the other plasma particles (including the actual friction force and the thermal force),
$\frac{d_a}{dt} = \frac{\partial}{\partial t} - (\boldsymbol{v}_a \cdot \nabla)$ - the material derivative.

Definitions of the moments of the higher order:

- Plasma pressure: $p_a = n_a T_a$
- Stress tensor: $\pi_{ajk} = m_a n_a \int \left((v_j - v_{aj})(v_k - v_{ak}) - \delta_{jk} (\mathbf{v} - \mathbf{v}_a)^2 f_a(\mathbf{r}, \mathbf{v}, t)\right) d\mathbf{v}$
- General friction force $R_{aj} = \int m_a (v_j - v_{aj}) C_a(\mathbf{r}, \mathbf{v}, t) dv$

The general friction force R_{aj} represents the mean change in the momentum of the particles of a given species due to collisions with all other particles.

This equation (3.7) represents the equation of motion for a plasma volume: in the left hand side the material derivative gives the acceleration of this volume and the right hand side represents the forces, acting on it: pressure gradient, divergence of the stress tensor, electrical force, Lorentz force and general friction force.

Heat balance equation (equation for the transport of internal energy):

$$\frac{3}{2} n_a \frac{d_a T_a}{dt} + p_a \mathrm{div} \boldsymbol{v}_a = -\mathrm{div} \mathbf{q}_a - \pi_{ajk} \frac{\partial v_{aj}}{\partial x_k} + \mathrm{Q}_a \tag{3.8}$$

Here $\mathbf{q}_a$- heat flux, Q_a - heat source. They are defined as follows:

$$\mathbf{q}_a(\mathbf{r}, t) = \frac{m_a n_a}{2} \int (\mathbf{v} - \mathbf{v}_a)(\mathbf{v} - \mathbf{v}_a)^2 f_a(\mathbf{r}, \mathbf{v}, t) d\mathbf{v} \tag{3.9}$$

$$\mathrm{Q}_a(\mathbf{r}, t) = \int \frac{m_a (\mathbf{v} - \mathbf{v}_a)^{\mathbf{2}}}{2} C_a f_a(\mathbf{r}, \mathbf{v}, t) d\mathbf{v} \tag{3.10}$$

3.4 Momentum equations closure

In each of the equations presented for evolution of the plasma moment of a certain order (3.6) - (3.8), moments of the next order are used. For instance, in the continuity equation (3.6) (density dynamics, moment of the zero order) there is the velocity present (moment of the first order). In the momentum balance equation (which defines the averaged velocity - first order moment - dynamics) there are terms, which include temperature and viscosity (moments of the second order).

To obtain a closed system of fluid equation, which one can implement in the code and solve numerically, it is necessary to express π_{ajk}, p_a , R_{aj} , $\boldsymbol{q}_a$ and Q_a through the first three moments n_a, $\mathbf{v}_a$, T_a and their spatial derivations. This can be done phenomenologically or by kinetic methods. Latter can be only used if the approximate solution for the kinetic equation is obtained. For instance, this can be done in high collisionality conditions [28] and then the final equation system would represent the fluid approach set of equations.

The criteria for high collisionality are as follows: mean free path (MFP) of plasma particles (path between collisions) should be much smaller than the characteristic scale length of the plasma; collision frequency should be higher than the characteristic times. Characteristic scale lengths of plasma are determined by the gradient lengths of the plasma parameters. This condition is always violated near the material boundary where plasma density drops rapidly and the characteristic length becomes smaller. In these areas, a kinetic approach is necessary (magnetic sheath). In the SOLPS-ITER equations this problem is treated via sheath boundary condition at the material targets boundaries, which approximates the results obtained in the kinetic approach.

If the high collisionality condition is fulfilled, the distribution function will be close to a Maxwellian $f_a = \dfrac{n_a}{(2\pi T_a/m_a)^{3/2}} e^{-\frac{m_a}{2T_a}(\mathbf{v}-\mathbf{v}_a)^2}$.

In [28] the kinetic equation then solved by using a perturbation method and the distribution function is approximated in the following way:

$$f_a(\mathbf{r}, \mathbf{v}, t) = f_a^0 + f_a^1 = \frac{n_a}{(2\pi T_a/m_a)^{3/2}} e^{-\frac{m_a}{2T_a}(\mathbf{v}-\mathbf{v}_a)^2} + f_a^1; |f_a^1| << f_a^0 \tag{3.11}$$

In this formulation the Maxwellian function and its derivatives are determined uniquely by the first three moments and their derivatives, the correction f_a^1 in the final formulation is determined by the same parameters and the effects, disturbing the Maxwellian - electric and magnetic fields and the parameter gradients. The method which is used to obtain the perturbed distribution function is usually based on the perturbation decomposition into generalized Laguerre polynomials [29].

Once the perturbed distribution function is found, relations between moments π_{ajk}, p_a, R_{aj} , $\boldsymbol{q}_a$, Q_a, and the effects, causing these forces can be found. Coefficients of proportionality are called transport coefficients.

For the present thesis the most important transport coefficients are the ones in the general friction force. For the simple plasma the expression from [28] is as follows:

$$\mathbf{R} = \mathbf{R}^{\mathbf{u}} + \mathbf{R}^{\mathbf{T}} \tag{3.12}$$

$$\mathbf{R}^{\mathbf{u}} = -n m_e \nu_{ei} \left(0.51\boldsymbol{u}_{||} + \boldsymbol{u}_{\perp}\right) \tag{3.13}$$

$$\mathbf{R}^{\mathbf{T}} = -0.71 n \nabla_{||} T_e - \frac{3}{2}\frac{n\nu_{ei}}{\omega_{ce}}\left[\frac{\mathbf{B}}{|\mathbf{B}|} \times \nabla T_e\right] \tag{3.14}$$

Here $\mathbf{u} = \mathbf{v_e} - \mathbf{v_i}$; $\nu_{ei} = \dfrac{4\sqrt{2\pi}}{3}\left(\dfrac{e^2}{4\pi\epsilon_0}\right)^2 \dfrac{n\Lambda}{m_e^{1/2} T_e^{3/2}}$ - the collisional frequency.
For the multicomponent plasma these expressions have a more complicated form which is presented in chapter 5 of the present thesis.

The explicit expressions of the other transport coefficients can be found in [28] for the simple plasma. Derivation of the transport coefficients for multicomponent plasma is done in [29].

Chapter 4

SOLPS-ITER code

One of the first numerical implementations of the transport equations (3.6) - (3.8) was done for studying of the impurity flow along magnetic field lines in a collisional tokamak scrape-off layer by B. Braams in 1987 [30]. This implementation was done in the code called B2. This code initially was designed as a tool for the impurity transport studies in tokamak boundary plasmas. It consisted of the Braginskii solver for multifluid plasma (for the dynamics parallel to the magnetic field). Since the theoretical model of the anomalous radial transport in the tokamak SOL was not yet fully developed, radial transport has been prescribed as an external input parameter. For the radial direction diffusive transport was assumed with prescribed profiles of the anomalous diffusion coefficients. Classical diffusion in the radial direction was neglected due to its insignificance in comparison with the anomalous transport.

Since the first version of the code, it was actively used for SOL studies. The code has been developed by the joint effort of the fusion community, including the coupling to the Eirene MC code for neutrals [31] modification of the electric drift and charge conservation equation treatment [20],[5]. The SOLPS 4.3 code version was used by A. S. Kukushkin to create a database for ITER reactor divertor design [15],[32].

The modern version of the code was launched by ITER Organization in 2012 [33] with the code name change to SOLPS-ITER. This version was updated in 2016 to the 3.0.6 version [16] which is used in the present thesis.

Part of this update consisted of the generalization of the parallel momentum balance equation (PMBE) used in the code [21]. This generalization consisted of the replacement of the simplified version of PMBE with the original Braginskii form and formulation of the friction and thermal force terms suitable for non trace impurity modeling. This modification was done in the framework of the present thesis.

4.1 Geometry

The SOLPS-ITER equations are given in toroidal geometry, but do not include any variation of the variables in the toroidal (z) direction. Coordinates are denoted as follows: x - for poloidal direction, y - for radial direction, z - toroidal coordinate (absent in the equations and used only for the geometry description).

The coordinate system is orthogonal and for its description in the code gathering equations metric coefficients are used. These coefficients (Lamé coefficients) are defined as follows:

$$h_x = \frac{1}{\|\nabla x\|}; h_y = \frac{1}{\|\nabla y\|}; h_z = \frac{1}{\|\nabla z\|} = 2\pi R \tag{4.1}$$

These coefficients are used to define the derivatives in the code coordinates. It is also necessary to define the volume of one computational cell :$\sqrt{g} = h_x h_y h_z$. Poloidal projections of the components is done by using factor $b_x = B_x/|B|$. The code geometry on the ASDEX Upgrade tokamak mesh example is demonstrated in 4.1.

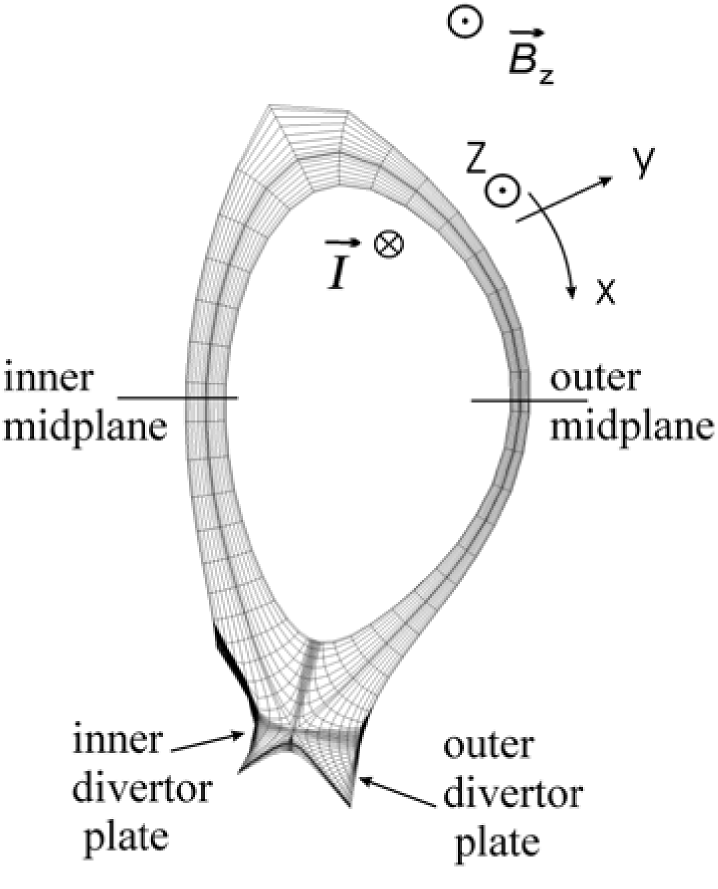

Figure 4.1: Coordinate system of SOLPS-ITER code on the ASDEX Upgrade tokamak mesh example, from [5].

4.2 Continuity equation

The continuity equation (3.6) in the SOLPS-ITER code is implemented in the following way:

$$\frac{\partial n_a}{\partial t} + \frac{1}{\sqrt{g}}\frac{\partial}{\partial x}\left(\frac{\sqrt{g}}{h_x}\widetilde{\Gamma}_{ax}\right) + \frac{1}{\sqrt{g}}\frac{\partial}{\partial y}\left(\frac{\sqrt{g}}{h_y}\widetilde{\Gamma}_{ay}\right) = S_a^n, \quad a = 0, 1, \ldots, n_s - 1 \tag{4.2}$$

Index a goes between 0 (indicating the main ions neutrals) to $n_s - 1$ - *the total number of plasma species.* For main ions $a = 1$; each charged state of each modeled ion species is considered as a separate fluid with the separate set of equations solved for it; each sequence of every species starts from the neutral particles, corresponding to this species. An example of the species numbering for the case with D as a main ions and N as an impurity:

$$D^0 : a = 0, D^{+1} : a = 1; N^0 : a = 2; N^{+1} : a = 3 \ldots N^{+7} : a = 9 \tag{4.3}$$

If the SOLPS-ITER code is run in a way such that neutral particles are treated in Eirene, equations, corresponding to the neutral particles, are not solved on the B2 side (applies for all equations, described in this chapter).

The source term S_a^n in the l. h. s. of equation 4.2 corresponds to the particles of the sort a appearing through ionization or disappearing through recombination. If the SOLPS-ITER code is run in a way such that neutral particles are treated in Eirene, this term for the first ionization state comes as an Eirene source. For the ionization and recombination within upper charged states these processes are treated by B2 part of the code. The fluxes appearing in equation (4.2) are defined as follows:

- Poloidal flux:

$$\begin{aligned}\widetilde{\Gamma}_{ax} = &\left(b_x v_{\|a} + v_{ax}^{(E)} + v_{ax}^{(AN)}\right) n_a \\ &- D_{n,a}\frac{1}{h_x}\frac{\partial n_a}{\partial x} - \left(\frac{1}{B^2} - \frac{1}{\langle B^2\rangle}\right)\frac{B_z}{e}\frac{1}{h_y}\frac{\partial n_a T_i}{\partial y}\end{aligned} \tag{4.4}$$

- Radial flux:

$$\begin{aligned}\widetilde{\Gamma}_{ay} = &\left(v_{ay}^{(E)} + v_{ay}^{(AN)}\right) n_a + \frac{1}{e n_a}\left(j_y^{(in)} + j_y^{(vis\|)}\right) \\ &- D_{n,a}\frac{1}{h_y}\frac{\partial n_a}{\partial y} + \left(\frac{1}{B^2} - \frac{1}{\langle B^2\rangle}\right)\frac{B_z}{e}\frac{1}{h_x}\frac{\partial n_a T_i}{\partial x}\end{aligned} \tag{4.5}$$

The coefficient $D_{n,a}$ here corresponds to the anomalous diffusion process and is set as an input parameter corresponding to the desirable shape of plasma density profile. In H mode modeling, the presence of the transport barrier has to be taken into account by reducing the anomalous transport coefficients in the narrow region in the separatrix vicinity.

ExB drift velocities are defined as follows:

$$v_{ax}^{(E)} = \frac{B_z}{B^2}\frac{1}{h_y}\frac{\partial\phi}{\partial y} \tag{4.6}$$

$$v_{ay}^{(E)} = \frac{B_z}{B^2}\frac{1}{h_x}\frac{\partial\phi}{\partial x} \tag{4.7}$$

Anomalous pinch velocities $v_{ax,y}^{(AN)}$ correspond to the plasma movement in the radial direction caused by processes which are not included in the SOLPS-ITER model. These velocities might be used to obtain specific density profiles.

Terms $\left(\frac{1}{B^2} - \frac{1}{\langle B^2\rangle}\right)\frac{B_z}{e}\frac{1}{h_y}\frac{\partial n_a T_i}{\partial y}$, $\left(\frac{1}{B^2} - \frac{1}{\langle B^2\rangle}\right)\frac{B_z}{e}\frac{1}{h_x}\frac{\partial n_a T_i}{\partial x}$ correspond to the vertical guiding centre drift of ions caused by ∇B. These terms replace diamagnetic drift contributions in the particle flux. These terms are discussed in [5]. Averaged magnetic field is defined as follows:

$$\langle B^2\rangle = \int\oint_{\text{inner boundary}}^{\text{separatrix}} \sqrt{g}B^2 dxdy \Big/ \int\oint_{\text{inner boundary}}^{\text{separatrix}} \sqrt{g}dxdy.$$

Terms in the radial flux proportional to the currents:

$$j_y^{(in)} = -\frac{B_z}{2}\frac{\partial}{h_x\partial x}\left(\frac{1}{B^2}\right)\sum_{a=0,z_a\neq 0}^{n_s-1} m_a n_a v_{a||}^2 \tag{4.8}$$

$$j_y^{(vis||)} = b_z\frac{B_x}{3B^{1/2}}\frac{\partial}{h_x\partial x}\left(\frac{1}{B^2}\right)\sum_{a=0,z_a\neq 0}^{n_s-1} \eta_a \frac{\partial\left(B^{1/2}V_{a||}\right)}{h_x\partial x} \tag{4.9}$$

These terms represent the parts of the flux due to the inertia and viscosity correspondingly. Viscous coefficient is defined as $\eta_a = 4/3 \cdot 0.96\sqrt{2}T_i n_a {z_a}^2 \tau_p b_x^2$, similar to the definition in [28].

4.3 Parallel momentum balance equation

Before the modification of the code made in the present thesis, the following form of the parallel momentum balance equation (PMBE) (implementation of eq. (3.4)) was used in the code:

$$\begin{aligned} m_a\frac{\partial n_a v_{a||}}{\partial t} + \frac{1}{h_z\sqrt{g}}\frac{\partial}{\partial x}\left(\frac{h_z\sqrt{g}}{h_y}\Gamma_{ax}^m\right) + \frac{1}{h_z\sqrt{g}}\frac{\partial}{\partial y}\left(\frac{h_z\sqrt{g}}{h_x}\Gamma_{ay}^m\right) + \\ \frac{b_x}{h_x}\frac{\partial n_a T_i}{\partial x} + \frac{b_x}{h_x}\frac{z_a n_a \partial n_e T_e}{n_e \partial x} \\ = S_{a||}^m + S_{CF||}^m + S_{\mathrm{fra}}^m + S_{\mathrm{Therma}}^{mOLD} + S_{I_a}^m + S_{R_a}^m + S_{CXa}^m \end{aligned} \tag{4.10}$$

Index a goes between 0 (indicating the main neutrals) to n_s-1 - *the total number of plasma species.*

Momentum fluxes are defined as follows:
Poloidal flux:

$$\Gamma^m_{ax} = \begin{cases} m_a v_{||a}\left(\Gamma_{ax}+\Gamma^{(dia)}_{ax}\right) - \eta_{ax}\frac{\partial v_{||a}}{h_x\partial x}; \quad a\neq 1 \\ m_a v_{||a}\left(\Gamma_{ax}+\Gamma^{(dia)}_{ax}\right) + \frac{4}{3}\eta_{ax}\frac{\partial ln(h_z)}{h_x\partial x}v_{||a} - \frac{4}{3}\eta_{ax}\frac{\partial v_{||a}}{h_x\partial x}; \quad a=1 \end{cases} \tag{4.11}$$

Where

$$\Gamma_{ax}+\Gamma^{(dia)}_{ax} = b_x v_{||a}n_a + v^{(E)}_{ax}n_a + 2\widetilde{v}^{(dia)}_{ax}n_a - D^n_a\frac{1}{h_x}\frac{\partial n_a}{\partial x} \tag{4.12}$$

$$\widetilde{v}^{(dia)}_{ax} = \frac{T_iB_z}{z_ae}\frac{\partial}{h_y\partial y}\left(\frac{1}{B^2}\right) \tag{4.13}$$

Radial flux:

$$\Gamma^m_{ay} = m_a v_{||a}\left(\Gamma_{ay}+\Gamma^{(dia)}_{ay}\right) - \eta_{ay}\frac{\partial v_{||a}}{h_y\partial y} \tag{4.14}$$

Where

$$\Gamma_{ay}+\Gamma^{(dia)}_{ay} = \begin{cases} v^{(E)}_{ay}n_a + 2\widetilde{v}^{(dia)}_{ay}n_a + v^{(AN)}_{ay}n_a - D^n_a\frac{1}{h_y}\frac{\partial n_a}{\partial y}; \quad a\neq 1 \\ v^{(E)}_{ay}n_a + 2\widetilde{v}^{(dia)}_{ay}n_a + v^{(AN)}_{ay}n_a + \frac{j^{(AN)}_y+j^{(in)}_y+j^{(vis||)}_y}{e}n_a - D^n_a\frac{1}{h_y}\frac{\partial n_a}{\partial y}; \quad a=1 \end{cases} \tag{4.15}$$

$$\widetilde{v}^{(dia)}_{ay} = -\frac{T_iB_z}{z_ae}\frac{\partial}{h_x\partial x}\left(\frac{1}{B^2}\right) \tag{4.16}$$

The terms in the l. h. s. of the equation 4.10 represent different momentum sources. These sources are: $S^m_{a||}$- viscous momentum source; $S^m_{CF_a}$ - centrifugal momentum source; $S^m_{I_a}$, $S^m_{R_a}$, $S^m_{CX_a}$- momentum sources corresponding to ionization, recombination and charge exchange respectively.

The terms $S^m_{Fr,a}$, $S^m_{Term,a}$, corresponding to friction and thermal forces, are going to be discussed in more detail since these terms were modified in the scope of the present thesis. In the form (3.15) of PMBE, the friction force is implemented in the following way:

$$S^{m\text{OLD}}_{\text{Fr}_a} = \sum_{\substack{b=0 \\ b\neq a, z_a\neq 0, z_b\neq 0}}^{n_s-1} \zeta_p{}^{-1}\sqrt{m_p}\sqrt{\frac{m_am_b}{m_a+m_b}}z_a^2z_b^2n_an_b\left(v_{b||}-v_{a||}\right) \tag{4.17}$$

where $\zeta_p = \dfrac{3}{4\sqrt{2\pi}} \dfrac{\sqrt{m_p} T_i^{3/2}}{\Lambda} \left(\dfrac{4\pi\epsilon_0}{e^2} \right)^2$, Λ - Coulomb logarithm.

$$S^{m\mathrm{OLD}}_{\mathrm{Term}_a} = n_a n_e b_x e {\zeta_p}^{-1} \left(\frac{z_a}{n_e} - \frac{z_a^2}{n_{e^2}} \right) \left[\hat{E}_x - \frac{2.65}{e} \frac{\partial T_i}{h_x \partial x} \right] \tag{4.18}$$

Here $\hat{E}_x = \dfrac{1}{e n_e h_x} \dfrac{\partial n_e T_e}{h_x \partial x} - \dfrac{\partial \phi}{h_x \partial x}$ - modified electric field;
$n_{e^2} = \sum\limits_{a=0}^{n_s-1} z_a^2 n_a$.

Equation 4.10 exhibits significant modifications compared to the basic equation 3.7. Historically [34] it was necessary to exclude the potential balance equation from the code for numerical reasons. In eq. 4.10 the potential gradient term was replaced by the electron pressure gradient. To make this replacement, the PMBE for ions was combined with the PMBE for electrons. To simplify the result of this operation, the trace impurity assumption was made, and friction and thermal force terms of the l. h. s. of the equation were rewritten accordingly.

Later in [35] the electric field term was returned to the eq 4.10 but not in the initial form, but as an addition to the thermal force term, with trace impurity assumption remaining in place.

The generalization of PMBE made in this thesis, which allowed to return to the electric field description used in 3.7, is discussed in the chapter 5. The new form of the friction and thermal force sources are also described there.

4.4 Heat balance equation

Implementation of eq. 3.8 in SOLPS-ITER results in two slightly different equations for electron heat balance (4.19) and ion heat balance (4.22):

$$\begin{aligned} \frac{3}{2} \frac{\partial n_e T_e}{\partial t} + \frac{1}{\sqrt{g}} \frac{\partial}{\partial x} \left(\frac{\sqrt{g}}{h_x} \widetilde{q}_{ex} \right) + \frac{1}{\sqrt{g}} \frac{\partial}{\partial y} \left(\frac{\sqrt{g}}{h_y} \widetilde{q}_{ey} \right) + \frac{n_e T_e}{\sqrt{g}} \frac{\partial}{\partial x} \left(\frac{\sqrt{g}}{h_x} b_x v_{e\parallel} \right) = \\ = Q_e + Q_{\mathrm{I}}^e + n_e T_e B_z \frac{1}{h_x h_y} \left(\frac{\partial \phi}{\partial y} \frac{\partial}{\partial x} \left(\frac{1}{B^2} \right) - \frac{\partial \phi}{\partial x} \frac{\partial}{\partial y} \left(\frac{1}{B^2} \right) \right) \end{aligned} \tag{4.19}$$

Here the last term of the equation corresponds to the heat source from the plasma pressure multiplied by the divergence of the diamagnetic drift velocity. Terms in the left hand side correspond to the inertia, divergences of the heat fluxes and the convective term which consist of the pressure multiplied by the divergence of the parallel velocity.

The heat fluxes $\widetilde{q}_{ex}$ and $\widetilde{q}_{ey}$ are defined as follows:

$$\begin{aligned}\tilde{q}_{ex} = \frac{3}{2}\left(\sum_{a=0}^{n_s-1} z_a \left((b_x v_{a\|} + v_{ax}^{(E)} + \frac{5}{3}v_a^{(AN)})n_a - \frac{5}{3}D_a^n \frac{1}{h_x}\frac{\partial n_a}{\partial x}\right) - \frac{b_x j_\|}{e}\right) T_e \\ - 0.71 b_x \frac{j_\|}{e} T_e - \kappa_{e\|} b_x^2 \frac{1}{h_x}\frac{\partial T_e}{\partial x} + \frac{5}{2}\frac{B_z}{e}\left(\frac{1}{B^2} - \frac{1}{\langle B^2\rangle}\right)\frac{\partial n_e T_e^2}{h_y \partial y}\end{aligned} \tag{4.20}$$

$$\begin{aligned}\tilde{q}_{ey} = \sum_{a=0}^{n_s-1} z_a \left((b_x v_{a\|} + v_{ax}^{(E)} + \frac{5}{3}v_a^{(AN)})n_a - \frac{5}{3}D_a^n \frac{1}{h_x}\frac{\partial n_a}{\partial x}\right) T_e \\ - \kappa_{ey}\frac{1}{h_y}\frac{\partial T_e}{\partial y} - \frac{5}{2}\frac{B_z}{e}\left(\frac{1}{B^2} - \frac{1}{\langle B^2\rangle}\right)\frac{\partial n_e T_e^2}{h_x \partial x}\end{aligned} \tag{4.21}$$

The ion heat balance equation:

$$\begin{aligned}\frac{3}{2}\frac{\partial n_i T_i}{\partial t} + \frac{1}{\sqrt{g}}\frac{\partial}{\partial x}\left(\frac{\sqrt{g}}{h_x}\widetilde{q}_{ix}\right) + \frac{1}{\sqrt{g}}\frac{\partial}{\partial y}\left(\frac{\sqrt{g}}{h_y}\widetilde{q}_{iy}\right) + \sum_{a=0}^{ns-1}\frac{n_a T_i}{\sqrt{g}}\frac{\partial}{\partial x}\left(\frac{\sqrt{g}}{h_x}v_{a\|}b_x\right) \\ = -Q_e + Q_{F_{ab}} + T_i B_z \frac{1}{h_x h_y}\left(\frac{\partial \phi}{\partial y}\frac{\partial}{\partial x}\left(\frac{1}{B^2}\right) - \frac{\partial \phi}{\partial x}\frac{\partial}{\partial y}\left(\frac{1}{B^2}\right)\right)\sum_{\substack{a=0 \\ z_a \neq 0}}^{ns-1} n_a + \\ + \sum_{\substack{a=0 \\ z_a \neq 0}}^{ns-1}\left(\eta_{ax}\left(\frac{\partial v_{a\|}}{h_x \partial x}\right)^2 + \eta_a^{(AN)}\left(\frac{\partial v_{a\|}}{h_y \partial y}\right)^2\right) + Q_{\mathrm{I}} + Q_{\mathrm{R}} + Q_{\mathrm{CX}}\end{aligned} \tag{4.22}$$

The heat fluxes are determined as follows:

$$\begin{aligned}\tilde{q}_{ix} = \frac{3}{2}\sum_{a=0}^{n_s-1} z_a \left((b_x v_{a\|} - \frac{B_z}{B}\frac{1}{h_y}\frac{\partial \phi}{\partial y} + \frac{5}{3}v_a^{(AN)})n_a - \frac{5}{3}D_a^n \frac{1}{h_x}\frac{\partial n_a}{\partial x}\right) T_i \\ - \kappa_{i\|} b_x^2 \frac{1}{h_x}\frac{\partial T_i}{\partial x} + \frac{5}{2}\sum_{a=0}^{n_s-1}\frac{B_z}{e}\left(\frac{1}{B^2} - \frac{1}{\langle B^2\rangle}\right)\frac{\partial n_a T_i^2}{h_y \partial y}\end{aligned} \tag{4.23}$$

$$\begin{aligned}\tilde{q}_{iy} = \sum_{a=0}^{n_s-1} z_a \left((\frac{B_z}{B}\frac{1}{h_x}\frac{\partial \phi}{\partial x} + \frac{5}{3}v_a^{(AN)})n_a - \frac{5}{3}D_a^n \frac{1}{h_y}\frac{\partial n_a}{\partial y}\right) T_i \\ - \frac{j_{(AN)} + j_y^{(vis\|)} + j_y^{(in)}}{e} T_i - \kappa_{ey}\frac{1}{h_y}\frac{\partial T_i}{\partial y} - \frac{5}{2}\frac{B_z}{e}\left(\frac{1}{B^2} - \frac{1}{\langle B^2\rangle}\right)\frac{\partial n_e T_i^2}{h_x \partial x}\end{aligned} \tag{4.24}$$

The reason for only two heat balance equations being present in the code instead of n_s (for each plasma species, as it is done for particle and momentum balance) is that in SOLPS-ITER (as well as in all previous code versions) all ion species are assumed to share a common temperature.

The heat sources are described as follows: heat source due to the ionization Q_{I}, recombination Q_{R}, charge exchange Q_{CX}, ionization losses in the electron channel Q_{I}^{e}, due to the friction between ion species $Q_{\mathrm{F_{ab}}}$, due to the heat exchange between electrons and ions Q_{e}.

4.5 Charge conservation equation

To obtain the electric potential distribution in SOLPS-ITER code, the charge conservation equation is solved. This equation can be derived as a combination of the continuity equations for electrons and ions.

$$\frac{1}{\sqrt{g}}\frac{\partial}{\partial x}\left(\frac{\sqrt{g}}{h_x}j_x\right)+\frac{1}{\sqrt{g}}\frac{\partial}{\partial y}\left(\frac{\sqrt{g}}{h_y}j_y\right)=0 \tag{4.25}$$

Expressions for j_x and j_y are obtained from the radial and poloidal projections of the combination of the momentum balance equations for electrons and ions.

$$j_x=\widetilde{j}_x^{(dia)}+j_x^{(in)}+j_x^{(vis)}+\widetilde{j}_x^{(s)}+b_x j_{||} \tag{4.26}$$

$$j_y=j_{AN}+\widetilde{j}_y^{(dia)}+j_y^{(in)}+j_y^{(vis)}+\widetilde{j}_y^{(s)} \tag{4.27}$$

Different contributions in the currents are: $\widetilde{j}_{x,y}^{(dia)}$ - non-divergent part of the diamagnetic current, $j_{x,y}^{(in)}$- inertial current, $j_{x,y}^{(vis)}$ - viscous current, $\widetilde{j}_x^{(s)}$ - non-divergent part of the current caused by the ion-neutral friction, j_{AN} - anomalous current, $b_x j_{||}$ - poloidal projection of parallel current.

Expressions for the mentioned current contributions can be found in [5].

The parallel current is modified in present thesis due to the modification of the friction and thermal force terms. The previous implementation, used in the code, has the following form:

$$j_{||}=\sigma_{||}^{OLD}\left(\frac{1}{en_eh_x}\frac{\partial n_eT_e}{\partial x}-\frac{1}{h_x}\frac{\partial\phi}{\partial x}\right)-\alpha_{ex}^{OLD}\frac{1}{h_x}\frac{\partial T_e}{\partial x} \tag{4.28}$$

Here

- $\sigma_{||}^{OLD}=1.95b_xn_e\tau_e\dfrac{e^2}{m_e}$ - parallel conductivity (SI units);

- $\alpha_{ex}^{OLD} = 1.95\sqrt{\frac{5}{2}} b_x n_e \tau_e \frac{e}{m_e}$ - thermal conduction (SI units).

The new expression for the parallel current after the modification of the PMBE, friction and thermal force terms, is as follows:

$$j_{||} = \sigma_{||}^{NEW}\left(\frac{1}{en_e h_x}\frac{\partial n_e T_e}{\partial x} - \frac{1}{h_x}\frac{\partial \phi}{\partial x}\right) - \alpha_{ex}^{NEW}\frac{1}{h_x}\frac{\partial T_e}{\partial x} \tag{4.29}$$

Here the expressions for the parallel conductivity and thermal conduction are adopted according to the new form of the thermal and friction force terms:

- $\sigma_{||}^{NEW} = \frac{\sqrt{2}}{c_e^{(1)} z_{eff}} b_x n_e \tau_e \frac{e^2}{m_e}$ - parallel conductivity (SI units);
- $\alpha_{ex}^{NEW} = \frac{\sqrt{2} c_e^{(2)}}{c_e^{(1)}\left(z_{eff} + \frac{\sqrt{2}}{2}\right)} b_x n_e \tau_e \frac{e}{m_e}$ - thermal conduction (SI units).

Numerical coefficients $c_e^{(1)}$, $c_e^{(2)}$ are explained in the next chapter.

The electron collisional time τ_e in all the terms above is determined as follows:

$$\tau_e = \frac{3}{4\sqrt{2\pi} n_e}\frac{\sqrt{m_e} T_e^{3/2}}{\Lambda}\left(\frac{e^2}{4\pi\epsilon_0}\right)^2 \tag{4.30}$$

4.6 Boundary conditions

In the SOLPS-ITER equations, discussed above, the code finds the solution for $2n_s+3$ independent variables: n_s densities, n_s velocities, electron and ion temperature and the plasma electric potential. For all these quantities it is necessary to define the boundary condition on each boundary of the computational domain. These boundary conditions are one of the most important input parameters and their choice should be connected to the experimental input from the modeled experimental (planned) shot.

Below the set of boundary conditions is discussed. These are the boundary conditions used for the modeling cases, discussed in the chapters 5 to 7 of this thesis.

For the single-null divertor geometry one would require: two different types of radial boundaries in the code (core boundary and the tokamak wall boundary and only one type of poloidal boundaries - boundary to the divertor targets. These boundaries are represented on the computational mesh plot in fig. 4.2.

The boundary conditions for each of the boundary areas are specified below.

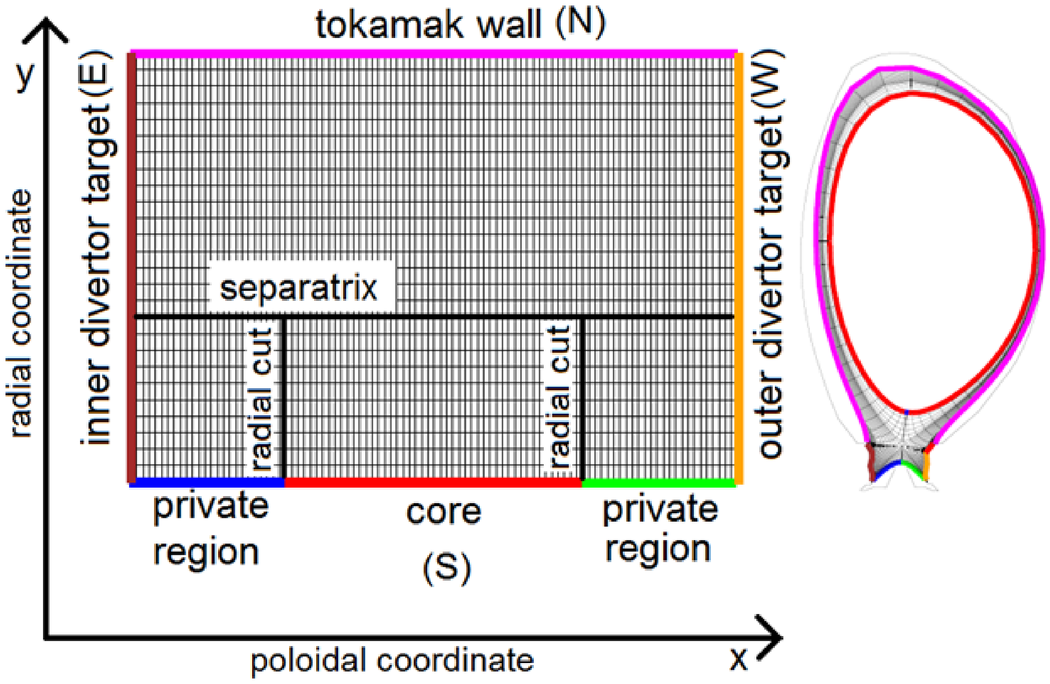

Figure 4.2: Computational and physical mesh with the color designation of the mesh boundaries. Adapted from [36]

4.6.1 The core boundary

- The boundary condition for the main ions and highest ionization state of impurities densities (feedback boundary condition): it prescribes the particle flux sum for all neutrals and ions belonging to a given isonuclear sequence and finds the average density of the highest ionization stage. A density perturbation for this density is taken from neighboring radial cell to keep the radial gradient of the density smooth and ensure the numerical stability of the simulations including drift terms.

  This boundary condition can be applied only to the highest ionization state of plasma species, since it emulates the following picture: all particles, belonging to the isonuclear sequence are flowing into the core and should return as the highest ionization state. This fixes the particle flux on the code side, when it is compared to the value, prescribed in the BC and then the density is changed in order to get these two flux values closer on the next step. (BCCON=27)

- The boundary condition for the other impurity ionization states densities (feedback boundary condition): it prescribes the total ion flux of this ionization state and finds the average density of this impurity ionization state, corresponding to this flux. A density perturbation is taken from neighbouring radial cell. This boundary condition is suitable for any species of multi-species plasma.

(BCCON=26)

- The boundary condition for the electron temperature (feedback boundary condition): it prescribes the total electron heat flux and finds the average temperature.(BCENE=16)

- The boundary condition for the the ion temperature (feedback boundary condition): it prescribes a total ion heat flux, constant poloidally averaged ion temperature and a poloidal variation in a simplified manner. (BCENI=27) - matching the main ions density boundary condition, can only be used in a combination with BCCON=27.

- The boundary condition for the poloidal velocity: zero radial gradient (BCMOM=2);

- The boundary condition for the electric potential: the radial current is set equal to the diamagnetic current at the core boundary (BCPOT=0):

$$j_y|_{core} = j_y^{dia}|_{core} = \left(B_z \sum_{\substack{a=0 \\ z_a \neq 0}}^{ns-1} n_a \left(z_a T_e + T_i \right) \frac{1}{h_x} \frac{\partial}{\partial x} \frac{1}{B^2} \right) |_{core} \tag{4.31}$$

4.6.2 The tokamak wall boundary

- Boundary condition for the ions (main and impurity) density: the radial particle flux through this boundary is determined as a fraction of the sound speed flux (BCCON=10)

$$- \widetilde{\Gamma}_{ay}|_{Wall} =$$
$$= \left(\xi_{n_a} c_s^a n_a - \left(\frac{1}{B^2} - \frac{1}{\langle B^2 \rangle} \right) \frac{B_z}{z_a e} \frac{1}{h_x} \frac{\partial n_a T_i}{\partial x} - max\left(0, n_a v_{ay}^{(E)}\right) \right) |_{Wall}$$

Here ξ_{n_a} is the leakage parameter; $c_s^a = \sqrt{\frac{z_a T_e + T_i}{m_a}}$ - the sound speed velocity for the ion species of sort "a".

The leakage parameter is prescribed in the input file b2.boundary.parameters through variables CONPAR(0, N,1) where N goes through 4 to 6 - numbers of regions, which belong to the tokamak wall (two private region boundaries and outer wall). This numerical parameter is usually set in the range 10^{-2} to 10^{-3}, depending on the steepness of the density gradient towards the wall.

- The boundary condition for the electron and ion temperature: prescribed decay length for the heat flux.

  For the electrons (BCENE=22):

$$k_{ey}\frac{\partial T_e}{h_y \partial y}|_{Wall} = -\lambda_{dec}^{T_e} c_s^e n_e T_e|_{Wall} \tag{4.32}$$

  For the ions(BCENI=22):

$$k_{iy}\frac{\partial T_i}{h_y \partial y}|_{Wall} = -\lambda_{dec}^{T_i} \sum_{\substack{a=0\\ z_a \neq 0}}^{ns-1} \left(c_s^a n_a\right) T_i|_{Wall} \tag{4.33}$$

  Here k_{ey} , k_{iy} - electron and ion heat conductivities in the radial direction; $c_s^e = \sqrt{T_e/m_e}$ - sound speed velocity for the electrons; $\lambda_{dec}^{T_e}$, $\lambda_{dec}^{T_i}$ - prescribed decay lengths for electron and ion heat fluxes. Decay lengths are prescribed in the input file b2.boundary.parameters through variables ENEPAR(1,1), ENIPAR(1,1), typical values are 10^{-4} for electrons and 10^{-2} for ions.

- The boundary condition for the poloidal velocity: zero radial gradient (BCMOM=2);

- The boundary condition for the electric potential: zero radial gradient (BCPOT=2).

4.6.3 The divertor targets boundary

- The boundary condition for the ions (main and impurity) density: the particle flux to the divertor targets is set to be equal to the sound speed flux (BCCON=14)

$$\widetilde{\Gamma}_{ax}|_W = \left(|b_x| c_s^{ion} n_a - \left(\frac{1}{B^2} - \frac{1}{\langle B^2 \rangle}\right) \frac{B_z}{z_a e} \frac{1}{h_y} \frac{\partial n_a T_i}{\partial y}\right)|_W \tag{4.34}$$

  (W is an inner divertor target boundary designation)

$$-\widetilde{\Gamma}_{ax}|_E = \left(|b_x| c_s^{ion} n_a + \left(\frac{1}{B^2} - \frac{1}{\langle B^2 \rangle}\right) \frac{B_z}{z_a e} \frac{1}{h_y} \frac{\partial n_a T_i}{\partial y}\right)|_E \tag{4.35}$$

(E is an outer divertor target boundary designation).

Here $c_s^{ion} = \sqrt{\sum\limits_{b=0}^{ns-1} p_b / \sum\limits_{b=0}^{ns-1} m_b n_b}$ - averaged ion sound speed velocity.

- The boundary condition for the electron and ion temperature: sheath boundary condition for the heat flux (BCENE,I=15):

$$\widetilde{q}_{ex}|_W = \left(-|b_x| \left((1+\gamma)T_e + (1-\gamma)e\phi \right) n_e \frac{1}{\sqrt{2\pi}} c_s^e exp\left(-\frac{e\phi}{T_e} \right) - q_{ex}^{P.Sch} \right) |_W \tag{4.36}$$

$$\widetilde{q}_{ex}|_E = \left(-|b_x| \left((1+\gamma)T_e + (1-\gamma)e\phi \right) n_e \frac{1}{\sqrt{2\pi}} c_s^e exp\left(-\frac{e\phi}{T_e} \right) - q_{ex}^{P.Sch} \right) |_E \tag{4.37}$$

Here γ is the coefficient of the secondary electron emission.

- The boundary condition for the poloidal velocity - speed sound boundary condition with the electric drift velocity modification (BCMOM=13);

$$v_W = -h_z \frac{\sqrt{g}}{h_x} \left(\frac{|b_x|}{b_x} v_{ax}^{E\times B} + b_x c_s \right) |_W \tag{4.38}$$

$$v_E = -h_z \frac{\sqrt{g}}{h_x} \left(\frac{|b_x|}{b_x} v_{ax}^{E\times B} - b_x c_s \right) |_E \tag{4.39}$$

Here c_s - averaged ion sound speed velocity (defined above).

- The boundary condition for the electric potential - sheath boundary condition on the current (BCPOT=11):

$$j_x|_W = e \left(\sum_{a=0}^{n_s-1} z_a(|b_x| c_s n_a) + (1-\gamma)|b_x| n_e \frac{1}{\sqrt{2\pi}} c_s^e exp(-\frac{e\phi}{T_e})|_W \right) \tag{4.40}$$

$$-j_x|_E = e \left(\sum_{a=0}^{n_s-1} z_a(|b_x| c_s n_a) + (1-\gamma)|b_x| n_e \frac{1}{\sqrt{2\pi}} c_s^e exp(-\frac{e\phi}{T_e})|_E \right) \tag{4.41}$$

Boundaries conditions should be selected in a problem-dependent manner. The set of boundary conditions used in the present thesis was recommended by the Saint-Petersburg team for drift modeling. The same set should not be just duplicated in every drift modeling. Every modeling task should be treated independently taking into account last features implemented in the SOLPS-ITER and the target physics problem.

Chapter 5

Impurity transport and the Parallel momentum balance equation (PMBE) modification

Impurity transport analysis is one of the major topics of the present thesis. In order to correctly estimate the retention to leakage ratio of the N and Ne impurities from the ITER and ASDEX Upgrade divertors in the SOLPS-ITER modeling results, it is important to understand impurity transport mechanisms in the code.

The mechanisms of the impurity transport in SOLPS are to a large extent determined by the impurity parallel velocity. This velocity in the code is an output of the Parallel Momentum Balance Equation (PMBE) for ions.

In order to improve the SOLPS-ITER code accuracy of the impurity transport modeling, an improvement of the PMBE for ions was made in the framework of the present thesis. Results of this improvement, discussed in this chapter, have been presented at the Plasma Edge Theory (PET) Workshop in 2017 and published in [21].

5.1 Old form of the PMBE. Limiting assumptions

Historically in the the code, a simplified version of the PMBE for ions was used. In the simplification, electric potential gradient term was excluded from the PMBE. This exclusion was made because older versions of the code did not solve the equation for the electric potential - the current balance equation.

In order to remove the potential gradient term from the PMBE for ions, it was combined with the PMBE for electrons. This allowed for replacing the potential gradient term by the electron pressure gradient term. After this procedure, the PMBE had the following form:

$$
\begin{aligned}
m_a\frac{\partial n_a v_{a\|}}{\partial t} + \frac{1}{h_z\sqrt{g}}\frac{\partial}{\partial x}\left(\frac{h_z\sqrt{g}}{h_y}\Gamma^m_{ax}\right) + \frac{1}{h_z\sqrt{g}}\frac{\partial}{\partial y}\left(\frac{h_z\sqrt{g}}{h_x}\Gamma^m_{ay}\right) + \frac{b_x}{h_x}\frac{\partial n_a T_i}{\partial x} + \frac{b_x}{h_x}\frac{z_a n_a \partial n_e T_e}{n_e \partial x} \\
= S^m_{a\|} + S^m_{\mathrm{CF}\|} + S^{m\mathrm{OLD}}_{\mathrm{Fr}_a} + S^{m\mathrm{OLD}}_{\mathrm{Therm}_a} + S^m_{\mathrm{I_a}} + S^m_{\mathrm{R}_a} + S^m_{\mathrm{CX}a}
\end{aligned}
\tag{5.1}
$$

Here:

- m_a, z_a, n_a, $v_{a\|}$ are correspondingly the mass, charge number, density and the parallel velocity of the ion species a;
- $\Gamma^m_{ax,y}$ are the x and y components of the momentum flux of these species;
- h_x, h_y, h_z and $\sqrt{g}$ are the metric coefficients;
- T_e and T_i are electron and ion temperatures;
- $S^m_{a\|}$- viscous momentum source;
- $S^m_{\mathrm{CF}\|}$- centrifugal momentum source;
- $S^m_{\mathrm{I_a}}$, $S^m_{\mathrm{R}_a}$, $S^m_{\mathrm{CX}a}$ are the momentum sources corresponding to ionization, recombination and charge exchange respectively;
- $S^{m\mathrm{OLD}}_{\mathrm{Fr}_a}$ and $S^{m\mathrm{OLD}}_{\mathrm{Therm}_a}$ are friction and thermal force terms in their old form.

The potential gradient term replacement, however, required specific assumptions:

- The impurity ions density in the plasma had to be negligible compared to the main ions density.
- Electron velocity was always assumed to be at least one order larger than ion velocity: in the moments of the derivation, where the sum of these two velocities was considered, the latter was not kept in the derivation.

In one of the next versions of the code [35], the current balance equation was solved and the potential gradient term was reintroduced in the PMBE. Reintroduction of the potential gradient was done through modifying the thermal force term, so the electric field term was included in the source term $S^{m\mathrm{OLD}}_{\mathrm{Therm}_a}$. The implemented form of the r. h. s. of the PMBE remained unchanged, which means it was still modified from the Braginskii form. Friction and thermal force terms used in the code after the return of the potential gradient term, but before their modification in the present thesis, are presented below.

$$S^{m\text{OLD}}_{\text{Fr}_a} = \sum_{\substack{b=0 \\ b\neq a, z_a\neq 0, z_b\neq 0}}^{n_s-1} \zeta_p^{-1}\sqrt{m_p}\sqrt{\frac{m_a m_b}{m_a+m_b}} z_a^2 z_b^2 n_a n_b \left(v_{b\|} - v_{a\|}\right) \tag{5.2}$$

where $\zeta_p = \frac{3}{4\sqrt{2\pi}}\frac{\sqrt{m_p}T_i^{3/2}}{\Lambda}\left(\frac{4\pi\epsilon_0}{e^2}\right)^2$, Λ - Coulomb logarithm.

$$S^{m\text{OLD}}_{\text{Therm}_a} = n_a n_e b_x e \zeta_p^{-1}\left(\frac{z_a}{n_e} - \frac{z_a^2}{n_{e^2}}\right)\left[\hat{E}_x - \frac{2.65}{e}\frac{\partial T_i}{h_x \partial x}\right] \tag{5.3}$$

Here $\hat{E}_x = \frac{1}{e n_e h_x}\frac{\partial n_e T_e}{h_x \partial x} - \frac{\partial \phi}{h_x \partial x}$ - modified electric field;

$n_{e^2} = \sum_{a=0}^{n_s-1} z_a^2 n_a$.

5.2 Braginskii form of the PMBE

In the framework of the present thesis, the original Braginskii [28] version of the PMBE was put in the SOLPS-ITER code. The equation implemented has the following form:

$$\begin{aligned} m_a\frac{\partial n_a v_{a\|}}{\partial t} &+ \frac{1}{h_z\sqrt{g}}\frac{\partial}{\partial x}\left(\frac{h_z\sqrt{g}}{h_y}\Gamma^m_{ax}\right) + \frac{1}{h_z\sqrt{g}}\frac{\partial}{\partial y}\left(\frac{h_z\sqrt{g}}{h_x}\Gamma^m_{ay}\right) + \\ &+\frac{b_x}{h_x}\frac{\partial n_a T_i}{\partial x} + e z_a n_a \frac{b_x}{h_x}\frac{\partial \phi}{\partial x} \\ &= S^m_{a\|} + S^m_{\text{CF}\|} + S^m_{\text{Fr}_a} + S^m_{\text{Therm}_a} + S^m_{\text{I}_a} + S^m_{\text{R}_a} + S^m_{\text{CX}a} \end{aligned} \tag{5.4}$$

This equation is very similar to eq. 5.1. There are 3 terms, which differ:

- $e z_a n_a \frac{b_x}{h_x}\frac{\partial \phi}{\partial x}$ - the electric force term in 5.4 - replaces $\frac{b_x}{h_x}\frac{z_a n_a \partial n_e T_e}{n_e \partial x}$ - electron pressure term from 5.1;
- $S^m_{\text{Fr}_a}$,$S^m_{\text{Therm}_a}$ - new form of friction and thermal force terms in 5.4 replace $S^{m\text{OLD}}_{\text{Fr}_a}$, $S^{m\text{OLD}}_{\text{Therm}_a}$ - old form of these terms from 5.1.

The original Braginskii version of the equation in [28] contained expressions for friction and thermal force only for the simple plasma, so for the multicomponent plasma modeling these terms had to be derived separately. Derivation of these terms was performed in the present thesis framework together with the implementation in the SOLPS-ITER code.

5.3 Thermal and friction force terms for the Braginskii form of the PMBE

In the first attempt to implement the Braginskii form of PMPE in the SOLPS code, [37], friction and thermal force terms for this form of equation were proposed in the simplest possible way. The derivation of these terms was based on [29].

The first attempt of this derivation was made with the trace impurity assumption. These terms were implemented in the code and modeling of the ASDEX Upgrade geometry scenarios was made with them. As it is shown in the next section, these terms were not accurate enough for the modeling of the impurity seeded discharges. These simplified terms will be referred here as “trace terms”.

In order to model impurity seeded case, first version of the derived friction and thermal force terms was modified and “corrected terms” for the friction and thermal forces were introduced in [21]. These terms allowed to lift the trace impurity assumption to a large extent and to achieve a more accurate treatment of impurities.

Below “corrected” terms for friction and thermal force are discussed. The difference between them and the “trace” terms are presented and discussed at the end of the section.

The friction force, acting on species “a”, can be split in two parts:

$$S^m_{\mathrm{Fr_a}} = S^m_{\mathrm{Fr,ea}} + S^m_{\mathrm{Fr,ia}}. \tag{5.5}$$

Here

- $S^m_{\mathrm{fr,ea}}$ is the electron-ion friction (has the same form for main ions and impurities);
- $S^m_{\mathrm{fr,ia}}$ is the ion-ion friction.

Explicit forms of ion-ion friction force, acting on the main ions $S^m_{\mathrm{Fr,i\_MAIN}}$, and on the impurity ions $S^m_{\mathrm{Fr,i\_IMP}}$ are written below.

$$S^m_{\mathrm{Fr_{ea}}} = -c_e^{(1)} m_e \zeta_e^{-1} n_e n_a z_a^2 (v_{\mathrm{a}\|} - v_{\mathrm{e}\|}) \tag{5.6}$$

$$S^m_{\mathrm{Fr_i\_MAIN}} = -\zeta_p^{-1} n_{\mathrm{MAIN}} z^2_{\mathrm{MAIN}} \sum_{\mathrm{IMP}} c^{(1)}_{\mathrm{IMP}} \sqrt{\mu_{\mathrm{MAIN\_IMP}} m_p}\; n_{\mathrm{IMP}} z^2_{\mathrm{IMP}} (v_{\mathrm{MAIN}\|} - v_{\mathrm{IMP}\|}) \tag{5.7}$$

$$\begin{aligned} S^m_{\mathrm{Fr_i\_IMP}} = {} & c^{(1)}_{\mathrm{IMP}} \zeta_p^{-1} \sqrt{\mu_{\mathrm{MAIN\_IMP}} m_p}\; n_{\mathrm{MAIN}} z^2_{\mathrm{MAIN}} n_{\mathrm{IMP}} z^2_{\mathrm{IMP}} (v_{\mathrm{MAIN}\|} - v_{\mathrm{IMP}\|}) \; - \\ & \sum_{\mathrm{IMP}*} \zeta_p^{-1} \sqrt{\mu_{\mathrm{IMP}*\_\mathrm{IMP}} m_p}\; n_{\mathrm{IMP}} z^2_{\mathrm{IMP}} n_{\mathrm{IMP}*} z^2_{\mathrm{IMP}*} (v_{\mathrm{IMP}\|} - v_{\mathrm{IMP}*\|}) \end{aligned} \tag{5.8}$$

where

- $\zeta_e = \dfrac{3}{4\sqrt{2\pi}} \dfrac{\sqrt{m_e} T_e^{\frac{3}{2}}}{\Lambda} (\dfrac{4\pi\epsilon_0}{e^2})^2$, $\zeta_p = \dfrac{3}{4\sqrt{2\pi}} \dfrac{\sqrt{m_p} T_i^{\frac{3}{2}}}{\Lambda} (\dfrac{4\pi\epsilon_0}{e^2})^2$ are electron and ion collision times normalized to corresponding densities,
- m_p - proton mass,
- $c_e^{(1)}$, $c^{(1)}_{\mathrm{IMP}}$- coefficients dependent on electron and ion densities,
- n_a, m_a, z_a, $v_{a\|}$ - density, mass, charge number and parallel velocity of ion species a,
- μ_{ab}- reduced mass of species a, b.

Note that subscripts MAIN and IMP respectively denote main ions and impurities. Different charge states of the same ion species are treated here as different species and correspond to different IMP indexes.

Thermal force acting on species "a", can also be split in the sum: $S^m_{\mathrm{Therm_a}} = S^m_{\mathrm{Therm,ea}} + S^m_{\mathrm{Therm,ia}}$.

Here

- $S^m_{\mathrm{Therm,ea}}$ is the electron thermal force, proportional to the parallel gradient of the electron temperature (has the same form for main ions and impurities);
- $S^m_{\mathrm{Therm,ia}}$ is the ion thermal force, proportional to the parallel gradient of the ion temperature.

It is again convenient to present the explicit form of the thermal force acting on the MAIN ions and on the impurity, IMP ions.

$$S^m_{\mathrm{Therm,ea}} = c_e^{(2)} c^{(\mathrm{Flim})}_{\mathrm{Therm_e}} \frac{n_a z_a^2}{z_{\mathrm{eff}} + \frac{\sqrt{2}}{2}} \nabla_\| T_e \tag{5.9}$$

$$S^m_{\text{Therm,MAIN}} = -c^{(2)}_{\text{IMP}} c^{(\text{Flim})}_{\text{Therm,i}} \frac{n_{\text{MAIN}} \sum\limits_{\text{IMP}} n_{\text{IMP}} z^2_{\text{IMP}} \sqrt{\frac{\mu_{\text{MAIN\_IMP}}}{m_{\text{MAIN}}}}}{\sum\limits_{\text{IMP}*} n_{\text{IMP}*} z^2_{\text{IMP}*} \sqrt{\frac{\mu_{\text{MAIN\_IMP}*}}{m_{\text{MAIN}}}} + \frac{\sqrt{2}}{2} n_{\text{MAIN}} z^2_{\text{MAIN}}} \triangledown_{\parallel} T_i \tag{5.10}$$

$$S^m_{\text{Therm,IMP}} = c^{(2)}_{\text{IMP}} c^{(\text{Flim})}_{\text{Therm}_\text{i}} \frac{n_{\text{MAIN}} n_{\text{IMP}} z^2_{\text{IMP}} \sqrt{\frac{\mu_{\text{MAIN\_IMP}}}{m_{\text{MAIN}}}}}{\sum\limits_{\text{IMP}*} n_{\text{IMP}*} z^2_{\text{IMP}*} \sqrt{\frac{\mu_{\text{MAIN\_IMP}*}}{m_{\text{MAIN}}}} + \frac{\sqrt{2}}{2} n_{\text{MAIN}} z^2_{\text{MAIN}}} \triangledown_{\parallel} T_i \tag{5.11}$$

Here

- $\triangledown_{\parallel} T_e$, $\triangledown_{\parallel} T_i$ - parallel projections of the electron and ion temperature gradients,
- $c^{(\text{Flim})}_{\text{Therm,e}}$, $c^{(\text{Flim})}_{\text{Therm,i}}$ - flux limiting coefficients.

Flux limiting coefficients are used to ensure that if outside the separatrix the temperature gradient exceeds a certain value, the thermal force terms would still be limited by a fraction of the maximized friction force value. This maximized friction force value is calculated assuming a Mach=1 velocity difference: for the electron-ion thermal force the velocity difference between electrons and ions in eq. (5.6) is replaced with $\sqrt{\frac{T_e}{m_e}}$; for the ion-ion thermal force the velocity difference between main ions ans impurity ions in eq. (5.7) (and between different impurity ion species in eq. (5.8)) is replaced with $\sqrt{\frac{T_i}{m_p}}$. Final limitation has the following form:

- electron-ion thermal force limit:

$$S^m_{\text{Therm,ea}} \leq 0.34 c^{(1)}_e \frac{m_e}{\zeta_e} n_e n_a z^2_a \sqrt{\frac{T_e}{m_e}} \tag{5.12}$$

- ion-ion thermal force limit for the thermal force, acting on the main ions:

$$S^m_{\text{Therm,MAIN}} \leq \ 0.532 \zeta_p^{-1} n_{\text{MAIN}} z^2_{\text{MAIN}} \sum_{\text{IMP}} c^{(1)}_{\text{IMP}} \sqrt{\mu_{\text{MAIN\_IMP}} m_p}\ n_{\text{IMP}} z^2_{\text{IMP}} \sqrt{\frac{T_i}{m_p}} \tag{5.13}$$

- ion-ion thermal force limit for the thermal force, acting on the impurity ions:

$$\begin{aligned} S^m_{\text{Therm,IMP}} \leq\ & 0.532 c^{(1)}_{\text{IMP}} \zeta_p^{-1} \sqrt{\mu_{\text{MAIN\_IMP}} m_p}\ n_{\text{MAIN}} z^2_{\text{MAIN}} n_{\text{IMP}} z^2_{\text{IMP}} \sqrt{\frac{T_i}{m_p}}\ + \\ & 0.532 \sum_{\text{IMP}*} \zeta_p^{-1} \sqrt{\mu_{\text{IMP}*\text{\_IMP}} m_p}\ n_{\text{IMP}} z^2_{\text{IMP}} n_{\text{IMP}*} z^2_{\text{IMP}*} \sqrt{\frac{T_i}{m_p}} \end{aligned} \tag{5.14}$$

Coefficients 0.34 for electrons and 0.532 for ions have been chosen to keep consistency with the corresponding terms in the previous version of the thermal force, implemented in the PMBE before it was rewritten in the Braginskii form (eq. (5.1)) in the D-only plasma limit.

The main effort in the derivation of the non-trace "corrected" friction and thermal force terms was the derivation of the coefficients, which are dependent on the impurity content. Details of this derivation are presented below in the section 5.5.

These coefficients are $c^{(1)}_e$, $c^{(2)}_e$ and $c^{(1)}_{\text{IMP}}$, $c^{(2)}_{\text{IMP}}$. They are defined as follows:

$$c^{(1)}_e = \frac{(1+0.24z_{\text{eff}})(1+0.93z_{\text{eff}})}{(1+2.56z_{\text{eff}})(1+0.29z_{\text{eff}})}; \tag{5.15}$$

$$c^{(2)}_e = 1.56\frac{(1+1.4z_{\text{eff}})(1+0.52z_{\text{eff}})}{(1+2.56z_{\text{eff}})(1+0.29z_{\text{eff}})} \tag{5.16}$$

$$c^{(1)}_{\text{IMP}} = \frac{(1+0.24z_{\text{eff\_imp}})(1+0.93z_{\text{eff\_imp}})}{(1+2.56z_{\text{eff\_imp}})(1+0.29z_{\text{eff\_imp}})}; \tag{5.17}$$

$$c^{(2)}_{\text{IMP}} = 1.56\frac{(1+1.4z_{\text{eff\_imp}})(1+0.52z_{\text{eff\_imp}})}{(1+2.56z_{\text{eff\_imp}})(1+0.29z_{\text{eff\_imp}})} \tag{5.18}$$

where, following the approach in [29], the parameter

$$z_{\text{eff\_imp}} = \sum_{\text{IMP}} (n_{\text{IMP}} z^2_{\text{IMP}})/(n_{\text{MAIN}} z^2_{\text{MAIN}}) \tag{5.19}$$

has been introduced in place of the more conventional z_{eff}.

The parameter $z_{\text{eff\_imp}}$ is more relevant for the description of ion-ion forces, and although it is very similar to $z_{\text{eff}} - 1$, it does not have the same value (see Fig. 5.1).

In fact, the difference between the "trace" terms presented in [37] and the "corrected" terms introduced here is that the assumption $z_{\text{eff\_imp}} = 0$ was made in the derivation of the former. This assumption puts factors $c^{(1)}_{\text{IMP}} = 1$, $c^{(2)}_{\text{IMP}} = 1.56$, but also influences the way the collision times are treated during the derivation. It

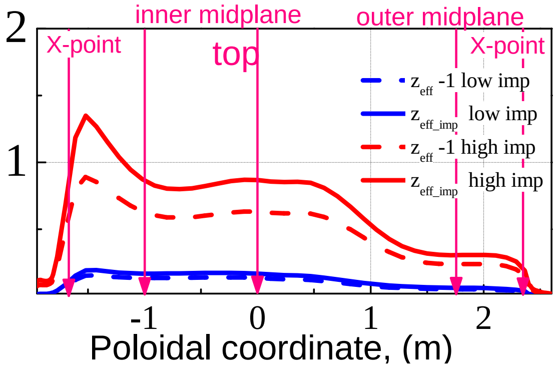

Figure 5.1: Poloidal profiles of $z_{\text{eff}} - 1$ and $z_{\text{eff\_imp}}$ for the case with low (blue) and high (red) impurity seeding rates.

results in an oversimplified version of the thermal force which does not contain any dependence on the main ion density, eq. 5.20.

$$S^{m,Trace}_{\text{Therm,MAIN}} = -1.56 c^{(\text{Flim})}_{\text{Therm}_{\text{MAIN\_imp}}} \sum_{\text{IMP}} n_{\text{IMP}} z^2_{\text{IMP}} \sqrt{\frac{\mu_{\text{MAIN\_IMP}}}{m_{\text{MAIN}}}} \nabla_{\parallel} T_i \tag{5.20}$$

The corrections to the ion-ion interaction forces introduced in the present work can finally be defined in the following way:

$$\text{FR}_{\text{correction}} = \text{c}^{(1)}_{\text{IMP}} \tag{5.21}$$

$$\text{TF}_{\text{correction}} = \frac{\text{c}^{(2)}_{\text{IMP}}}{1.56} \frac{\text{c}^{(\text{Flim})}_{\text{Therm}_{\text{MAIN\_imp}}} \text{n}_{\text{IMP}} \text{z}^2_{\text{IMP}} \sqrt{\frac{\mu_{\text{MAIN\_IMP}}}{\text{m}_{\text{MAIN}}}}}{\sum_{\text{IMP}*} \text{n}_{\text{IMP}*} \text{z}^2_{\text{IMP}*} \sqrt{\frac{\mu_{\text{MAIN\_IMP}*}}{\text{m}_{\text{MAIN}}}} + \frac{\sqrt{2}}{2} \text{n}_{\text{MAIN}} \text{z}^2_{\text{MAIN}}} \tag{5.22}$$

for the friction and thermal forces respectively.

The corrections introduced in the momentum balance terms have also consistently been included in the SOLPS-ITER current balance and heat balance equations. Modifications were made in the expressions of electron heat fluxes, parallel current, classical electrical conductivity and thermo-electric coefficients.

Although the corrected terms give a more accurate treatment of the friction and thermal force terms, certain assumptions are still required for their derivation.

- The model is valid under the assumption of mass separation between the different species: the impurity species must be heavier than the main ion (at least factor of 3 difference). It is thus not possible at that stage to model D-T plasmas or to treat Deuterium-Helium mixtures. The mass separation allows the use of the form of the coefficients $c^{(1)}_{\mathrm{IMP}}$, $c^{(2)}_{\mathrm{IMP}}$ presented in equations 5.17, 5.18 for interactions between main ions and impurity ions. For interaction between different species of impurity ions no explicit formulation for such coefficients is implemented. A linear system of equations given in [29] must then be solved to get friction and thermal forces.

- In the present formulation, friction between them occurs with unity numerical coefficient and the thermal force is not taken into account. These two terms are second order with respect to the impurity density, since they are proportional to n^2_{IMP} in comparison to terms proportional to $n_{\mathrm{MAIN}} \cdot n_{\mathrm{IMP}}$ (for processes between main ions and impurities).

5.4 Effect of the thermal and friction force corrections in the Braginskii form of the PMBE

The influence which the modification of the friction and thermal force from "trace" to the "corrected" forms has on the modeling results, has been studied on the ASDEX Upgrade geometry case with nitrogen impurity seeding. Significant impurity redistribution was obtained with the "corrected" form of the terms.

The mesh for the test cases considered, fig. 5.2, was based on the real magnetic geometry from the ASDEX Upgrade tokamak shot 28093. This shot was selected because it was already successfully modeled with the SOLPS code [38]. Even though the test cases were based on the realistic magnetic geometry (AUG reconstruction), they are not related to any specific experimental discharge.

Input parameters of the test case are as follows:

- Input heating power through the core side of the computational domain: 5 MW; 1/3 of this power is introduces through the ion channel, 2/3 though the electrons;
- H-mode pedestal included through the anomalous radial transport coefficients input, fig. 5.3;
- Drifts and currents are fully activated;
- The deuterium fueling is set to 2x10^{22} atoms/s through a gas puff of deuterium molecules at the centre of the divertor dome baffle;
- Impurity (nitrogen) seeding is set at the same location with two different rates: 8x10^{18} atoms/s (trace impurity case) and 5x10^{19} atoms/s.
  Trace impurity rate is defined here as the rate below which SOL radiation does not exceed 2% of the total input power.

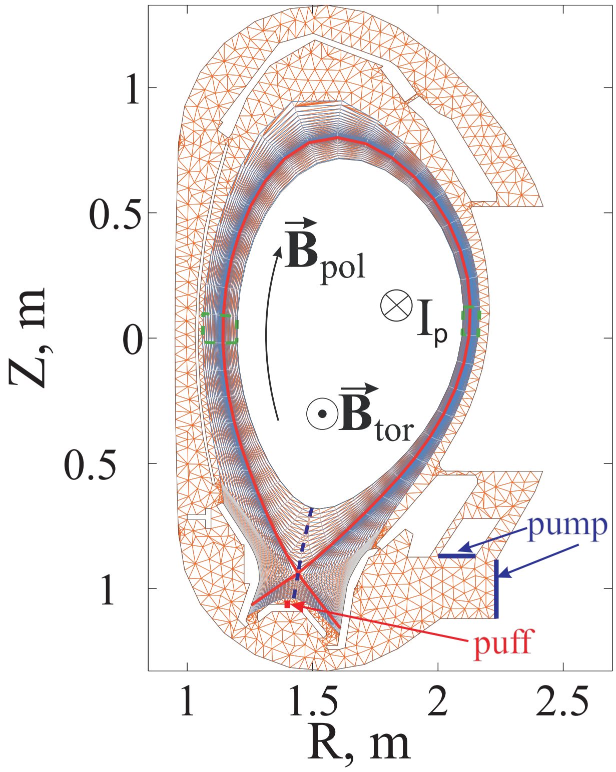

Figure 5.2: Computational domain.

For the second case at 5x10^{19} atoms/s, this SOL radiation is already 15% of total input power in the simulation. Although 5x10^{19} atoms/s is not a particularly high seeding rate in comparison with experiments ($\sim 10^{21}$ atoms/s are typical in ASDEX Upgrade [38]), it will be referred as "high" for convenience.

The effect of the correction terms depends strongly on the impurity content. Impurity redistribution is quite significant for the higher seeding rate (z_{eff} $\sim$1.5) and becomes less pronounced for the trace impurity case ($z_{\text{eff}} < 1.5$)

The main difference for the high seeding rate case is that the corrected form of the friction and thermal force terms impedes impurity accumulation in the SOL above the outer midplane, which would lead to impurity accumulation in the core, Fig. 5.4 (a) at the location of the maximum of the temperature gradient Fig. 5.4 (b).

For the high impurity seeding case calculated with the "trace" version of friction and thermal force terms, the impurity density peaks strongly at the outer midplane. This peak, which tends to grow as the simulation proceeds, leading eventually to radiative collapse of the case, occurs due to inaccuracy in the thermal force description.

Due to the peaking of the thermal force at the location of the temperature gradient maximum (e.g. above the outer midplane in the cases considered), the impurity

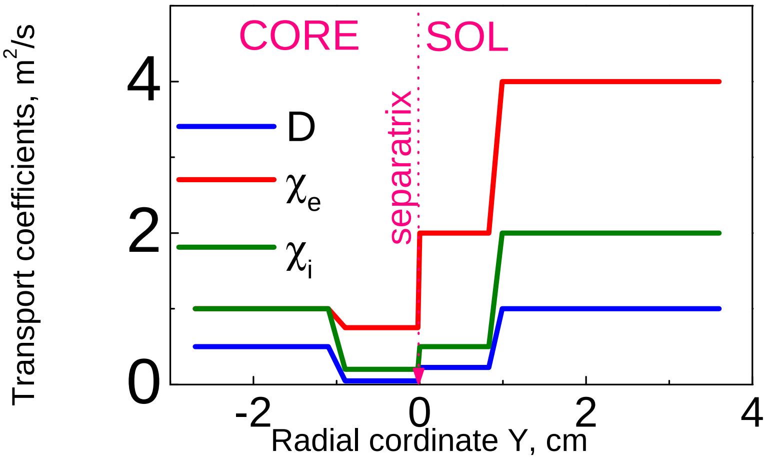

Figure 5.3: Anomalous transport coefficients in equatorial midplane.

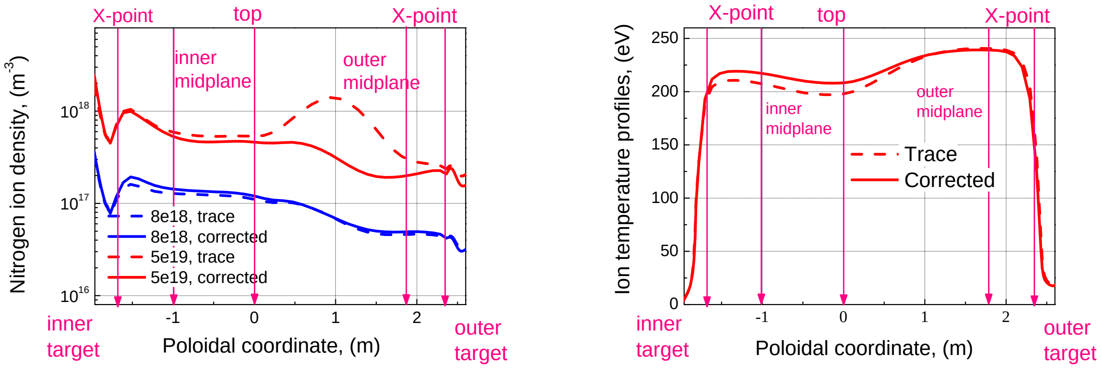

a)   b)

Figure 5.4: Poloidal profiles of the friction and thermal force terms for the case with the small (a) and large (b) impurity seeding rates with trace (dash lines) and corrected (solid lines) forms of momentum balance terms treatment (for the same surface)

content starts to increase while the main ion density decreases. The “trace” form of thermal force (eq. 5.20), is proportional only to the impurity density and to the temperature gradient. So it also increases and drags more impurities to this area, even if the main ion content in the region decreases below that of the impurities. At the final stage of the numerical instability, the main ion density at the maximum of T_i tends to zero.

With the corrected form of the thermal force eq. 5.10, this instability does not occur, due to the fact that the linear dependence of the thermal force on the impurity density cancels out, and the thermal force decreases with decreasing main ion density. As a result, the new treatment provides a smoother distribution of the impurity along the field line, with reduced accumulation at the maximum of T_i even though the SOL T_i profile does not change.

To understand the mechanism of poloidal redistribution of the impurity ion density, an analysis of the parallel momentum balance was performed.

In [19], it was shown that the impurity parallel momentum balance is determined to a large extent by the balance of thermal and friction forces. Contribution of the electric force and ion pressure gradient force in the PMBE is at least one order of magnitude lower (apart from the very cold detached areas of the SOL, which are not present in the cases considered). To understand the difference in the impurity distributions in the cases considered it was sufficient to compare friction and thermal force terms, Fig. 5.5 (a), (b).

In the new “corrected” formulation, the friction and thermal forces are reduced in the SOL at the position of their peak values. Redistribution of the impurity ions occurs despite the fact that, in both the “trace” and “corrected” formulation, thermal and friction force terms are almost balanced.

The reason why the redistribution still occurs is the fact that the correction factors, introduced in the new formulation, do not have exactly the same values for the friction and thermal force terms. This leads to the change of impurity parallel velocities. This correction is the main driver in the impurity ion redistribution process.

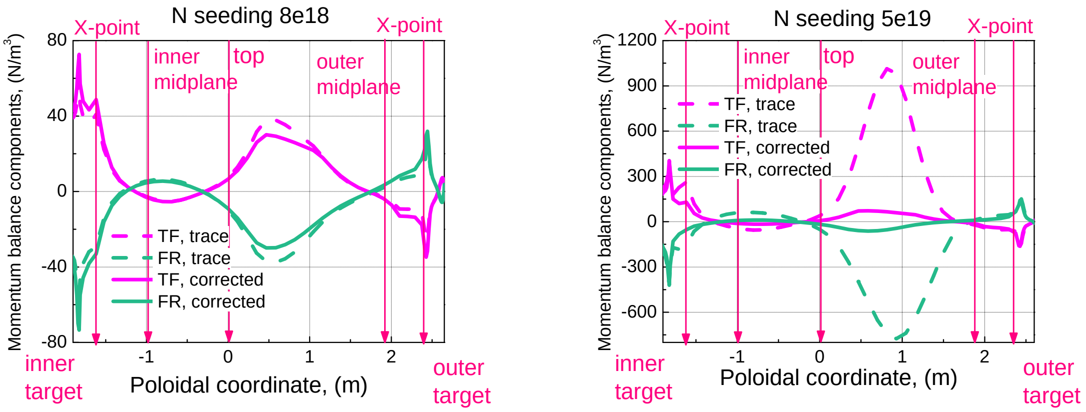

a) b)

Figure 5.5: Poloidal profiles of the friction and thermal force terms for the case with the small (a) and large (b) impurity seeding rates with trace (dash lines) and corrected (solid lines) forms of momentum balance terms treatment (for the same surface)

5.5 Derivation of the corrected thermal and friction force terms for the Braginskii form of the PMBE

The derivation of the corrected form for the friction and thermal force terms discussed above is based on the multicomponent plasma description introduced by V. Zhdanov [29]. The central equation for the derivation, presented here, is (5.23) below, which was taken from paragraph 8.4 of [29]. This equation describes the sum of the friction and thermal forces, acting on ion species a.

$$\mathrm{S^m_{Therm_a}} + \mathrm{S^m_{Fr_a}} = -\mathrm{n_a}\left(\sum_{\mathrm{b}}\left[\mathrm{c^{(1)}_{ab}}\mu_{\mathrm{ab}}\tau^{-1}_{\mathrm{ab}}\left(\mathrm{v_{a||}} - \mathrm{v_{b||}}\right) - \frac{\mathrm{c^{(2)}_{ab}}\tau^{-1}_{\mathrm{ab}}}{\widetilde{\tau}^{-1}_{\mathrm{b}}}\frac{\mu_{\mathrm{ab}}}{\mathrm{m_a}}\nabla_{||}\mathrm{T_b}\right] + \mathrm{c^{(5)}_a}\nabla_{||}\mathrm{T_a}\right) \tag{5.23}$$

Here

- m_a and n_a are the mass and density of species a;
- $\widetilde{\tau}_a^{-1} = \sum_c \frac{\mu_{ac}}{m_a}\tau_{ac}^{-1}$ is the averaged collision frequency;
- $\mu_{ab} = \frac{m_a m_b}{m_a + m_b}$ is the reduced mass for species pair a, b;
- τ_{ab}^{-1} is the collision frequency between species a and b (the exact form of the collision frequency is discussed below);
- $v_{a||}$, $v_{b||}$ are the projections of the velocities for species a and b on the direction parallel to the magnetic field;
- $\nabla_{||}T_a$ is the projection of the gradient of the temperature of species a on the parallel to the magnetic field direction;
- $c^{(1)}_{ab}$, $c^{(2)}_{ab}$ and $c^{(5)}_a$ are coefficient as defined below.

Coefficients $c_{ab}^{(1)}$ are assumed to be symmetrical against the permutation of a, b indices.

The first term in the sum in (5.23) corresponds to the friction force interaction between plasma species, second term in the sum and the last term correspond to the thermal forces. In [29] the different ion species are assumed to have different temperatures, so there are separate terms with parallel temperature gradients in (5.23): the term which comes with other species temperature gradients appears in the sum and has normalization of the collision frequency in front of it (τ_{ab}^{-1} / $\widetilde{\tau}_b^{-1}$, comes from the kinetic derivation of (5.23)); the term from the considered species itself comes later (last term of equation).

The complicated part in the implementation of Eq. (5.23) is the calculation of the numerical coefficients $c_{ab}^{(1)}$, $c_{ab}^{(2)}$ and $c_a^{(5)}$. Generally, the calculation of these coefficients should be performed for each simulated plasma composition (set of the types of ions chosen for modeling, e.g. pure deuterium plasma, D-T mixture, D plasma with N impurity, etc.). Depending on the masses of the ions present in the composition, the coefficients can be calculated by integration of the system of kinetic equations using generalized Laguerre polynomials.

As shown in [29], for relatively light plasma particles k with low mass in comparison to that of other species in the same plasma, the calculation of these coefficients can be simplified and they can be defined as:

$$c_{ka}^{(1)} = c_{ak}^{(1)} = \frac{(1 + 0.24\widetilde{z}_k)(1 + 0.93\widetilde{z}_k)}{(1 + 2.56\widetilde{z}_k)(1 + 0.29\widetilde{z}_k)}; \tag{5.24}$$

$$c_{ak}^{(2)} = 1.56\frac{(1 + 1.4\widetilde{z}_k)(1 + 0.52\widetilde{z}_k)}{(1 + 2.56\widetilde{z}_k)(1 + 0.29\widetilde{z}_k)} \tag{5.25}$$

$$c_{ka}^{(2)} = 0 \tag{5.26}$$

Here $\widetilde{z}_k = \sum\limits_{a:m_a>>m_k} \frac{n_a z_a^2}{n_k z_k^2}$ is an averaged charge of the heavy particles with respect to the light ones.

In case then of electrons are taken as light particles and compared to all ion species:

$$\widetilde{z}_e = \sum_{a:m_a>>m_e} \frac{n_a z_a^2}{n_e} = z_{\text{eff}} \tag{5.27}$$

In the implementation discussed here, the same mass separation was performed between main ions and impurity ions. Impurity ions were considered to be heavy particles in this case:

$$z_{\mathrm{IMP}} = \sum_{\mathrm{IMP}} \frac{n_{\mathrm{IMP}} z_{\mathrm{IMP}}^2}{n_a z_a^2} = z_{\mathrm{eff\_imp}} \tag{5.28}$$

This procedure of simplification of the coefficient calculation will be referred below as "mass separation procedure". It was used for the coefficients $c_e^{(1)}$, $c_e^{(2)}$, $c_{\mathrm{imp}}^{(1)}$ and $c_{\mathrm{imp}}^{(2)}$ defined in (5.15)-(5.18).

The remaining definition of the coefficients $c_{aa}^{(2)}$ and $c_a^{(5)}$ is performed in two steps. First, it is important to show that eq. (5.23) for each plasma species contains these coefficients only in specific combinations $\left(c_a^{(5)} - \frac{1}{2}c_{aa}^{(2)}\right)$. Then there will be no need to define coefficients $c_{kk}^{(2)}$, $c_k^{(5)}$, separately – only the combination will need to be defined.

To show the fact, that only the combination $\left(c_a^{(5)} - \frac{1}{2}c_{aa}^{(2)}\right)$ has to be defined, one has to rewrite the equation (5.23) in the following way (separating the term with $\nabla_{||}T_a$):

$$\begin{aligned} \mathrm{S}^{\mathrm{m}}_{\mathrm{Therm_a}} + \mathrm{S}^{\mathrm{m}}_{\mathrm{Fr_a}} = -\mathrm{n_a} \sum_{\mathrm{b \neq a}} & \left[\mathrm{c}^{(1)}_{\mathrm{ab}} \mu_{\mathrm{ab}} \tau_{\mathrm{ab}}^{-1} \left(\mathrm{v_{a||}} - \mathrm{v_{b||}} \right) - \frac{\mathrm{c}^{(2)}_{\mathrm{ab}} \tau_{\mathrm{ab}}^{-1}}{\widetilde{\tau}_{\mathrm{b}}^{-1}} \frac{\mu_{\mathrm{ab}}}{\mathrm{m_a}} \nabla_{||} \mathrm{T_b} \right] \\ & + n_a \left[c_a^{(5)} - \frac{c_{aa}^{(2)} \tau_{aa}^{-1}}{\widetilde{\tau}_a^{-1}} \frac{\mu_{aa}}{m_a} \right] \nabla_{||} T_a \end{aligned} \tag{5.29}$$

By the definition of the reduced mass $\frac{\mu_{aa}}{m_a} = \frac{1}{2}$, so the last term in (5.29) would be $n_a \left[c_a^{(5)} - \frac{c_{aa}^{(2)} \tau_{aa}^{-1}}{\widetilde{\tau_a^{-1}}} \frac{1}{2} \right] \nabla_{||} T_a$.

Now, according to Newton's third law, friction and thermal forces between all types of plasma particles should compensate each other. This means that after summing up the separate momentum balance equations for all plasma species all the terms should cancel out:

$$
\begin{aligned}
&\sum_{\mathrm{a}}\left(\mathrm{S}^{\mathrm{m}}_{\mathrm{Therma_a}}+\mathrm{S}^{\mathrm{m}}_{\mathrm{Fr a_a}}\right)= \\
&-\sum_{a} n_a \sum_{b\neq a}\left[c^{(1)}_{ab}\mu_{ab}\tau^{-1}_{ab}\left(v_{a||}-v_{b||}\right)-\frac{c^{(2)}_{ab}\tau^{-1}_{ab}}{\tilde{\tau}^{-1}_{b}}\frac{\mu_{ab}}{m_a}\nabla_{||}T_b\right] \\
&+\sum_{a} n_a\left[c^{(5)}_{a}-\frac{c^{(2)}_{aa}\tau^{-1}_{aa}}{\tilde{\tau}^{-1}_{a}}\frac{\mu_{aa}}{m_a}\right]\nabla_{||}T_a
\end{aligned}
\tag{5.30}
$$

The first term in the first sum on the RHS of eq (5.30) gives the condition $c^{(1)}_{ab}=c^{(1)}_{ba}$ (to eliminate velocity terms), which was mentioned above (symmetry of the $c^{(1)}_{ab}$ coefficient). The remaining terms correspond to the thermal force:

$$
0=-\sum_{a} n_a\left(\sum_{b\neq a}\left[-\frac{c^{(2)}_{ab}\tau^{-1}_{ab}}{\tilde{\tau}^{-1}_{b}}\frac{\mu_{ab}}{m_a}\nabla_{||}T_b\right]+\left[c^{(5)}_{a}-\frac{c^{(2)}_{aa}\tau^{-1}_{aa}}{\tilde{\tau}^{-1}_{a}}\frac{\mu_{aa}}{m_a}\right]\nabla_{||}T_a\right)
\tag{5.31}
$$

It is convenient to define the coefficients in (5.31) by looking separately at each type of plasma particle (every plasma species). Here the procedure will be demonstrated for coefficients corresponding to electron temperature gradients. In this case $\frac{\mu_{eb}}{m_e}\approx\frac{m_e}{m_e}=1$ for b denoting any sort of ion species.

$$
\begin{aligned}
&c^{(2)}_{e\_\mathrm{MAIN}}\frac{\tau^{-1}_{e\_\mathrm{MAIN}}}{\tilde{\tau}^{-1}_{e}}\nabla_{||}T_{\mathrm{MAIN}}+c^{(2)}_{e\_\mathrm{IMP}}\frac{\tau^{-1}_{e\_\mathrm{IMP}}}{\tilde{\tau}^{-1}_{e}}\nabla_{||}T_{\mathrm{IMP}}+ \\
&c^{(2)}_{\mathrm{MAIN}\_e}\frac{\tau^{-1}_{\mathrm{MAIN}\_e}}{\tilde{\tau}^{-1}_{e}}\nabla_{||}T_{\mathrm{e}}+c^{(2)}_{\mathrm{IMP}\_e}\frac{\tau^{-1}_{\mathrm{IMP}\_e}}{\tilde{\tau}^{-1}_{e}}\nabla_{||}T_{\mathrm{e}}+ \\
&\left(c^{(5)}_{e}-c^{(2)}_{ee}\frac{1}{2}\frac{\tau^{-1}_{ee}}{\tilde{\tau}^{-1}_{e}}\right)\nabla_{||}T_e=0
\end{aligned}
\tag{5.32}
$$

Substituting the values of $c^{(2)}_{e\_\mathrm{MAIN}}$, $c^{(2)}_{e\_\mathrm{IMP}}$, $c^{(2)}_{\mathrm{MAIN}\_e}$, $c^{(2)}_{\mathrm{IMP}\_e}$ from (5.25), (5.26) we obtain:

$$
\left(c^{(5)}_{e}-c^{(2)}_{ee}\frac{1}{2}\frac{\tau^{-1}_{ee}}{\tilde{\tau}^{-1}_{e}}\right)=c^{(2)}_{e}\left(\frac{\tau^{-1}_{e\_\mathrm{MAIN}}}{\tilde{\tau}^{-1}_{e}}+\frac{\tau^{-1}_{e\_\mathrm{IMP}}}{\tilde{\tau}^{-1}_{e}}\right)
\tag{5.33}
$$

Equation (5.33) yields the combination $\left(c^{(5)}_{e}-\frac{1}{2}c^{(2)}_{ee}\right)$ mentioned above. With these, the implementation of Eq (5.23) for electrons in the mass separation assumption is complete.

The same procedure is followed for the main ion temperature gradient (assuming the mass separation between light main ions and relatively heavy impurity), resulting in:

$$\left(c^{(5)}_{\mathrm{MAIN}} - c^{(2)}_{\mathrm{MAIN\_MAIN}}\frac{1}{2}\frac{\tau^{-1}_{\mathrm{MAIN\_MAIN}}}{\widetilde{\tau}^{-1}_{\mathrm{MAIN}}}\right) = -\sum_{\mathrm{IMP}} c^{(2)}_{\mathrm{IMP}}\frac{\tau^{-1}_{\mathrm{MAIN\_IMP}}}{\widetilde{\tau}^{-1}_{\mathrm{MAIN}}}\frac{\mu_{\mathrm{MAIN\_IMP}}}{m_{\mathrm{IMP}}} \tag{5.34}$$

Impurity temperature gradient terms are neglected in this implementation of the parallel momentum balance equation, as mentioned above. The derivation of the coefficient in front of such terms can not be done by the same procedure and would require future effort. These terms are second-order with respect to impurity density and at the moment they are not included in the code.

The problem with the calculation of impurity temperature gradient terms is that for these coefficients the mass separation procedure described above can not be used since the masses of the impurities are usually of the same order. Therefore these coefficients can be calculated only by integration of the system of kinetic equations using generalized Laguerre polynomials with the masses and densities of the ions present in each plasma composition. The analytical benchmark of the implemented model would be significantly complicated. Since the impurity densities are at least one order of magnitude lower than that of the main ions, the terms of the second-order with respect to the impurity density can be neglected in order to keep the analytical form of the code equations.

5.5.1 Collision times

The definition of the collision times is essential while dealing with processes of particle interactions in plasma. Two different conventions for this quantity exist in tokamak plasma physics (Braginskii [28] and Balescu [39]), making it extremely important to define it carefully to avoid misinterpretation of the final expressions. In the present thesis the formulation from [29] is followed, which matches the approach of Braginskii [28]. Before presenting the collision times, it is convenient to define the following quantities:

$$\zeta_p = \frac{3}{4\sqrt{2\pi}}\frac{\sqrt{m_p}T_i^{3/2}}{\Lambda}\left(\frac{4\pi\epsilon_0}{e^2}\right)^2 \tag{5.35}$$

$$\zeta_e = \frac{3}{4\sqrt{2\pi}}\frac{\sqrt{m_e}T_e^{3/2}}{\Lambda}\left(\frac{4\pi\epsilon_0}{e^2}\right)^2 \tag{5.36}$$

Here m_p, m_e are respectively the proton and electron mass, Λ is the Coulomb logarithm, ϵ_0 is the vacuum permittivity. Here ζ_e, ζ_p are normalized collision times for electrons and protons respectively. Use of (5.35), (5.36) simplifies the symmetry-checking procedure of the final equations. The collision times can then be written as follows:

$$\tau_{ab}^{-1} = \frac{4\sqrt{2\pi}\sqrt{2}n_b}{3}\frac{z_a^2 z_b^2 \Lambda}{T_i^{3/2}\mu_{ab}^{1/2}}\left(\frac{e^2}{4\pi\epsilon_0}\right)^2 = \sqrt{2}\zeta_p^{-1} n_b z_a^2 z_b^2 \frac{\sqrt{m_p}}{\sqrt{\mu_{ab}}} \tag{5.37}$$

$$\tau_{eb}^{-1} = \frac{4\sqrt{2\pi}n_b}{3}\frac{z_b^2 \Lambda}{T_e^{3/2}m_e^{1/2}}\left(\frac{e^2}{4\pi\epsilon_0}\right)^2 = \zeta_e^{-1} n_b z_b^2 \tag{5.38}$$

$$\tau_{be}^{-1} = \zeta_e^{-1} n_e z_b^2 \tag{5.39}$$

$$\tau_{ee}^{-1} = \frac{4\sqrt{2\pi}\sqrt{2}n_e}{3}\frac{\Lambda}{T_e^{3/2}m_e^{1/2}}\left(\frac{e^2}{4\pi\epsilon_0}\right)^2 = \sqrt{2}\zeta_e^{-1} n_e \tag{5.40}$$

In order to use equation 5.23 it is also necessary to define the average collision frequency for species a, $\widetilde{\tau}_a^{-1} = \sum_b \frac{\mu_{ab}}{m_a}\tau_{ab}^{-1}$.

For the electrons:

$$\begin{gathered}
\widetilde{\tau}_e^{-1} = \sum_a \frac{\mu_{ae}}{m_e}\tau_{ea}^{-1} = \sum_{\text{IMP}} \tau_{e\_\text{IMP}}^{-1} + \tau_{e\_\text{MAIN}}^{-1} + \frac{1}{2}\tau_{ee}^{-1} = \\
\zeta_e^{-1}\sum_{\text{IMP}} n_{\text{IMP}} z_{\text{IMP}}^2 + n_{\text{MAIN}} z_{\text{MAIN}}^2 \zeta_e^{-1} + \frac{\sqrt{2}}{2}\zeta_e^{-1} n_e = n_e \zeta_e^{-1}\left(z_{eff} + \frac{\sqrt{2}}{2}\right)
\end{gathered} \tag{5.41}$$

For the main ions:

$$\begin{gathered}
\widetilde{\tau}_{\text{MAIN}}^{-1} = \sum_a \frac{\mu_{\text{MAIN}\_a}}{m_{\text{MAIN}}}\tau_{\text{MAIN}\_a}^{-1} = \\
\sum_{\text{IMP}} \frac{\mu_{\text{MAIN\_IMP}}}{m_{\text{MAIN}}}\tau_{\text{MAIN\_IMP}}^{-1} + \frac{1}{2}\tau_{\text{MAIN\_MAIN}}^{-1} + \frac{m_e}{m_{\text{MAIN}}}\tau_{\text{MAIN}\_e}^{-1} \approx \\
\sum_{\text{IMP}} \sqrt{2}\frac{\mu_{\text{MAIN\_IMP}}}{m_{\text{MAIN}}}\frac{\sqrt{m_p}}{\sqrt{\mu_{\text{MAIN\_IMP}}}} n_{\text{IMP}} z_{\text{IMP}}^2 z_{\text{MAIN}}^2 \zeta_p^{-1} + \\
\frac{1}{2}\frac{\sqrt{m_p}}{\frac{m_{\text{MAIN}}}{2}}\sqrt{2} n_{\text{MAIN}} z_{\text{MAIN}}^4 \zeta_p^{-1} = \\
\sqrt{2}\zeta_p^{-1} z_{\text{MAIN}}^2 \frac{\sqrt{m_p}}{m_{\text{MAIN}}}\sum_{\text{IMP}} \sqrt{\mu_{\text{MAIN\_IMP}}} n_{\text{IMP}} z_{\text{IMP}}^2 + \sqrt{\frac{m_p}{m_{\text{MAIN}}}} n_{\text{MAIN}} z_{\text{MAIN}}^4 \zeta_p^{-1}
\end{gathered} \tag{5.42}$$

In the derivation of the (5.42) the term proportional to the ratio of the electron to the ion mass is neglected to simplify the result.

5.5.2 Final form of the friction and thermal force terms

Now that the collision frequencies have been defined, eq. (5.23) can be rewritten in its complete form. In this subsection, it will be done for the electron, main ions and impurity ions. The friction and thermal force terms for the main ions and impurity ions were already presented above, but to show the complete derivation process, they will be repeated here.

The friction and thermal forces, acting on the electrons, is given by:

$$\begin{aligned} S^m_{\mathrm{Fr}_e} + S^m_{\mathrm{Therm}_e} = & -c_e^{(1)} m_e \zeta_e^{-1} z^2_{\mathrm{MAIN}} n_{\mathrm{MAIN}} n_e \left(v_{e||} - v_{\mathrm{MAIN}||}\right) \\ & -c_e^{(1)} m_e \zeta_e^{-1} \sum_{\mathrm{IMP}} z^2_{\mathrm{IMP}} n_{\mathrm{IMP}} n_e \left(v_{e||} - v_{\mathrm{IMP}||}\right) \\ & -c_e^{(2)} \left(\tau^{-1}_{\mathrm{MAIN\_}e} \widetilde{\tau}_e + \sum_{\mathrm{IMP}} \tau^{-1}_{\mathrm{IMP\_}e} \widetilde{\tau}_e \right) n_e \nabla_{||} T_e \end{aligned} \tag{5.43}$$

Using (5.39) and (5.41) one can obtain $\tau^{-1}_{\mathrm{MAIN\_}e} \widetilde{\tau}_e = \dfrac{z^2_{\mathrm{MAIN}}}{z_{\mathrm{eff}} + \sqrt{2}/2}$; $\tau^{-1}_{\mathrm{IMP\_}e} \widetilde{\tau}_e = \dfrac{z^2_{\mathrm{IMP}}}{z_{\mathrm{eff}} + \sqrt{2}/2}$, thus (5.43) can be finalized in the following way:

$$\begin{aligned} S^m_{\mathrm{Fr}_e} + S^m_{\mathrm{Therm}_e} = & -c_e^{(1)} m_e \zeta_e^{-1} z^2_{\mathrm{MAIN}} n_{\mathrm{MAIN}} n_e \left(v_{e||} - v_{\mathrm{MAIN}||}\right) \\ & -c_e^{(1)} m_e \zeta_e^{-1} \sum_{\mathrm{IMP}} z^2_{\mathrm{IMP}} n_{\mathrm{IMP}} n_e \left(v_{e||} - v_{\mathrm{IMP}||}\right) \\ & -c_e^{(2)} \left(\frac{z^2_{\mathrm{MAIN}}}{z_{\mathrm{eff}} + \sqrt{2}/2} + \sum_{\mathrm{IMP}} \frac{z^2_{\mathrm{IMP}}}{z_{\mathrm{eff}} + \sqrt{2}/2} \right) n_e \nabla_{||} T_e \end{aligned} \tag{5.44}$$

This form, in the pure deuterium plasma limit, matches the Braginskii [28] friction and thermal force expression:

$$S^m_{\mathrm{Fr}_e} + S^m_{\mathrm{Therm}_e} = -0.51 \frac{m_e n_e}{\tau_e} \left(v_{e||} - v_{\mathrm{i}||}\right) - 0.71 n_e \nabla_{||} T_e \tag{5.45}$$

To write eq. (5.23) for ion-ion interactions (5.37) and (5.42) are used:

$$\tau^{-1}_{\mathrm{IMP\_MAIN}} \widetilde{\tau}_{\mathrm{MAIN}} \frac{\mu_{\mathrm{IMP\_MAIN}}}{m_{\mathrm{MAIN}}} = \frac{n_{\mathrm{MAIN}} z^2_{\mathrm{IMP}} \sqrt{\frac{\mu_{\mathrm{IMP\_MAIN}}}{m_{\mathrm{MAIN}}}}}{\sum_{\mathrm{IMP}} \sqrt{\frac{\mu_{\mathrm{IMP\_MAIN}}}{m_{\mathrm{MAIN}}}} n_{\mathrm{IMP}} z^2_{\mathrm{IMP}} + \frac{\sqrt{2}}{2} n_{\mathrm{MAIN}} z^2_{\mathrm{MAIN}}} \tag{5.46}$$

The final forms of eq. (5.23) for ions - sum of all the friction and thermal forces acting on the main ions and each impurity ion species - become correspondingly:

$$\begin{aligned} S^m_{\mathrm{Fr}_{\mathrm{MAIN}}} + S^m_{\mathrm{Therm}_{\mathrm{MAIN}}} = & -c_e^{(1)} m_e \zeta_e^{-1} z^2_{\mathrm{MAIN}} n_{\mathrm{MAIN}} n_e \left(v_{\mathrm{MAIN}||} - v_{e||}\right) \\ -\sum_{\mathrm{IMP}} c^{(1)}_{\mathrm{IMP}} \sqrt{2} \sqrt{\mu_{\mathrm{MAIN\_IMP}}} & \zeta_e^{-1} z^2_{\mathrm{IMP}} n_{\mathrm{IMP}} z^2_{\mathrm{MAIN}} n_{\mathrm{MAIN}} \left(v_{\mathrm{MAIN}||} - v_{\mathrm{IMP}||}\right) \\ & -c_e^{(2)} \frac{z^2_{\mathrm{MAIN}} n_{\mathrm{MAIN}}}{z_{\mathrm{eff}} + \sqrt{2}/2} \nabla_{||} T_e \\ & - \frac{\sum_{\mathrm{IMP}} c^{(2)}_{\mathrm{IMP}} n_{\mathrm{MAIN}} z^2_{\mathrm{IMP}} \sqrt{\frac{\mu_{\mathrm{IMP\_MAIN}}}{m_{\mathrm{MAIN}}}}}{\sum_{\mathrm{IMP}} \sqrt{\frac{\mu_{\mathrm{IMP\_MAIN}}}{m_{\mathrm{MAIN}}}} n_{\mathrm{IMP}} z^2_{\mathrm{IMP}} + \frac{\sqrt{2}}{2} n_{\mathrm{MAIN}} z^2_{\mathrm{MAIN}}} \nabla_{||} T_{\mathrm{MAIN}} \end{aligned} \tag{5.47}$$

$$
\begin{gathered}
S^m_{\text{Fr}_{\text{IMP}}} + S^m_{\text{Therm}_{\text{IMP}}} = -c_e^{(1)} m_e \zeta_e^{-1} z_{\text{IMP}}^2 n_{\text{IMP}} n_e \left(v_{\text{IMP}||} - v_{e||}\right) \\
-c_{\text{IMP}}^{(1)} \sqrt{2}\sqrt{\mu_{\text{MAIN\_IMP}}}\zeta_e^{-1} z_{\text{IMP}}^2 n_{\text{IMP}} z_{\text{MAIN}}^2 n_{\text{MAIN}} \left(v_{\text{IMP}||} - v_{\text{MAIN}||}\right) \\
- \sum_{\text{IMP}*} \sqrt{2}\sqrt{\mu_{\text{IMP}*\text{\_IMP}}}\zeta_e^{-1} z_{\text{IMP}}^2 n_{\text{IMP}} z_{\text{IMP}*}^2 n_{\text{IMP}*} \left(v_{\text{IMP}||} - v_{\text{IMP}*||}\right) \\
-c_e^{(2)} \frac{z_{\text{IMP}}^2 n_{\text{IMP}}}{z_{\text{eff}} + \sqrt{2}/2} \nabla_{||} T_e \\
+\frac{c_{\text{IMP}}^{(2)} n_{\text{MAIN}} z_{\text{IMP}}^2 \sqrt{\frac{\mu_{\text{IMP\_MAIN}}}{m_{\text{MAIN}}}}}{\sum_{\text{IMP}} \sqrt{\frac{\mu_{\text{IMP\_MAIN}}}{m_{\text{MAIN}}}} n_{\text{IMP}} z_{\text{IMP}}^2 + \frac{\sqrt{2}}{2} n_{\text{MAIN}} z_{\text{MAIN}}^2} \nabla_{||} T_{\text{MAIN}}
\end{gathered}
\tag{5.48}
$$

5.5.3 The parallel current modification

Since the expressions for electron-ion friction and thermal force are now modified, the expression for parallel current should be modified accordingly. To do so, one should consider the electron parallel momentum balance equation in its stationary form:

$$
0 = -\nabla_{||} p_e + e n_e \nabla_{||}\phi + c_e^{(1)} m_e \zeta_e^{-1} n_e \sum_a n_a z_a^2 \left(v_{a||} - v_{e||}\right) - \frac{c_e(2) z_{\text{eff}}}{z_{\text{eff}} + \sqrt{2}/2} \nabla_{||} T_e \tag{5.49}
$$

Here index a in the sum goes through all the ions species (main and impurity ions).

From (5.49) it is possible to construct a parallel current expression. By definition, the parallel current is $j_{||} = e\sum_a n_a v_{a||} z_a - e n_e v_{e||}$. To extract such an expression from (5.49) one would need to add and subtract a term $c_e^{(1)} m_e \zeta_e \sum_a n_a z_a^2 \sum_b n_b z_b v_{b||}$.

$$
\begin{gathered}
0 = -\nabla_{||} p_e + e n_e \nabla_{||}\phi + \\
c_e^{(1)} m_e \zeta_e^{-1} e^{-1} n_e e \sum_a n_a z_a^2 v_{a||} \\
+c_e^{(1)} m_e \zeta_e^{-1} e^{-1} \sum_a \left(e n_a z_a^2 \sum_b n_b z_b v_{b||} - n_a z_a^2 n_e e v_{e||} - e n_a z_a^2 \sum_b n_b z_b v_{b||} \right) \\
-\frac{c_e(2) z_{\text{eff}}}{z_{\text{eff}} + \sqrt{2}/2} \nabla_{||} T_e
\end{gathered}
\tag{5.50}
$$

Now it is possible to construct $j_{||}$ in brackets, by combining $\sum_a \left(e n_a z_a^2 \sum_b n_b z_b v_{b||} - n_a z_a^2 n_e e v_{e||} \right)$ and taking the $j_{||} = e\sum_b n_b v_{b||} z_b - e n_e v_{e||}$ out from the sum over the index a. The equation (5.50) can then be written in the following form:

$$\begin{gathered}0 = -\nabla_{||} p_e + e n_e \nabla_{||}\phi + \\ c_e^{(1)} m_e \zeta_e^{-1} e^{-1} e \sum_a n_a z_a^2 \left(n_e v_{a||} - \sum_b n_b z_b v_{b||} \right) \\ + c_e^{(1)} m_e \zeta_e^{-1} e^{-1} j_{||} \sum_a e n_a z_a^2 - \frac{c_e^{(2)} z_{\text{eff}}}{z_{\text{eff}} + \sqrt{2}/2} \nabla_{||} T_e\end{gathered} \tag{5.51}$$

Using the fact that $\sum_a n_a z_a^2 = n_e z_{\text{eff}}$, the $j_{||}$ can be extracted from the (5.51) in the following form:

$$\begin{gathered}j_{||} = \frac{e^2 \zeta_e}{c_e^{(1)} m_e z_{\text{eff}}} \left(\frac{1}{e n_e} \nabla_{||} p_e - \nabla_{||}\phi \right) - \\ \frac{e}{z_{\text{eff}}} \sum_a n_a z_a^2 \left(n_e v_{a||} - \sum_b n_b z_b v_{b||} \right) + \frac{c_e^{(2)} e \zeta_e}{c_e^{(1)} m_e \left(z_{\text{eff}} + \sqrt{2}/2 \right)} \nabla_{||} T_e\end{gathered} \tag{5.52}$$

The sum $\sum\limits_a n_a z_a^2 \left(n_e v_{a||} - \sum\limits_b n_b z_b v_{b||} \right)$ can be significantly simplified. Using the $n_e = \sum\limits_a n_a z_a^2 / z_{\text{eff}}$ it can be rewritten as:

$$\frac{1}{z_{\text{eff}}} \sum n_a z_a^2 v_{a||} \sum_b n_b z_b^2 - \sum n_a z_a^2 \sum n_b z_b v_{b||} \tag{5.53}$$

Since both indices a and b in the sums have the same intervals in which they change, in the second sum one can rename the indices ($a \leftrightarrow b$), after that the terms in 5.53 can be regrouped the following way:

$$\sum_b n_b z_b^2 \left(\frac{1}{z_{\text{eff}}} \sum n_a z_a^2 v_{a||} - \sum n_a z_a v_{a||} \right) \tag{5.54}$$

Now using again $n_e = \sum\limits_a n_a z_a^2 / z_{\text{eff}}$ in (5.54) and substituting it in the expression for the parallel current (5.52) one can obtain the final expression for the parallel current:

$$\begin{gathered}j_{||} = \frac{e^2 \zeta_e}{c_e^{(1) m_e z_{\text{eff}}}} \left(\frac{1}{e n_e} \nabla_{||} p_e - \nabla_{||}\phi \right) - \\ \frac{e}{z_{\text{eff}}} \sum_a n_a v_{a||} \left(z_a^2 - z_a z_{\text{eff}} \right) + \frac{c_e^{(2)} e \zeta_e}{c_e^{(1) m_e} \left(z_{\text{eff}} + \sqrt{2}/2 \right)} \nabla_{||} T_e\end{gathered} \tag{5.55}$$

This form of the parallel current is included in the SOLPS-ITER code now, and was already mentioned in the chapter about the code equations (eq. 4.29).

5.6 Comparison of the old form of the PMBE with the Braginskii form with corrected terms

In the previous section, it is shown that the Braginskii form of the PMBE with the corrections to the friction and thermal forces included, provides a stable solution for the impurity seeded plasmas.

In the present section, results obtained with the Braginskii version of the PMBE, 5.4, with the "corrected" thermal and friction force terms are compared with the results, obtained with the "old" version of the PMBE, 5.1.

Comparison was made on the modeling results obtained with the same input parameters, which were used for the testing of the "trace" and "corrected" forms of the thermal and friction force. The only difference was that the impurity seeding rates for the "high" impurity seeding: the seeding rate of the N for this case was set to 8x10^{19} atoms/s instead of 5x10^{19} atoms/s. For the "trace" case a seeding level if 8x10^{18} atoms/s was retained.

The new treatment (Fig. 5.6) results in a different distribution of the impurity ions along the SOL field line and thus a different z_{eff} value. The most pronounced effect is a higher impurity density in the upper SOL region. For the 8x10^{19} atoms/s case, this modified impurity redistribution increases z_{eff} at the separatrix by roughly 10%, with a corresponding decrease (by 20%) of the impurity ion content in the outer divertor.

Observed change in the impurity ion poloidal distribution is especially important for consistent modeling of exhaust scenarios with impurity seeding and for correct definition of the operational constraints for these scenarios. Profiles achieved with this new, more accurate formulation (Braginskii form of the PMBE), are more realistic. Modeling results achieved with the old formulation are likely to make too positive estimation of impurity compression in the divertor. This might lead to underestimating the core impurity content for a given divertor radiation level.

Further tests of the differences between the modeling results, obtained with the old and the new forms of the equation were not made. The Braginskii form of the parallel momentum balance equation with the new ("corrected") form of friction and thermal force terms was set as default in the SOLPS-ITER code as more theoretically sound.

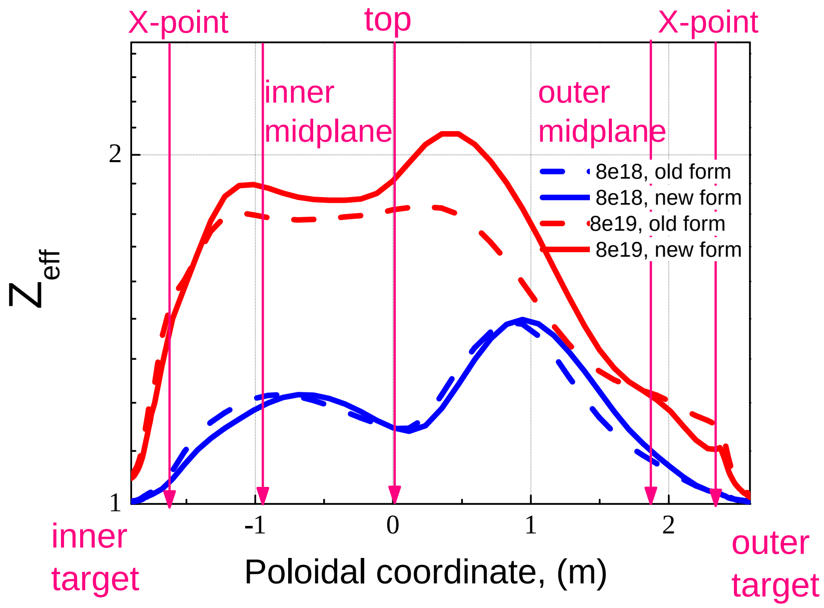

Figure 5.6: Poloidal distribution of z_{eff} for the case with the low (blue) and high (red) impurity seeding rates obtained with old (dashed) and new (solid) forms of the PMBE in SOLPS-ITER for the SOL flux surface 1 mm outside the separatrix (mapped to the outer midplane).

Chapter 6

Discussion of the ITER and ASDEX Upgrade modeling results

In this chapter the modeling results obtained with the 3.0.6 version of the SOLPS-ITER code (which includes the modification of the parallel momentum balance equation, described in the previous chapter) will be presented. These results served the basis for the impurity transport investigation and the study of the difference between nitrogen and neon behaviour described in the next chapter.

6.1 Modeling setup

The numerical meshes used in the modeling are presented in Fig. 6.1.

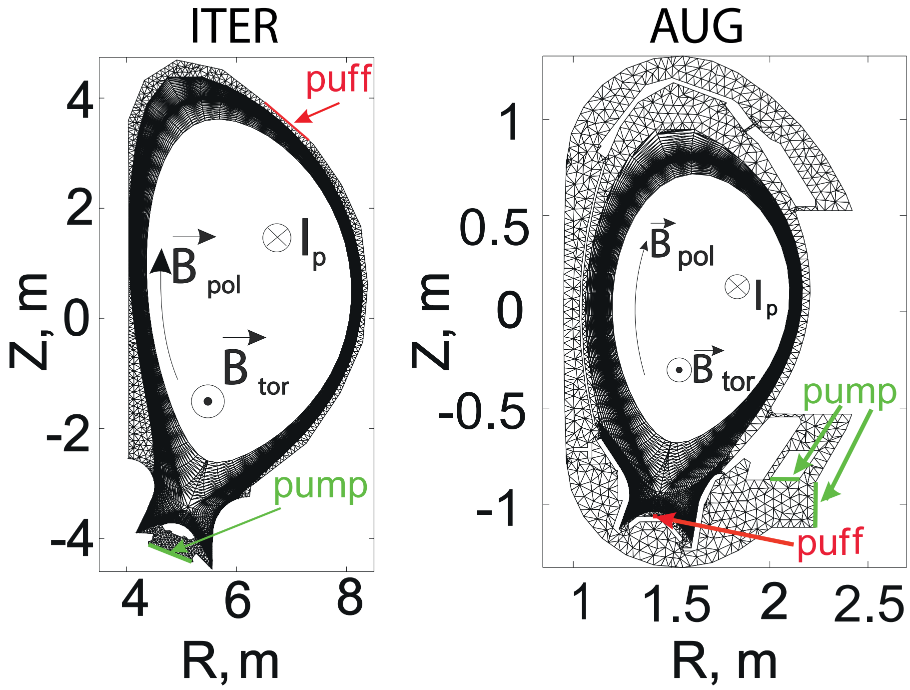

Figure 6.1: Computational mesh for ITER cases (left) and AUG cases (right).

For the ITER cases, the standard (ITER internal mesh number F57) mesh with 36 radial cells and 90 poloidal cells was used [8], [15]. This mesh corresponds to a $q_{95} = 3$ burning plasma (H-mode) magnetic equilibrium ($I_p = 15$ MA, $B_T = 5.3$ T).

For AUG, the grid has 36 radial cells and 96 poloidal cells. It was created based on the real machine geometry and the equilibrium corresponding to the Type I ELMing H-mode shot #28903, with $I_p = 800$ kA, $B_T = 2.5$ T and with a higher $q_{95} = 5.5$ [38] than for the ITER cases. One has to note that in this thesis no serious attempt is made here to match experimental results – the study is comparative and aims to compare the use of different seeding gases on a large (reactor scale) and a medium-sized tokamak.

One should note very different scales of the ITER and AUG meshes shown in Fig. 6.2. This size difference results in the different parameter distributions, which are discussed in the next chapter.

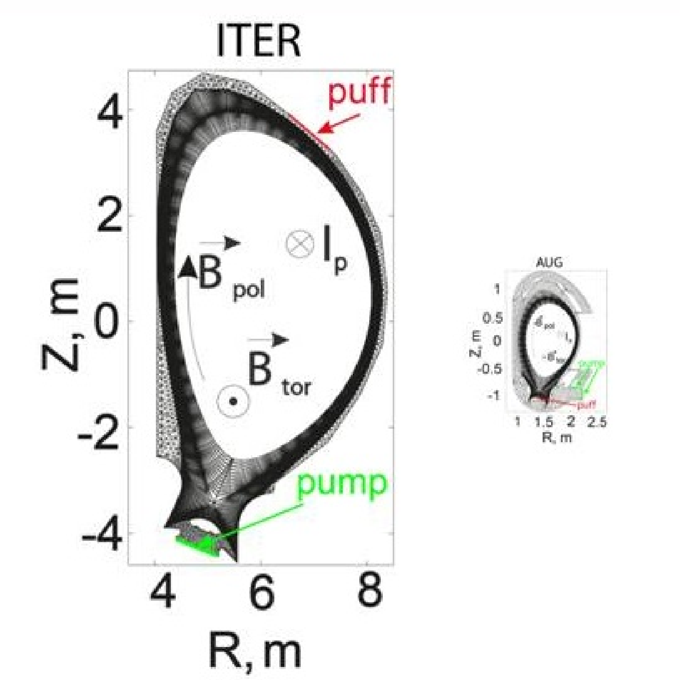

Figure 6.2: Computational mesh for ITER cases (left) and AUG cases (right) with the same scale unit.

The ITER simulations had beryllium as wall material and tungsten (W) on the divertor contour, with W assumed on all wall and divertor surfaces for AUG. In both cases (AUG and ITER) W, sputtering is not activated and the W impurity is not followed in the calculations.

Radial transport in the SOLPS-ITER code is not modeled self-consistently, in common with all boundary plasma simulation packages of this type. Instead radial transport is specified as an input parameter (through the b2.transport.inputfile). Anomalous radial transport coefficients for particles ($D_\perp$) and heat ($\chi_\perp$) used here for the modeling results analyzed in the next chapter are shown in Fig. 6.3. They are set differently for AUG and ITER cases, but remain the same within each geometry for the two seeding species considered (N and Ne). To reproduce the H-mode transport barrier, $D_\perp$ and heat $\chi_\perp$ are reduced in the core region in both cases, though the structure for the AUG cases, based on [4], is more complex and is intended to provide similar outboard midplane pedestal and SOL profiles to those seen in experiment for pulse #28903, inward pinch at the separatrix is used for AUG for this reason. For ITER transport was kept as simple as possible.

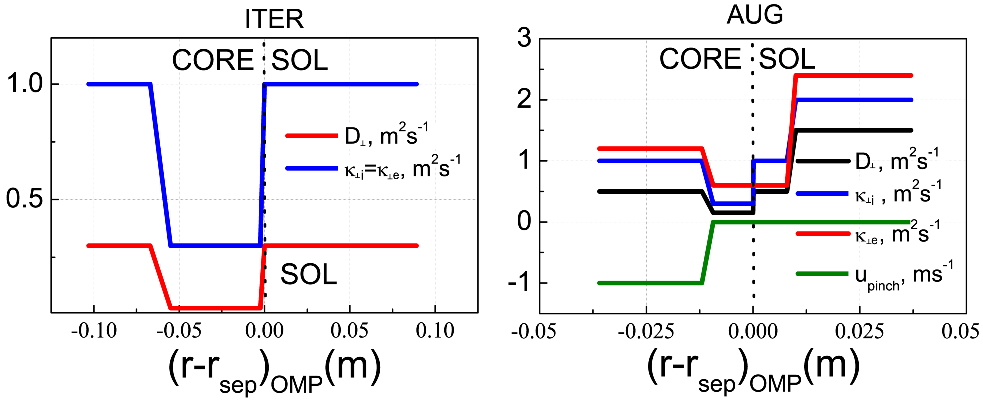

Figure 6.3: Radial transport coefficients for ITER (left) and AUG geometry (right) simulations.

Key input parameters for the simulations are compared in Table 6.1.

	ITER		AUG	
q_{95}	3		5.5	
$s_{\|\|}$(m)	190		130	
P_{in}(MW)	100		5	
D_{puff}(10^{23}e/s)	1.95		0.2	
Seeded gas	N	Ne	N	Ne
Seeding rate (10^{21}e/s)	21	2	0.35	0.2
Neutral pressure (Pa)	11.4	11.6	9.7	9.3

Table 6.1: Safety factor q_{95}, connection length of the chosen modeling scenarios (from the modeling results), power input, D gas puff and impurity seeding rates used in the modeling - compared for all considered modeling cases.

In particular, injected powers of 100 MW and 5 MW are specified at the inner core boundary of the numerical grid for ITER and AUG respectively. For ITER the power is distributed equally between ions and electrons. For AUG, approximately 2/3rd of the input power is placed in the electrons and 1/3rd in the ions; the different profiles for the radial heat conductivity ($\chi_{\perp e}$) and ($\chi_{\perp e}$) are selected to match measurements even though no attempt is made here to compare the code predictions in the divertor with experiment.

Due to the difference in scale size, the absolute quantities of fuel (deuterium) and seeded impurities are larger for ITER than AUG. As shown later (see Table 7.1), the rates were also chosen to try and approximately match the total radiated power fractions between the devices for each given seed impurity.

Boundary conditions at the targets were set to sheath boundary conditions for all variables (both electron and ion temperatures, ion densities and poloidal velocities, electric potential). Decay length boundary conditions were specified at the main wall and the PFR (private flux region) boundaries. More details on the boundary conditions description are given in the Chapter 4.

Impurity seeding (puff location) is done from the cell on top of the mesh for ITER (like in the previous ITER modeling [15]) and from under the dome for AUG geometry cases (real experimental location) (see Figure 6.1). Such a difference in the seeding position worsens the comparability of the discussed cases. However the results, discussed below, show better impurity compression in the divertor for ITER, despite unfavorable seeding position, so one can still consider these results to be relevant.

Impurity seeding rates of N and Ne for both simulated geometries are presented in Table 6.1. The choice of the seeding rate values for each geometry (AUG, ITER) was made such that the distributions of the temperature and density were similar between N and Ne seeded cases (AUG N similar to the AUG Ne, ITER N similar to the ITER Ne). The feature which is seen in the modeling is better compression of neutral N (in a cold regions, not affecting the radiation) for ITER than for AUG. To achieve similar fractions of radiated power an increased ratio ($\sim$ factor 6) of impurity to fuel throughput is required for ITER in comparison to AUG. The precise reasons for this different behavior of neutral N at the two different size scales are not currently understood.

Between the devices (ITER and AUG) the choice of the impurity seeding rates was made such that it provided similar ratios of radiated to input power ($\mathrm{P_{rad\_tot}/P_{in}}$). For nitrogen seeded cases the following values were achieved: 60% of the total input power radiated for ITER seeded case and 48% for AUG case. Neon seeded cases had the following values: 67% for ITER and 52% for AUG.

The neutral particles in the modeling were treated by the Eirene code [40], which is coupled to the SOLPS plasma solver in the SOLPS-ITER code. Eirene describes the neutral particles transport in a kinetic way. The Fokker-Planck equation for the neutrals is solved with a Monte-Carlo approach. The interactions of the neutrals with the plasma are given in the Table (6.2) (this idea is taken from [2]). The detailed description of all reactions can be found in [40] and [2].

Reaction	Eirene Label	Type
$D + e^- \rightarrow D^+ + 2e^-$	AMJUEL H.4/10 2.1.5	Ionization
$D^+ + e^- \rightarrow D$	AMJUEL H.4/10 2.1.8	Recombination
$D + D^+ \rightarrow D^+ + D$	AMJUEL H.1/3 3.1.8	Charge exchange
$D + D^+ \rightarrow D^+ + D$	AMJUEL H.0 -3 0.1T	Elastic collision
$D_2 + e^- \rightarrow D_2^+ + 2e^-$	AMJUEL H4 2.2.9	Ionization
$D_2 + e^- \rightarrow 2D + 2e^-$	AMJUEL H4 2.2.5g	Dissociation
$D_2 + e^- \rightarrow D_2^+ + D + 2e^-$	AMJUEL H4 2.2.10	Ionizing dissociation
$D_2 + D^+ \rightarrow D_2^+ + D$	AMJUEL H3 3.2.3	Charge exchange
$D_2 + e^- \rightarrow 2D^+ + 2e^-$	AMJUEL H4 2.2.11	Ionizing dissociation
$D_2 + e^- \rightarrow D^+ + D + 2e^-$	AMJUEL H4 2.2.12	Dissociation
$D_2 + e^- \rightarrow D^+ + D + 2e^-$	AMJUEL H4 2.2.14	Recombining dissociation
$D_2 + D^+ \rightarrow D_2 + D^+$	AMJUEL H.0 -3 0.3T	Elastic collision
$He + e^- \rightarrow He^+ + 2e^-$	HYDHEL H.2 2.3.9	Ionization
$He^+ + e^- \rightarrow He$	ADAS H.4 acd96; H.10prb96	Recombination
$He + D^+ \rightarrow He + D^+$	AMJUEL H.0 -3 0.2T	Elastic collision
$He + D^+ \rightarrow He^+ + D$	AMJUEL H.3/9 3.3.1	Charge exchange
$N + e^- \rightarrow N^+ + 2e^-$	AMJUEL H.4/10 2.7A0	Ionization
$N^+ + e^- \rightarrow N$	AMJUEL H.4/10 2.3.7A0	Recombination
$Ne + e^- \rightarrow Ne^+ + 2e^-$	H.2 2.10B0	Ionization
$Ne^+ + e^- \rightarrow Ne$	H.4 acd96; H.10prb96	Recombination

Table 6.2: Reactions included in the Eirene modeling setup

Reactions for the helium from the table (6.2) were used only for the ITER modeling, because in ASDEX Upgrade modeling He was not included. Additional elastic collision reactions were used in the ITER modeling. These reactions were taken from the input files prepared by A. Kukushkin and their impact is discussed in [31].

Elastic collision reactions were not used for AUG.

The convergence control of all presented cases was done by the analysis of the insthr.trc tracing file, produced by the code. In this file, the number of the main ion and impurities particles in the 4 different regions of the tokamak is tracked: core, SOL, inner and outer divertor. The total number of particles in each region for the set of time points in the phase considered converged, was related to the time derivatives of the number of particles in this region (calculated for each time step). This way the characteristic time of the system was estimated. Once this time became significantly large (more than a few seconds) the convergence was considered confirmed.

For all the cases a speed up scheme for the fluid part of the modeling [41] was used. This scheme handles the numerical instability caused by the drift terms in the code. This instability, as indicated in the [41], is connected to the poloidal redistribution of particles inside the separatrix by $E \times B$ drift in combination with modification of the radial electric field by the diamagnetic current. The method of modified preliminary solution was used in both ASDEX Upgrade and ITER modeling. This method introduces the correction factors which stabilize the system by decreasing the density and temperature perturbation on the time step. Implementation of these corrections allows performing calculation with the larger time step without the occurrence of the drift instability. After the preliminary solution is converged (according to the defined above characteristic time), the correction factors are switched off and the real solution is obtained.

For the ITER cases, presented in the current thesis, the corrections were taken as follows: $\alpha_n = 0.002$, $\alpha_t = 0.004$. For the preliminary solution time step of $2 \cdot 10^{-6} s$ was used, for the final solution $2 \cdot 10^{-8}$s.

For the ASDEX Upgrade modeling coefficients were set as follows: $\alpha_n = 0.01$; $\alpha_t = 0.05$; for the preliminary solution time step $1 \cdot 10^{-5}$ was used, for the final $1 \cdot 10^{-6} s$.

6.2 Modeling results

The midplane profiles of the electron density and temperature for all 4 modeling cases, considered in the present thesis, are presented in Figure 6.4. This figure demonstrates a good match throughout the profile for the two seeding species in

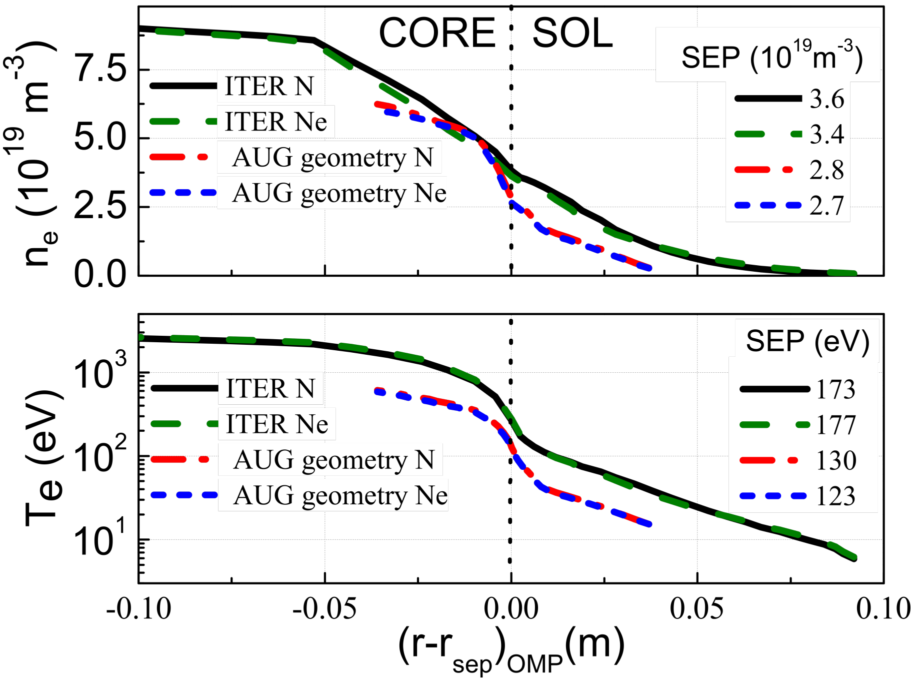

Figure 6.4: Outer midplane distributions and the values at the separatrix of plasma electron density and temperature for all considered cases.

each of the two devices. The effect of the reduced anomalous transport coefficients in the region just inside the separatrix can be clearly seen - in both of the considered devices, the density on the core side of the computational domain is much higher than at the separatrix and the density gradient is present in the near SOL as well. A corresponding gradient is also present in the temperature profiles.

The separatrix density for the AUG geometry modeling cases is lower than for the ITER cases: $3.6 \cdot 10^{19}\text{m}^{-3}$ for ITER with N seeding and $3.4 \cdot 10^{19}\text{m}^{-3}$ for ITER with Ne seeding; $2.8 \cdot 10^{19}\text{m}^{-3}$ for AUG with N seeding and $2.7 \cdot 10^{19}\text{m}^{-3}$ for AUG with Ne seeding. Such a difference can be explained by the higher D puff for the ITER cases.

Separatrix temperature is lower in the AUG modeling cases. For the ITER modeling cases the values of 177 eV and 173 eV were obtained for the N and Ne seeding correspondingly and for AUG 130 eV for N seeding and 123 eV for Ne seeding were obtained. This difference is also expected due to the different input parameters: input power used in the ITER modeling cases is 20 times higher than the one used for AUG.

Independently of the difference, described above, the similar shape of the upstream profiles and the matched percentages of the radiated power in both geometries make the comparison, performed in the present thesis, reasonable. The mechanism of the impurity retention and leakage was the main point of analysis. This mechanism (discussed in the next chapter) is found to be the same in both geometries and it does not depend on the upstream plasma conditions

Divertor neutral pressure values, averaged on the private flux region boundary of the computational domain are ∼ 11.5 Pa for ITER cases and ∼ 9.5 Pa for AUG cases.

The distributions of the electron densities and temperatures in the divertor for all 4 simulation cases are compared in Figs. 6.5 and 6.6 respectively. In Fig. 6.7 the corresponding inner and outer target power flux densities are shown.

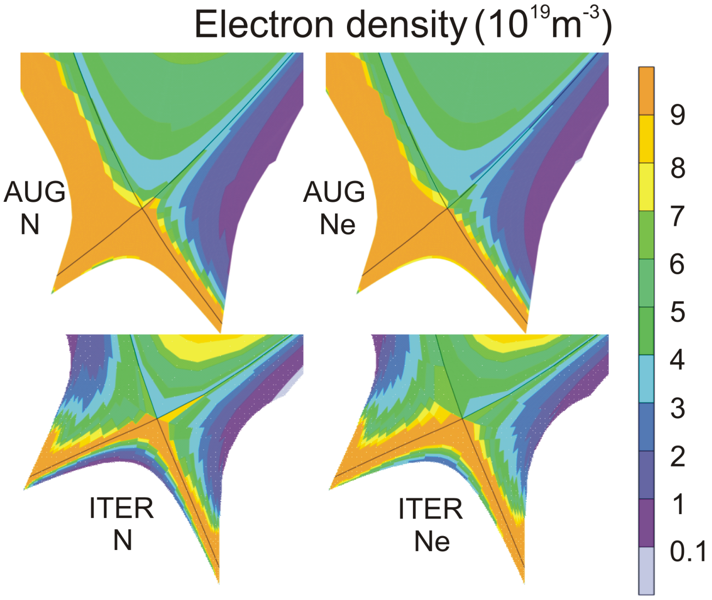

Figure 6.5: Divertor plasma electron density. Top left - AUG N seeding, top right - AUG Ne seeding, bottom left - ITER N seeding, bottom right - ITER Ne seeding.

These distributions illustrate the differences between the large and small scales for comparable relative levels of impurity injection. In AUG, for both N and Ne impurity seeding, an extended area of high density and low temperature is present near the inner divertor target (similar to 'high field side high density' (HFSHD) phenomenon, seen in the experiment [42]). The target power flux density at the inner target is low, which indicates a fully detached state. In contrast, the outer target in the AUG cases is in a partially detached state, with low electron temperature only in the strike point vicinity, much less spread region of high electron density and much more peaked power flux density profiles.

In the ITER modeling results, the distributions of the density and the temperature in the divertor are much more symmetric. The peak of the electron density is still wider at the inner divertor target, but this effect is much less pronounced than in

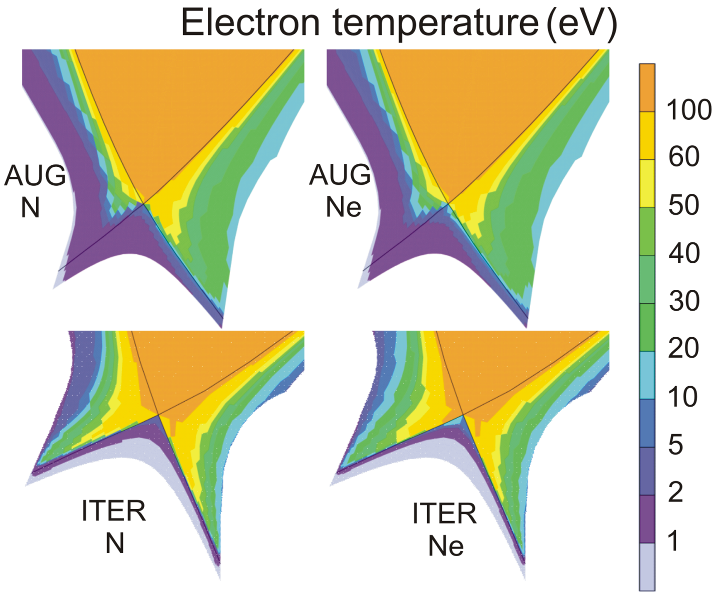

Figure 6.6: Divertor plasma electron density. Top left - AUG N seeding, top right - AUG Ne seeding, bottom left - ITER N seeding, bottom right - ITER Ne seeding.

AUG case. The distribution of the electron temperature and the heat fluxes is also more symmetric in the ITER modeling results. One of the potential reasons for this are weaker ExB drift fluxes through the private flux region. This effect is partially described in [21], but more studies are required to confirm it.

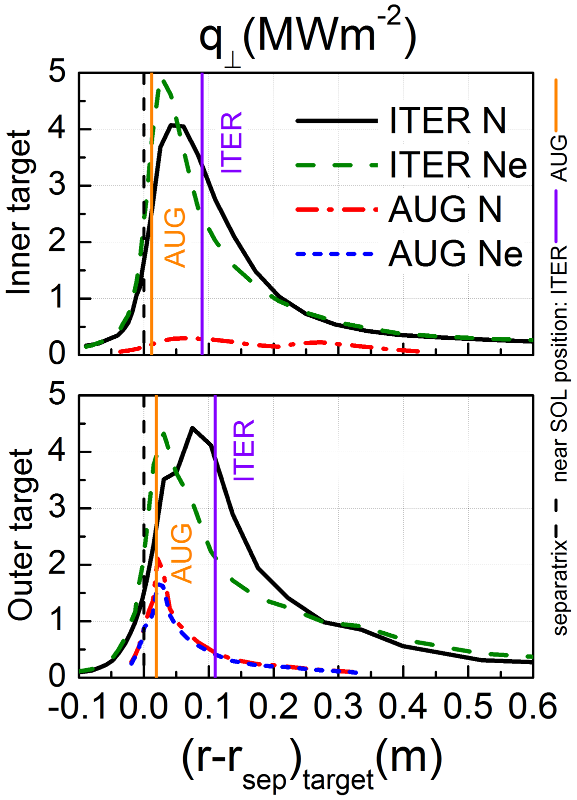

Figure 6.7: Power flux density profiles at inner (top) and outer (bottom) targets for the 4 model cases. The vertical lines mark the extent of the near-SOL (fluxed tubes close to separatrix projected onto the target): 9mm and 11 mm at the inner and outer targets respectively for ITER and 1.2 mm and 1.9 mm for AUG.

Chapter 7

Impurity retention and leakage: comparison of N and Ne behaviour in the ITER and ASDEX Upgrade modeling results

In order to reduce the power loads on the divertor target plates, impurity seeding can be used to [43]. Processes of impurity retention and leakage in the tokamak divertor become important when one considers the detachment regime achieved by impurity seeding . Retention of the impurity in the divertor volume is beneficial for the detachment scenario: this way the radiation by the impurity line emission stays in the divertor volume. Radiative losses allow to achieve the reduction of the heat fluxes to the divertor targets. At the same time if most of the impurity stays in the divertor volume, it does not contaminate the core plasma and does not lead to the losses of the power in the core.

Leakage of the impurity from the divertor volume is the process which leads to the opposite situation: impurity ions escape the divertor and are transported to the upper SOL. This way core plasma contamination becomes much more probable and radiation losses by the impurity line radiation can occur and cause losses of the power in the core.

In previous studies [22] the following mechanism of impurity retention and leakage was suggested. The parallel velocity of impurity ions is determined through the parallel momentum balance equation for these ions. In its stationary form, this balance is dominated by four terms: friction force, thermal gradient force, pressure gradient force and electric force. This balance can be formulated as follows:

$$S_{\mathrm{Fr_a}} + S_{\mathrm{Therm_a}} - \nabla_{||} n_a T_i - e z_a n_a \nabla_{||} \phi = 0 \tag{7.1}$$

Here $S_{\mathrm{Fr_a}}$ - friction force acting on the impurity ion species a, $S_{\mathrm{Therm_a}}$ - thermal force, acting on them; $\nabla_{||} n_a T_i$ - pressure gradient force; $ez_a n_a \nabla_{||}\phi$ - electric force.

In most of the upper SOL, the balance is determined by the balance of the friction and the thermal force. All other forces, which are present in the equation, are usually at least one order of magnitude smaller. This statement was already discussed in [19].

From the balance of the friction and thermal force the following model for impurity retention or leakage was suggested: if the friction force with the main ions is larger than the thermal force, impurity ions are retained in the divertor. If the thermal gradient force is larger, impurity ions are dragged upstream and it causes impurity leakage.

This model was found to be not applicable to the analyzed SOLPS-ITER modeling results. In all the considered cases the friction and thermal force, acting on the impurity ions, are found to be in balance. This balance was also found to be the same for N and Ne seeded simulations. Since N is found to be better retained in the divertor volume, impurity retention or leakage in the considered cases has to be determined by additional physics.

It was found in the simulations, that the ionization fronts of N and Ne are located differently with respect to the D ionization front in all the cases considered. For the modeling results with the matched plasma backgrounds - similar electron temperature and density distribution in the divertor and upstream SOL - in the N seeded cases first impurity ionization always happened closer to the divertor target than the fuel ions ionization and in the Ne seeded cases impurity always ionized further upstream. This fact stays the same for both analyzed geometries and it seems to be the determining factor for the difference between nitrogen and neon retention and leakage.

7.1 SOL velocity structure in the SOLPS-ITER modeling. Main ions reverse flow

Now it is important to mention the structure of the ion flux in the divertor SOL [4]. For the main ion flux in the analyzed modeling results the return flow is present in the near SOL of the outer divertor for both geometries (AUG and ITER).

This region - near SOL in the outer divertor - in ASDEX Upgrade is the most important one in the context of impurity divertor retention. The inner divertor in

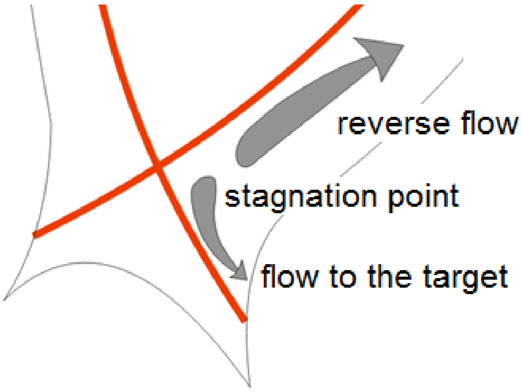

Figure 7.1: Reverse flow pattern in the outer divertor.

the AUG geometry is always in the higher recycling state and retains impurities better than the outer. The near SOL is the most important area in the boundary plasma analysis since the amplitude of the heat and particle fluxes in the outer SOL is at least one order of magnitude lower.

The structure of the outer divertor near SOL in both AUG and ITER modeling results for the main ion flux features the reverse flow pattern for the main ions. By reverse flow pattern the following is meant: close to the target, the flux of the main ions is directed towards the target and further upstream it stagnates and goes towards the equatorial midplane, as it is shown in Fig. 7.1.

The position of the main ion flow stagnation is located approximately at the ionization front peak. This connection can be explained by the pressure gradient which arises from the ion density source. The position of the stagnation point can still be shifted by the cross field drifts effects and by the drifts caused by the magnetic field gradient. The effect of the drifts on the impurity retention and leakage for nitrogen and neon SOLPS-ITER simulations is discussed in [6] and in [4]. The effect of the drifts on the argon retention and leakage is studied in [44].

7.2 Impurity ions velocity

The impurity ion flow is connected to the main ion flow through the friction force. The stagnation point of impurity ions can be shifted from the main ions stagnation point by the temperature gradient force. This statement can be formalized through the thermal and friction force balance for impurities mentioned above.

The friction force can be estimated as $S_{\mathrm{Fr_a}} \sim \alpha z_a^2 \tau^{-1} n_a m_a \left(v_{||_i} - v_{||_a}\right)$, the thermal force as $S_{\mathrm{Therm_a}} \sim \beta z_a^2 n_a \nabla_{||} T_i$. From the fact that these two forces should be balanced one can estimate the impurity velocity: $v_{||_a} \sim v_{||_i} + \frac{\beta}{\alpha} \tau m_a^{-1} \nabla_{||} T_i$.

Here

- $v_{||_a}$ and m_a are the parallel velocity and the mass of the impurity ion species a;
- $v_{||_i}$ is the main ion parallel velocity;
- τ is the collision time for the main ions;
- n_i is the main ion density;
- $\nabla_{||}T_i$ is the parallel projection of main ion temperature gradient;
- α, β are numerical coefficients.

The first contribution reflects the connection to the main ions; the second one reflects the temperature gradient force. Considering the location of the stagnation point position for the impurity ions, the impurity ion's velocity will stagnate approximately at the main ions stagnation point position, if the temperature gradient is not very high.

In Fig. 7.2 the near SOL impurity and the main ion parallel velocities are compared. In this comparison one can notice that for ITER modeling results impact of the thermal force is larger and can in principle increase leakage. This applies to both N and Ne seeding.

For the AUG cases in Fig. 7.2 the velocity difference provided by the ion temperature gradient force is essentially negligible for both Ne and N and is therefore not the most important player governing impurity leakage from the divertor.

For the ITER case, Fig. 7.2 shows that there are larger differences between the velocities of the impurity and main ions. The difference is provided by the thermal force produced mainly by ion temperature gradient which pushes the stagnation point of impurities towards the divertor. This is unfavorable for impurity retention for both impurities and both inner and outer divertors. This is unlike AUG where impurity flow reversal on the considered flux surface only occurs for Ne and only at the outer divertor.

7.3 Impurity retention and leakage

For impurity retention or leakage, the interplay of the position of the stagnation point and of the impurity ionization front is crucial. Before ionization occurs, impurity particles do not feel the magnetic field and can freely permeate the divertor volume. After the first ionization occurs, impurity ions are strongly connected to the parallel transport pattern and can only move with the ion flow - back towards the

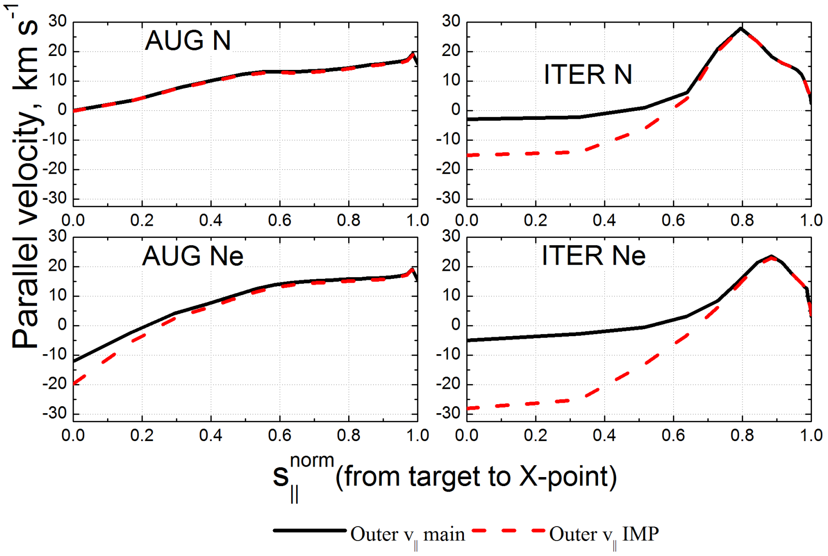

Figure 7.2: Main ion (solid) and impurity ion (dashed) parallel velocity profiles along the normalized parallel distance $s_{||}$ for the flux tubes close to the separatrix ($(r - r_{\mathrm{sep}})_{\mathrm{omp}} = 1.6$mm for ITER case, ($(r - r_{\mathrm{sep}})_{\mathrm{omp}} = 0.35$mm for AUG) at the outer divertor for the AUG and ITER Ne seeded model cases. $s_{||} = 0$ corresponds to the X-point, $s_{||} = 1$ corresponds to the outer target.

target if the ionization occurs below the stagnation point of the ion flow or upstream towards the main SOL if ionization happened above.

For all modeling cases considered, in the near SOL N ionized below (closer to the divertor targets in the poloidal direction) the D and Ne ionized above (closer to the equatorial midplane). This statement is valid for both ITER and ASDEX Upgrade geometries, see Fig 7.3. For the AUG cases, the difference between stagnation point position of N and Ne is noticeable only in a few first cells in the near SOL, but this position coincides with the position of the ionization source peak, which leads to the difference in the impurity leakage. For ITER, the difference between N and Ne stagnation is more pronounced, but both stagnation points are located further away from the impurity ionization peaks. This weakens the impurity leakage effect for ITER modeling for both N and Ne, but still Ne escapes more to the upper SOL in comparison to N.

From the SOLPS-ITER modeling point of view, Ne will be more spread in the upper SOL of ITER, as well as it is in ASDEX Upgrade. Nevertheless in the comparison of the modeling results of Ne and N seeding in AUG versus ITER provides an indication on the Ne suitability for ITER. This difference takes place in the radiated power distributions and it is discussed in the next section.

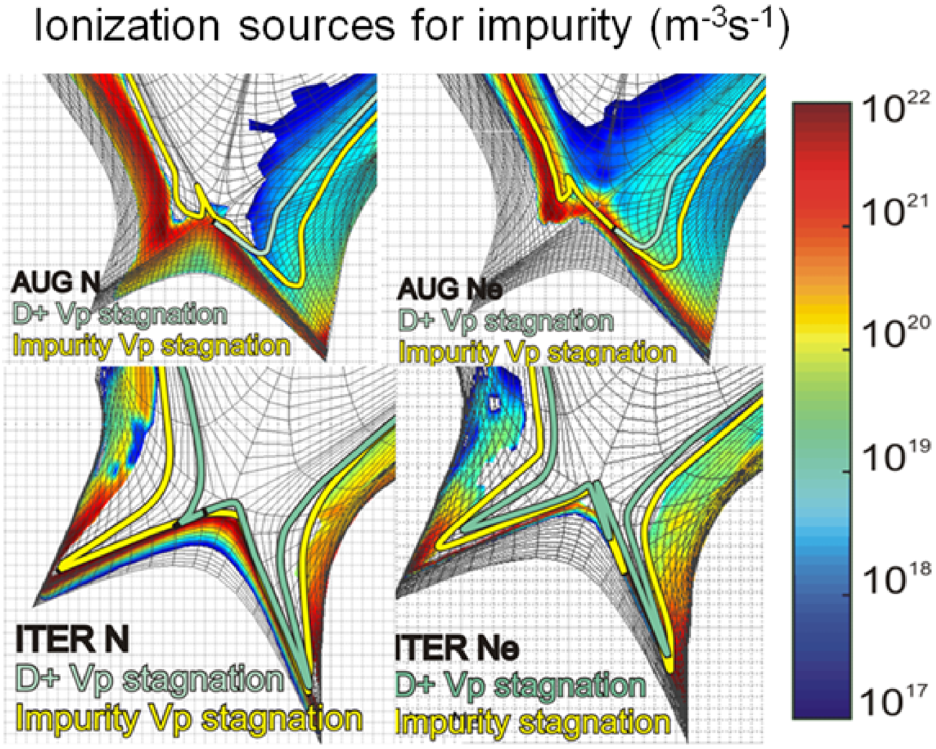

Figure 7.3: Impurity ionization source distribution ($m^{-3}s^{-1}$). Green lines - D^{+1} ions stagnation point position, yellow lines - impurity ions stagnation point position.

7.4 Radiative patterns of Ne and N in ASDEX Upgrade and ITER modeling results

Distribution of the radiated power was analyzed for all 4 considered cases, Fig 7.4. In both ASDEX Upgrade and ITER geometries, radiation is more spread towards the upper SOL in the Ne seeded cases, consistent with the conclusion of the previous section of higher ability of Ne to escape the divertor volume. Fractions of the power, radiated in the divertor volume and in the core region is shown in Table 7.1.

	P_{rad_tot}/P_{in}; $P_{rad\_tot}(MW)$	P_{rad_div}/P_{in}; $P_{rad\_div}(MW)$	P_{rad_SOL}/P_{in}; $P_{rad\_SOL}(MW)$	P_{rad_core}/P_{in}; $P_{rad\_core}(MW)$
ITER N	0.6 (60)	0.53 (53)	0.05 (5.3)	0.02 (2)
ITER Ne	0.67 (67)	0.53 (53)	0.085 (8.5)	0.05 (5)
AUG N	0.48 (2.4)	0.33 (1.6)	0.12 (0.61)	0.03 (0.15)
AUG Ne	0.52 (2.6)	0.23 (1.18)	0.16 (0.84)	0.13 (0.56)

Table 7.1: Fractions of the radiated power to the input power: in the whole domain (column 1) and by regions (columns 2-4)

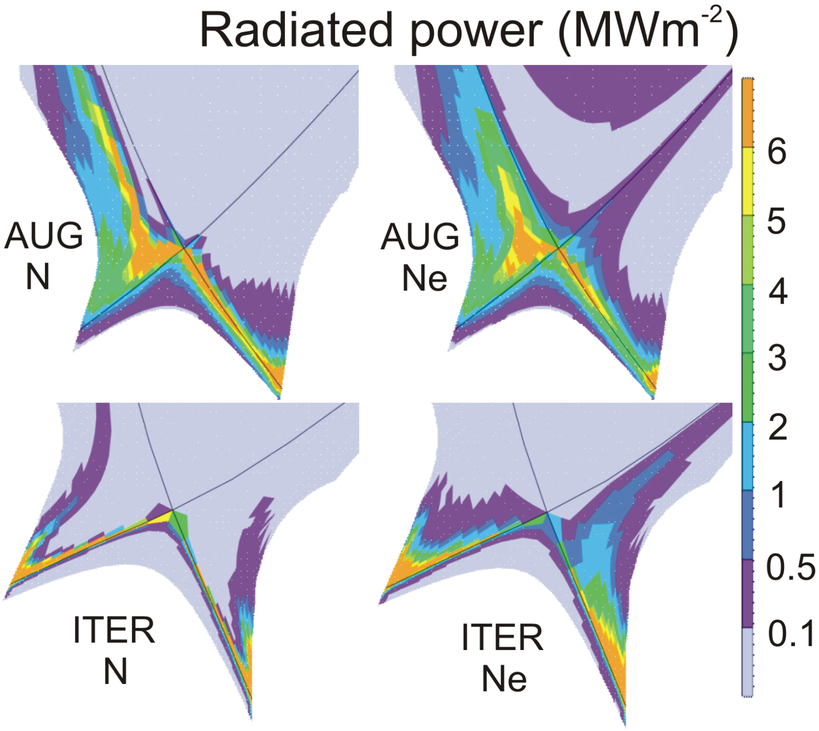

Figure 7.4: Radiated power distribution in ASDEX Upgrade (upper row) and ITER (lower row) cases with N (left column) and Ne (right column) seeding.

Important differences are present in the radiated power distributions between ASDEX Upgrade and ITER geometries:

- For both Ne and N seeding, the radiated power peak in the ASDEX Upgrade cases is localized around the X-point. In the ITER cases the peak of the radiated power for both seeded impurities is localized around the divertor targets strike point.

This difference is partially coming from the different radiative scenarios in these two geometries. In AUG geometry one can claim that the X-point radiative scenario is present. At ITER the situation is different: no cooling down of the X-point is present and the cold plasma layer is only present at the strike point vicinity of the divertor target. Therefore one can claim that chosen exhaust scenario in two different geometries are not comparable.

A counterargument for this statement is as follows: for the considered ITER cases radiated power is 61% of the input power for N seeded case and 67% of the input power for Ne seeded cases. In the considered ASDEX Upgrade cases, only 48% of input power is radiated for N seeded case and 51% of the Ne seeded case. In the ASDEX Upgrade geometry a smaller percentage of the input power radiated leads to the more intense radiative exhaust scenario - in ITER more input power can be radiated without going into X-point radiation.

One can argue that ITER geometry cases stayed further away from the X-point radiation regime due to the higher input power. This claim can be partially balanced with an argument that input powers in both geometries were calibrated in the way to stay close to L-H transition threshold ($P_{sep}/P_{LH} \sim 2$), therefore usage of the higher input power for ASDEX Upgrade geometry in this study would not be reasonable.

- In the ASDEX Upgrade geometry cases radiation is less divertor localized: for N seeded case 33% and for Ne seeded case 23% of the total input power is radiated in the divertor volume. In contrast, in the ITER geometry cases 53% of input power is radiated in the divertor volume. The reason for these difference is suggested to be as follows: due to the higher heating power in the ITER divertor temperature stays higher further in the divertor and thus radiative impurity charged states cannot escape the divertor target strike point vicinity.
- In the ASDEX Upgrade geometry for the Ne seeded case significant core radiation (13% of total input power) is present. The difference between this value and the AUG geometry N seeded case core radiation (3%) is more than 4 times. In the ITER geometry, Ne seeded case has only 5% of total radiation coming from the core region and the difference to the N seeded case is only 2.5 times (2%). These facts allow to suggest better suitability of Ne exhaust scenarios for larger divertors with higher heat fluxes.

The main reason of the discussed differences between radiated power distributions are mentioned before: the larger ITER divertor allows to contain the detachment front deep inside the divertor region far away from the X-point and higher powers in the ITER SOL allow to maintain the temperature higher further away from the X-point. Both facts result in the different distribution of the impurity radiative charged states in the divertor volume.

Most of the radiation power is coming from the not fully stripped (ionized) impurity ions. In the cases considered with Ne seeding most of the radiation is coming from $Ne^{+1} - Ne^{+6}$. Higher ionization states provide much lower radiated power, see Table 7.2.

Distribution of the charged states of impurity in the near SOL below the X-point together with the electron temperature in the same region is presented in Fig. 7.5 : for instance, Ne^{+5} exist in the X-point vicinity as 40% of the total impurity there.

	$Ne^{+1} - Ne^{+2}$	Ne^{+3}	Ne^{+4}	Ne^{+5}	Ne^{+6}	$Ne^{+7} - Ne^{+10}$
AUG	15.7	20.2	30	20.9	7.1	2.1
ITER	8,4	18.2	22.3	23.4	23.1	4.6

Table 7.2: Distribution of the radiated power between Ne charged states in AUG (upper row) and ITER geometry modeling cases.

In ITER all radiative charged states decrease below 20% at the X-point region. This means that radiation in the ITER modeling results is well compressed near the divertor targets even for the Ne seeded case.

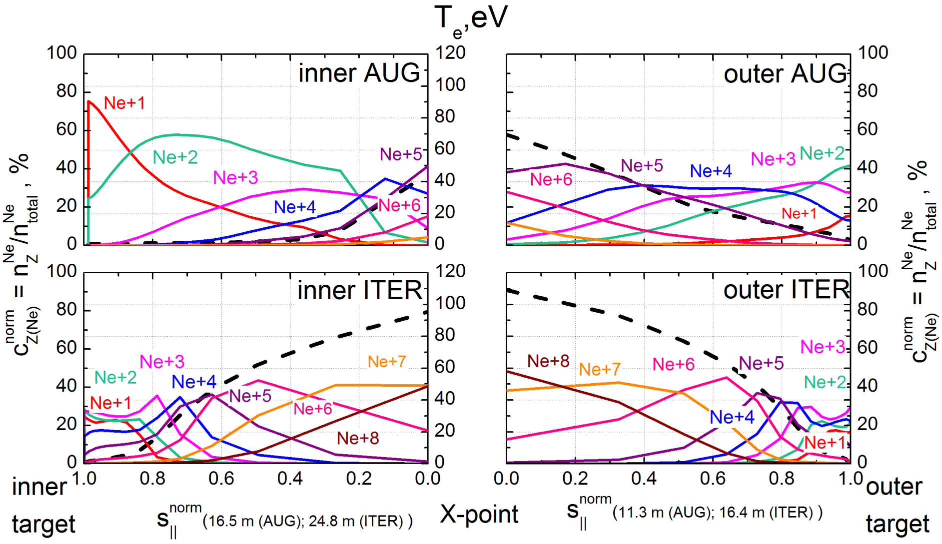

Figure 7.5: Distributions of the normalized Ne charged states densities: each charged state density is divided by the total impurity density and presented in percents. Dashed line represents electron temperature. Horizontal axis is given in the normalized connection length: on the l.h.s. from the inner target to the X-point and on the r.h.s. from the X-point to the outer target.

Significant differences in the radiated power distributions in ITER and ASDEX Upgrade cases, as mentioned above, are partially coming from the very different distributions of the temperature in the divertor region, Fig 7.6. These differences are partially caused by much higher heating power in the ITER case, 100 MW versus 5 MW in ASDEX Upgrade case.

These differences, as discussed above, can cast doubt on the comparability of the considered ITER and AUG modeled cases. It is also mentioned above that input powers for both machines were selected such as to be close to the L-H transition threshold (($P_{sep}/P_{LH} \sim 2$). For the selected input powers and impurity radiation levels the conclusion is that overall impurity retention is better in the modeling results for ITER parameters. Further analysis suggest that the Ne seeding can be used at ITER without core contamination. In SOLPS-ITER modeling results for AUG parameters Ne core contamination is present and it causes impurity radiation there, which goes in line with the experimental observations [13].

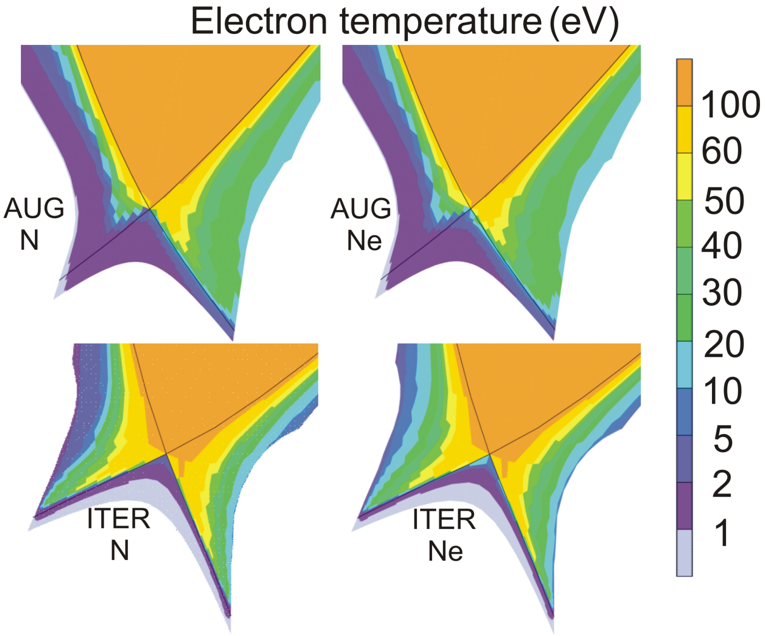

Figure 7.6: Distribution of the electron temperature in the divertor region of ASDEX Upgrade (upper row) and ITER (bottom row) modeling results. N seeded cases (left column) and Ne seeded cases (right column) do not differ significantly within each device setup.

Chapter 8

Conclusion and outlook

This PhD project had three important parts - improvement of the parallel momentum balance equation (PMBE) in the SOLPS-ITER code, modeling of the ASDEX Upgrade and ITER scenarios with the code and the analysis of the modeling results.

All the parts served the following goals:

- Improve the impurity transport description in the SOLPS-ITER code and obtain clear analytical formulation of the friction and the thermal force terms;
- Compare the behaviour of the detached plasma modeling results in ASDEX Upgrade and ITER geometries;
- Reproduce in the modeling the difference between nitrogen and neon behavior in the SOL of ASDEX Upgrade which is seen in the experiment; obtain a qualitative explanation of this behaviour;
- Compare nitrogen and neon behaviour in the SOL of the ITER modeling results. On the basis of this comparison make a prediction about which of the two impurities is going to be suitable for ITER detachment operations.

8.1 Improvement of the PMBE

The first part of the present thesis work was the modification of the Parallel Momentum Balance Equation for ions in SOLPS. This modification was required for a better description of the impurity transport in the code. The previous version was derived in the limiting assumptions on the ions velocities and on the impurity content. The new version is an analytical expression directly taken from the Braginskii equations [28].

For the Braginskii form of the equations friction and thermal force terms were derived and implemented. These terms had to be modified from the Braginskii expression, because in [28] only the simple plasma case (plasma without impurities) was considered.

To derive analytical expressions for thermal and friction force terms their descriptions given in [29] were used. On the basis of the algorithms suggested there new terms were derived. In this thesis framework these terms were first derived in the trace impurities approximation. Results of this derivation were implemented in the SOLPS. They were tested on the ASDEX Upgrade geometry scenario and an instability connected to the impurity accumulation was found for the case with the high impurity seeding.

After that friction and thermal force terms were improved by impurity dependent correction coefficients. This improvement was implemented in the code and tested on the same modeling case. In this case, an impurity accumulation instability did not occur.

Modeling results obtained with the Braginskii form of PMBE, newly implemented into SOLPS, were compared with the modeling results obtained with the old form of PMBE. Differences in the impurity distribution were found: the Braginskii form of the equation resulted in more impurity leakage from the divertor volume. Since this form of the equation required fewer assumptions in the derivation process, this result was considered to be more realistic. Trace impurity assumption in this implementation is lifted to the large extent. However, the impurity temperature gradient term in this derivation is still neglected as a second-order term with respect to the impurity density.

The more general Braginskii form of PMBE resulted in an impurity distribution which is less beneficial for the divertor detachment scenario. Due to this fact, it was important to push the more general form of PMBE into the master version of SOLPS. This was managed first at the Saint-Petersburg development team level and then at the ITER code management level. All the further modeling, performed and analyzed in the present thesis framework, was done with the Braginskii form of PMBE implemented.

8.2 Impurity retention and leakage mechanism

Neon and nitrogen impurity behaviour in the SOLPS modeling results was analyzed in the present thesis for ASDEX Upgrade and ITER scenarios. The same mechanism of the impurity leakage form the divertor was found in both AUG and ITER: in a first approximation, impurity ions escaped the divertor with the main ion reverse flow. This flow is connected to the impurity ions by the friction force and drags them upstream.

The defining factor for the amount of the impurity ions retained of the divertor was the interplay between the location of the ionization of these impurity neutrals and the start of the main ions reverse flow. Main ions reverse flow in the modeling at the first approximation can be connected to the main ion ionization from the neutral state.

This allows one to simplify the impurity leakage criteria to the following: impurities, which ionize closer to the divertor target than the main ions, are retained in the divertor and contribute to the detachment of the targets. Impurities, which are ionized from the neutral state further away from the target than the main ions, get dragged to the upper SOL. These impurity ions contribute less to the detachment formation and are more likely to cause core impurity contamination.

The starting point of the main ions reverse flow can be connected in a simplified manner to the position of the main ions ionization from the neutral to the first charged state. This location is connected to the peak of the main ions pressure gradient due to the presence of the source. From this place two fluxes are created to compensate this pressure gradient: one towards the target and the other towards the upstream (the reverse flow). The full picture of the reverse flow formation is more complicated and includes the drift flows. All these effects were taken into account in the modeling.

8.3 Nitrogen and Neon retention and leakage

A mechanism, explained in the previous section, was used to study the difference of the neon and nitrogen transport in the analyzed modeling results.

One of the tasks of the present thesis was to explain from the modeling point of the view, why it is possible to get a stable detachment scenario at ASDEX Upgrade with nitrogen seeding and impossible to get it with neon seeding. The main reason, from the modeling point of view, is that nitrogen neutrals ionize closer to the divertor target than the main ion neutrals and neon neutrals ionize further away.

This fact in the ASDEX Upgrade modeling leads to the very different distribution of the radiated power in the neon and nitrogen seeded cases. In the nitrogen seeded case radiation stays relatively well compressed in the divertor region (although it spreads towards the X-point) and in the neon seeded case the core radiation is present. It should be taken into account that the compared nitrogen and neon seeded cases have similar fraction of the total input power radiated: 48 % in the nitrogen seeded case and 52% in the neon seeded case. Even for similar amounts of the radiated power the two gases behave differently.

In the ITER modeling results the distributions of the nitrogen and neon also show that neon escapes the divertor more than the nitrogen, and spreads in the upper SOL. However in the ITER parameters the more pronounced spreading of neon does not make a significant difference in the radiative patterns: in the analyzed cases with nitrogen and neon impurity seeding, similar total level of radiated power (60% for N, 67% for Ne) corresponded to the similar percent of the power, radiated in the divertor volume (53% for both cases). This suggests that Ne would be a suitable radiator in the ITER conditions.

8.4 Nitrogen and Neon radiation patterns in ASDEX Upgrade and ITER SOLPS modeling

An explanation of the different radiative patterns in ASDEX Upgrade and ITER is provided through the different divertor temperature distributions in the modeling results.

In the ASDEX Upgrade scenario modeling results the cold plasma area, in which most of the radiation occurred, extended up to the X-point. This feature was present in both N and Ne seeded cases.

Such a distribution of the temperature allows the radiation to escape the divertor volume in the AUG case. Conditions for the efficient impurity radiation extend to the main SOL and can even be present in the core region. This is why in case of the impurity leakage from the divertor (like in the neon seeded cases) the total radiated power in the SOL and core regions increases strongly.

In the ITER modeling results, due to the heating power and size differences, the cold plasma area stays much closer to the divertor targets and does not extend to the upper SOL and core regions.

This makes the impurity leakage from the divertor much less dangerous: in the chosen radiated power level, the temperature distribution organizes in such a way that the conditions for the impurity radiation are present only in close vicinity of the divertor target strike points.

8.5 Outlook

In the present thesis an important modification of the SOLPS-ITER code was done, modeling results for AUG and ITER input parameters with nitrogen and neon seeding were obtained and analyzed. On the basis of the analyzed modeling results the impurity retention and leakage mechanism was suggested. Through this mechanism the nitrogen and neon behaviour in the modeling results was explained. For AUG modeling, results were consistent with the experimental observations of less divertor radiation in the neon seeding case. For the ITER modeling, results more neon leakage, than nitrogen, was observed, but the radiation pattern stayed the same with both seeded impurities. Difference in the radiative patterns between AUG and ITER was explained through the different temperature distributions in the divertor region.

From the ASDEX Upgrade modeling point of view, the main drawback of the present thesis is the absence of a properly benchmarked experimental case. This benchmark would be an interesting contribution in the SOLPS-ITER validation. This task is a very complex one both from the point of view of the experimental data collection and from the modeling point of view - for instance, transport coefficients adjustments to achieve the correct radial profiles can take several months.

For ITER modeling it is necessary to achieve further understanding of the obtained temperature profiles. More studies are required on the drift impacts estimation. Absence of strong asymmetries in the modeling results can probably be explained from the less significant drift impact on ITER. Partially this analysis is performed in the paper which will be published by the Saint-Petersburg team in 2020 [7]. Another point, which could be addressed in future modeling analysis, is the compression of neutral N (in a cold regions, not affecting the radiation) for ITER than for AUG. To achieve similar fractions of radiated power an increased ratio ($\sim$ factor 6) of impurity to fuel throughput is required for ITER in comparison to AUG. The precise reasons for this different behavior of neutral N at the two different size scales are not currently understood and should be studied in the future.

Another important point, raised in [45] is the grid resolution, which might be not fine enough to fully capture the ITER physics. In the present study, the standard ”coarse” numerical grid for ITER with 30 cells in the radial direction and 96 cells in the poloidal direction was used. However, since the differences mentioned in [45] were of the quantitative and not the qualitative character, most probably even with the new profiles, obtained with the finer grids, the peak temperature gradient at ITER would still be located in the strike point vicinity. Therefore the suggested impurity transport mechanism and impurity radiation pattern for ITER would remain unchanged.

The grid analysis problem for ASDEX Upgrade modeling is less critical since for a significantly smaller device a mesh with 36 cells in the radial direction and 96 cells in the poloidal direction were used. The same grid resolution was used in the SOLPS modeling study with the experimental benchmark achieved [2]. Nevertheless, it would indeed be a very interesting future study, for instance, to refine and adapt the grid once the experimental benchmark is achieved and study the new possible effects brought up by the refined grid. Still, the suggested mechanism of the impurity transport would most probably generally stay the same with the probable corrections coming from the changes in the temperature and the density of the main ions distributions.

Bibliography

[1] C. Theiler. *Basic Investigation of Turbulent Structures and Blobs of Relevance for Magnetic Fusion Plasmas*. PhD thesis. 2011.

[2] F. Reimold. *Experimental Studies and Modeling of Divertor Plasma Detachment in H-Mode Discharges in the ASDEX Upgrade Tokamak*. PhD thesis. 2014.

[3] S. Potzel. *Experimental classification of divertor detachment*. PhD thesis. 2012.

[4] I.Senichenkov et al. "On mechanisms of impurity leakage and retention in the tokamak divertor". In: *Plasma Physics and Controlled Fusion* 61.4 (2019).

[5] V. Rozhansky et al. "New B2SOLPS5.2 transport code for H-mode regimes in tokamaks". In: *Nuclear Fusion* 49.2 (2009), p. 025007.

[6] Elizaveta Sytova et al. "Comparing N versus Ne as divertor radiators in ASDEX-upgrade and ITER". In: *Nuclear Materials and Energy* 19 (2019), pp. 72–78. ISSN: 2352-1791.

[7] Elizaveta Kaveeva et al. "SOLPS-ITER modelling of ITER edge plasma with drifts and currents". In: *Nuclear Fusion* (2020).

[8] R. Pitts et al. "Physics basis for the ITER tungsten divertor". In: *Nuclear Materials and Energy* 23 (2019).

[9] L Spitzer. "The Stellarator Concept". In: *The Physics of Fluids* 1.4 (1958), pp. 253–264.

[10] S. I. Krasheninnikov and A. S. Kukushkin. "Physics of ultimate detachment of a tokamak divertor plasma". In: *Journal of Plasma Physics* 83.5 (2017), p. 155830501.

[11] M. E. Fenstermacher et al. "The two-dimensional structure of radiative divertor plasmas in the DIII-D tokamak". In: *Physics of Plasmas* 4.5 (1997), pp. 1761–1773.

[12] H. D. Pacher et al. "Impurity seeding in ITER DT plasmas in a carbon-free environment". In: *Journal of Nuclear Materials* 463 (2015), pp. 591–595.

[13] M.Bernert et al. "Power exhaust by SOL and pedestal radiation at ASDEX Upgrade and JET". In: *Nuclear Materials and Energy* 12 (2017), pp. 111–118.

[14] D. Reiter, M. Baelmans, and P. Börner. "The EIRENE and B2-EIRENE Codes". In: *Fusion Science and Technology* 47.2 (2005), pp. 172–186.

[15] A. Kukushkin et al. "Finalizing the ITER divertor design: The key role of SOLPS modeling". In: *Fusion Engineering and Design* 86 (Dec. 2011), pp. 2865–2873.

[16] X. Bonnin et al. "Presentation of the New SOLPS-ITER Code Package for Tokamak Plasma Edge Modelling". In: *Plasma and Fusion Research* 11 (2016), p. 1403102.

[17] V. Rozhansky. "Drifts, Currents, and Radial Electric Field in the Edge Plasma with Impact on Pedestal, Divertor Asymmetry and RMP Consequences". In: *Contributions to Plasma Physics* 54.4-6 (2014), pp. 508–516.

[18] V. Rozhansky et al. “Electric fields and currents in the detached regime of a tokamak”. In: *Contributions to Plasma Physics* 58.6-8 (2018), pp. 540–546.

[19] E. Sytova. *Analysis of impurity momentum balance and flows in the SOL by SOLPS-ITER modelling.* Proceedings of 43rd EPS Conference on Plasma Physics. Leuven, Belgium, 2016.

[20] V. Rozhansky. “Simulation of tokamak edge plasma including selfconsistent electric fields”. In: *Nuclear Fusion* 41.4 (2001), pp. 387–401.

[21] E. Sytova et al. “Impact of a new general form of friction and thermal forces on SOLPS-ITER modelling results”. In: *Contributions to Plasma Physics* 58.6-8 (2018), pp. 622–628.

[22] P. Stangeby. *Transport Processes in a Plasmas.* The Plasma Boundary of Magnetic Fusion Devices. Series: Series in Plasma Physics, Taylor & Francis, Edited by Peter Stangeby, vol. 7, 2002.

[23] B. LaBombard et al. “Transport-driven Scrape-Off-Layer flows and the boundary conditions imposed at the magnetic separatrix in a tokamak plasma”. In: *Nuclear Fusion* 44.10 (2004), pp. 1047–1066.

[24] Y. Feng et al. “Recent Improvements in the EMC3-Eirene Code”. In: *Contributions to Plasma Physics* 54.4-6 (2014), pp. 426–431.

[25] G. Ciraolo et al. “First modeling of strongly radiating WEST plasmas with SOLEDGE-EIRENE”. In: *Nuclear Materials and Energy* 20 (2019), p. 100685.

[26] R. Simonini et al. “Models and Numerics in the Multi-Fluid 2-D Edge Plasma Code EDGE2D/U”. In: *Contributions to Plasma Physics* 34.2-3 (1994), pp. 368–373.

[27] M.E. Fenstermacher et al. “UEDGE and DEGAS modeling of the DIII-D scrape-off layer plasma”. In: *Journal of Nuclear Materials* 220-222 (1995). Plasma-Surface Interactions in Controlled Fusion Devices, pp. 330–335.

[28] S. I. Braginskii. “Transport processes in a plasma”. In: *Reviews of Plasma Physics* 1 (1965).

[29] V M Zhdanov. “Transport Processes in Multicomponent Plasma”. In: *Plasma Physics and Controlled Fusion* 44.10 (Sept. 2002), pp. 2283–2283.

[30] B. Braams. “A Multi-Fluid Code for the Simulation of the Edge Plasma in Tokamaks”. In: *NET Report* (1987).

[31] V. Kotov. “Numerical study of the ITER divertor plasma with the B2-Eirene code package”. In: *PhD Thesis JUEL–4257* (2007).

[32] A. Kukushkin and H.D. Pacher. “Neutral recirculation - The key to control of divertor operation”. In: *Nuclear Fusion* 56 (Dec. 2016), p. 126012.

[33] S. Wiesen et al. “The new SOLPS-ITER code package”. In: *Journal of Nuclear Materials* 463 (Aug. 2015), pp. 480–484.

[34] B. Braams. *A Multi-Fluid Code for Simulation of the Edge Plasma in Tokamaks.* Report. 68 EUR-FU /XII-80/87/68. 1987.

[35] B. Braams. “Radiative Divertor Modelling for ITER and TPX”. In: *Contributions to Plasma Physics* 36.2–3 (1996), pp. 276–281.

[36] Coster D. P. “SOLPS 5.0 presentation”. In: *EFDA JET meeting* (2002).

[37] V. Rozhansky et al. “Momentum balance for impurities in SOLPS transport code”. In: *Journal of Nuclear Materials* 463 (2015), pp. 477–479.

[38] F. Reimold et al. "Divertor studies in nitrogen induced completely detached H-modes in full tungsten ASDEX Upgrade". In: *Nuclear Fusion* 55.3 (2015), p. 033004.

[39] R. Balescu. *Transport processes in plasmas.* 1998.

[40] D. Reiter. *The EIRENE Code User Manual including: B2-EIRENE interface.* 2019.

[41] E. Kaveeva et al. "Speed-up of SOLPS-ITER code for tokamak edge modeling". In: *Nuclear Fusion* 58.12 (Oct. 2018), p. 126018.

[42] F. Reimold et al. "The high field side high density region in SOLPS-modeling of nitrogen-seeded H-modes in ASDEX Upgrade". In: *Nuclear Materials and Energy* 12 (2017). Proceedings of the 22nd International Conference on Plasma Surface Interactions 2016, 22nd PSI, pp. 193–199.

[43] P. Monier-Garbet et al. "High radiation from intrinsic and injected impurities in Tore Supra ergodic divertor plasmas". In: *Journal of Nuclear Materials - J NUCL MATER* 290 (Mar. 2001), pp. 925–929.

[44] T.W. Petrie et al. "Impurity behaviour under puff-and-pump radiating divertor conditions". In: *Nuclear Fusion* 49 (May 2009), p. 065013. DOI: `10.1088/0029-5515/49/6/065013`.

[45] K. Ghoos et al. "Grid resolution study for B2-EIRENE simulation of partially detached ITER divertor plasma". In: *Nuclear Fusion* 59.2 (Dec. 2018), p. 026001.

Acknowledgments

I would like to thank to the Erasmus+ Fusion DC program for funding the first 3 years of my Ph. D. and giving me a possibility to work and study in Europe. I would also like to thank Frank Jenko for giving me the possibility to finish this thesis at IPP Garching and funding me through the last year of this project.

I am grateful to Vladimir Rozhansky from Peter the Great St. Petersburg Polytechnical University bringing the inspiration of the whole project and helping me throughout it till the very end. I am also grateful to the SOLPS-ITER team of the Polytechnical University - Elizaveta Kaveeva, Ilya Senichenkov, Irina Veselova, and Sergey Voskoboynikov, who always were co-authors on my papers and never refused to help me.

I am thankful to the ITER Organisation for welcoming me for a one year internship. I am especially grateful to Xavier Bonnin and Richard Pitts for teaching me a lot of important life lessons. I would also like to thank all the members of the science division, especially Steve Lisgo, Alexei Polevoi, Isabel Nunes, Aneeqa Khan, Javier Artola, Marco Andrés Miller, Daan van Vugt, Ryan Sweeney, Himank Anand, Toon Weyens, Stijn Franssen, Joseph Snipes, Peter de Vries and Alberto Loarte for their support and interesting lunch discussions. Conversations with my friend, Katerina Komissarova were also a highlight of these times for mes for me.

I am also grateful to the Katholieke Universiteit Leuven for the productive half year I spent there. I gained a lot of knowledge on the numerical methods during this time. I would especially mention Kristel Ghoos, Stefano Carli, Ján Drgoňa, Wouter Dekeyser and Martine Baelmans.

The most productive time of my Ph.D. was spent at the Max-Planck-Institut für Plasmaphysik (IPP) in Garching. I am very thankful to Anja Bauer for helping me to figure out all the complications with the documents. I am extremely thankful to the IPP team for teaching me scientific methods, introducing me to the analysis of the experimental results of the ASDEX Upgrade tokamak, deepening my knowledge of theoretical plasma physics and computational physics. I would especially mention

Matthias Bernert, Mike Dunne, Athina Kappatou, Marco Wischmeier, Bruce Scott, Matthias Hoelzl, Tobias Görler, Gergely Papp and Alex Chankin and thank them for the time they spent with me and for the knowledge they shared. I would also mention Thomas Hayward who helped me to automate my calculations and always answered my questions on the IPP computing systems. And of course I would like to thank Felix Reimold, who is now working at Max-Planck-Institut für Plasmaphysik (IPP) in Greifswald for all the support and knowledge he gave me.

I am very thankful to the Ph.D. students, who studied together with me at the IPP for our discussions, which always supported me a lot. I would like to mention here Ana Kostic, Veronika Klevarova, Egor Seliunin, Ivan Paradela Perez, Ferdinand Hitzler, Stephan Glöggler, Dieter Boeyaert, Branka Vanovac, Niels Horsten, Georg Harrer, and many others; but this list would be way too long if I were to mention all the people who supported me. If you don't find your name here, but we had a warm conversation - please, be sure, I am very thankful to you as well.

The people, who supported me the most, were my scientific advisors: David Coster from IPP Garching, Philippe Ghendrih from Aix-Marseille University and Jean-Marie Noterdaeme from Ghent University. David Coster taught me most of what I know about the Linux system and about how to work with the data, which remains one of the main working tools in my everyday life, and supported me with scientific discussions during the whole project. He also made me feel very welcome in IPP Garching from my first day there as a Ph.D student. Philippe Ghendrih and Jean-Marie Noterdaeme were my academic advisors and helped me to make progress even when I was completely ready to give up. Without them this thesis would not have been written. They both contributed a lot to the creation of the final version of this document. Here I would also like to mention Kristel Crombé who was my advisor in Ghent University for the last year and supported me a lot.

The person who also contributed to my professional development a lot is Elisabeth Wolfrum from IPP Garching. She convinced me that my scientific progress was enough to write a thesis, explained to me how to do it (by making small steps every day), and helped me to get a new project which helped me to survive the bureaucratic burden at the end of this one and showing me that doing science can still be fun. I am endlessly thankful for all that. Here I would also like to thank Bernd Kurzan from IPP Garching, who supported me on my new project, while I was still finishing this one.

Last but not least, I would like to thank my friends and family, who was always there for me. I would like to mention here my friends from many different places: Xenia Schmalz, Ondřej Kudláček, Kristel Ghoos, Anna Medvedeva, Christina Kirichenko, Oleg Krutkin, Anton Bogomolov, Egor Seliunin, Dmytro Meshcheriakov, Serhiy Mochalskyy, Dasha Ivanova, Anna Kopejkina, Alexei Lansere, Anna Lansere and Daniel Told. For the daily support I would like to thank my mom, Eva Lansere.